NATIONAL INSTITUTE FOR FUSION SCIENCE

The 7th Japan-China-Korea Joint Seminar on Atomic and Molecular Processes in Plasma (AMPP2018)

Edited by Daiji Kato, Ling Zhang, and Xiaobin Ding

(Received - Apr. 08, 2019)

NIFS-PROC-114

May 10, 2019

The 7th Japan-China-Korea Joint Seminar on Atomic and Molecular Processes in Plasma (AMPP2018)

Jul. 24 – 26, 2018, Hefei, China

Edited by Daiji Kato, Ling Zhang, and Xiaobin Ding

Abstract

The 7th Japan-China-Korea Joint Seminar on Atomic and Molecular Processes in Plasma (AMPP2018) was held on July 24 – 26, 2018 at Institute of Plasma Physics in Hefei, China, as one of the activities of Post Japan-China Core University Program, JSPS-NSFC-NRF A3 Foresight Program in the field of Plasma Physics "Study on Critical Physics Issues Specific to Steady State Sustainment of High-Performance Plasmas", and the NINS program of Promoting Research by Networking among Institutions (Grant Number 01411702).

Topics of AMPP2018 cover spectroscopic properties of impurity ions in fusion plasmas, plasma-wall interactions, diagnostics of laser induced plasmas, highly charged ion physics, atomic and molecular collision dynamics, plasma simulation and diagnostics, and application of statistical methods to atomic data evaluation. In the seminar, there were 34 oral talks (including 5 talks by phD students). The total number of registered participants was 100 (89 from China, 10 from Japan, and 1 from Korea). The present issue of the proceedings has collected 12 papers from the delegates of the seminar. The present issue includes abstracts of all presentations in the seminar, the scientific program, and the list of participants.

Keywords:
charge transfer, Auger process, recombination, three-body fragmentation, atomic structure, oscillator strength, cross section, tungsten, lanthanide, highly charged ion, X-ray scattering, EUV spectroscopy, visible forbidden lines, hydrogen recycling, LHD, EAST tokamak, statistical analysis

Preface

"*If, in some cataclysm, all of scientific knowledge were to be destroyed, and only one sentence passed on to the next generations of creatures, what statement would contain the most information in the fewest words? I believe it is the atomic hypothesis (or the atomic fact, or whatever you wish to call it) that all things are made of atoms …*" (quotes from 1. Atoms in Motion, Feynman Lecture on Physics). Many characteristics of plasmas can also be understood in terms of atomic and molecular processes taking place in the plasmas. More specifically, electronic, atomic, and photonic collision processes and radiative transitions play a decisive role for atomic and molecular abundance, photon emission and absorption properties, and energy balance of plasmas. Emission and absorption line spectra of atoms and molecules give a precise measure of temperature, densities, constituent species, etc, of fusion and astronomical plasmas. It is, therefore, obvious that constant communications of researchers of atomic and molecular processes and plasma research are important for further development in applications of atomic and molecular data to plasma researches. New knowledge in atomic physics offers novel ideas to understand plasma behaviors. Collaboration with plasma researchers creates new applications and researches of atomic and molecular processes in plasmas. The seminar series of Atomic and Molecular Processes in Plasma (AMPP) has been offering a unique interdisciplinary meeting for researchers of atomic and molecular processes and plasma research in Japan, China, and Korea to discuss about these issues.

The 7th Japan-China-Korea Joint Seminar on Atomic and Molecular Processes in Plasma (AMPP2018) was held on July 24 – 26, 2018 at Institute of Plasma Physics in Hefei, China, as one of the activities of Post Japan-China Core University Program, JSPS-NSFC-NRF A3 Foresight Program in the field of Plasma Physics "Study on Critical Physics Issues Specific to Steady State Sustainment of High-Performance Plasmas", and the NINS program of Promoting Research by Networking among Institutions (Grant Number 01411702). This seminar is the extension of the last six seminars that were held in 2004 in Lanzhou, China, in 2007 in Dunhuang, China, in 2009 in Xi'an, China, in 2012 in Lanzhou, China, in 2014 in Lanzhou, China, and in 2016 in Chengdu, China. Topics of AMPP2018 cover spectroscopic properties of impurity ions in fusion plasmas, plasma-wall interactions, diagnostics of laser induced plasmas, highly charged ion physics, atomic and molecular collision dynamics, plasma simulation and diagnostics, and application of statistical methods to atomic data evaluation. In the seminar, there were 34 oral talks (including 5 talks by phD students). A poster session was also organized. The total number of registered participants was 100 (89 from China, 10 from Japan, and 1 from

Korea). The present issue of the proceedings has collected 12 papers from the delegates of the seminar. The present issue includes abstracts of all presentations in the seminar, the scientific program, and the list of participants.

On behalf of the organizing committee, we would like to express our sincerest thanks to all the participants who made active contributions not only in the formal presentations but also in the fruitful discussions. We would like to acknowledge everybody who devoted very hard work for preparing the seminar. Finally, we would like to acknowledge the administrative as well as the financial supports from Institute of Plasma Physics, CAS and National Institute for Fusion Science.

Ling Zhang
Institute of Plasma Physics, CAS, Hefei, China
Xiaobin Ding
Northwest Normal University, Lanzhou, China
Daiji Kato
National Institute for Fusion Science, Toki, Japan

Contents

Preface

Contents

Photo of Participants

Papers

Hajime Tanuma
Soft X-ray emissions from inner-shell excited Li-like ions in charge transfer collisions of metastable He-like ions with neutral gases 1

Yulong Ma
Theoretical investigation of resonant multiple Auger processes of core-excited Ar $2p_{3/2}^{-1}4s$ 5

Daiji Kato
Statistical properties of atomic structures of r-process elements 11

Shigeru Morita
Estimation of photon emission coefficients in tungsten UTA transitions using LHD plasmas 17

Takehiko Esaka
Application of matrix decomposition technique to tungsten spectra measurement data 21

Ling Zhang
Estimation of density profiles of W^{43+}-W^{45+} in EAST H-mode plasma 27

Fumihiro Koike
A consideration on the accuracy of GRASP calculations 32

Nobuyuki Nakamura
Visible spectra of multiply charged heavy ions obtained with a compact electron beam ion trap 36

Ya-Wei Liu
Oscillator strengths and integral cross sections of the valence-shell excitations of oxygen molecule studied by fast electron and X-ray scattering 40

Shu-Xing Wang
Electron-ion recombination of Be-like Ca 46

Takuya Osugi
Statistical Analysis of Hydrogen Recycling in the Peripheral Region of LHD 50

Lei Chen
Three-body fragmentation dynamics of CF_4^{2+} induced by 1 keV electron collision 56

Seminar Program 61

Collection of Abstracts 65

Participants List 110

The 7th China-Japan-Korea Joint Seminar on Atomic and Molecular Processes in Plasma

July 24-27, 2018, Hefei, China

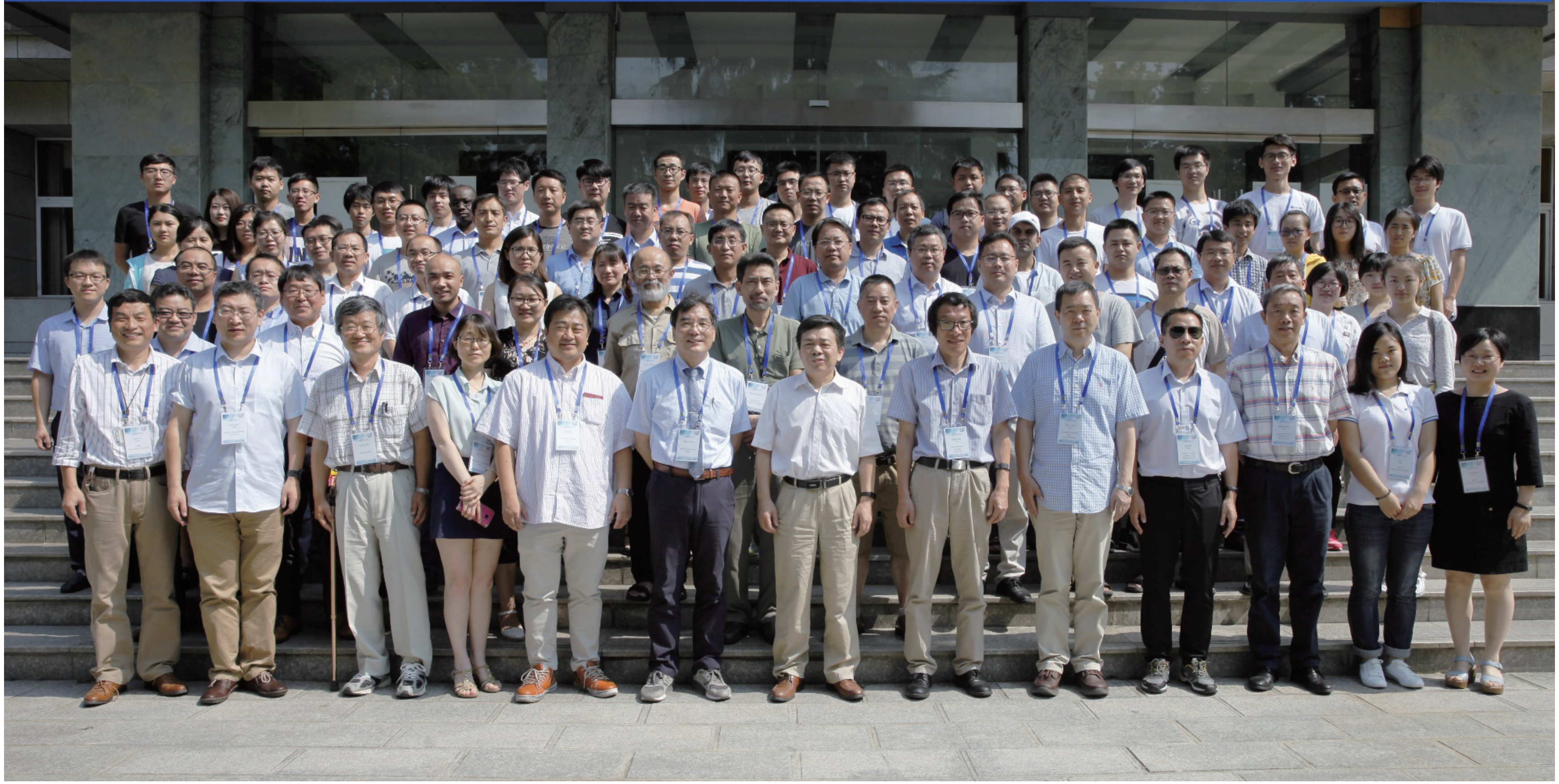

Soft X-ray emissions from inner-shell excited Li-like ions in charge transfer collisions of meta-stable He-like ions with neutral gases

Hajime Tanuma* **and Naoki Numadate**

Department of Physics, Tokyo Metropolitan University, Hachioji, Tokyo 192-0397, Japan

Abstract

We show soft X-ray emission spectra in collisions of He-like C, N, and O ions with neutral gases. Emissions are identified as transitions from doubly excited (inner-shell excited) Li-like ions produced in collisions of meta-stable He-like. Comparison with previous works and some discussion is given.

1. Introduction

In Tokyo Metropolitan University, we have performed ion-beam collision experiments using a 14.25 GHz ECR (electron cyclotron resonance) ion source which produces a plasma of temperature about 10^6 K. When we measured soft x-ray emissions in the collisions of helium-like O ions, O^{6+}, with helium gas, we observed high energy photons of 560 and 630 eV by using of a silicon drift detector (SDD) accidentally. Since the ionization potential energy of O^{5+}, which is produced in charge transfer reaction in the O^{6+} - He collisions, is 138 eV, we can say that these high energy emission is not due to singly excited O^{5+} ($1s^2nl$) ions.

Therefore, we consider that the emissions from 1s2s*nl* states produced in charge transfer collisions of helium-like ions in the meta-stable triplet states, 1s2s $^3S_1$, were observed in our experiments. As it is well-known that the helium-like ion beam produced with an ECR ion source is a mixture of the ground state and the long-lived excited state and has few percent of the meta-stable state, the formation of 1s2s*nl* states might be possible. However, the most probable decay process of the inner-shell excited state is usually Auger electron emission, and the radiative emission is not strongly expectable.

We have looked for the previous similar studies in the literature, and we found a series of experiments in Grenoble, France, using C^{4+}, N^{5+}, and O^{6+} ions [1, 2, 3]. In these experiments, the results with He and H_2 target gases were reported. Then we have performed the experiments with same three kinds of helium-like ions and various gas targets in this work.

2. Experiments

Multiply charged ions produced with this ion source were extracted with an electric potential of 15 kV and the charge-state of the ions was selected by using a double-focusing dipole magnet. The ion beam with a single charge state was introduced into a collision cell filled with a target gas, and photon emissions from the collision cell in an EUV (extreme ultra-violet) region were observed with a compact grazing-incident spectrometer equipped with a gold-plated cylindrical mirror for light condensing and a variable-line-spacing (ca. 1200~lines/mm) grating. A CCD (charge coupled device) camera with a Peltier cooling system was

---

* Corresponding author's email: tanuma-hajime@tmu.ac.jp

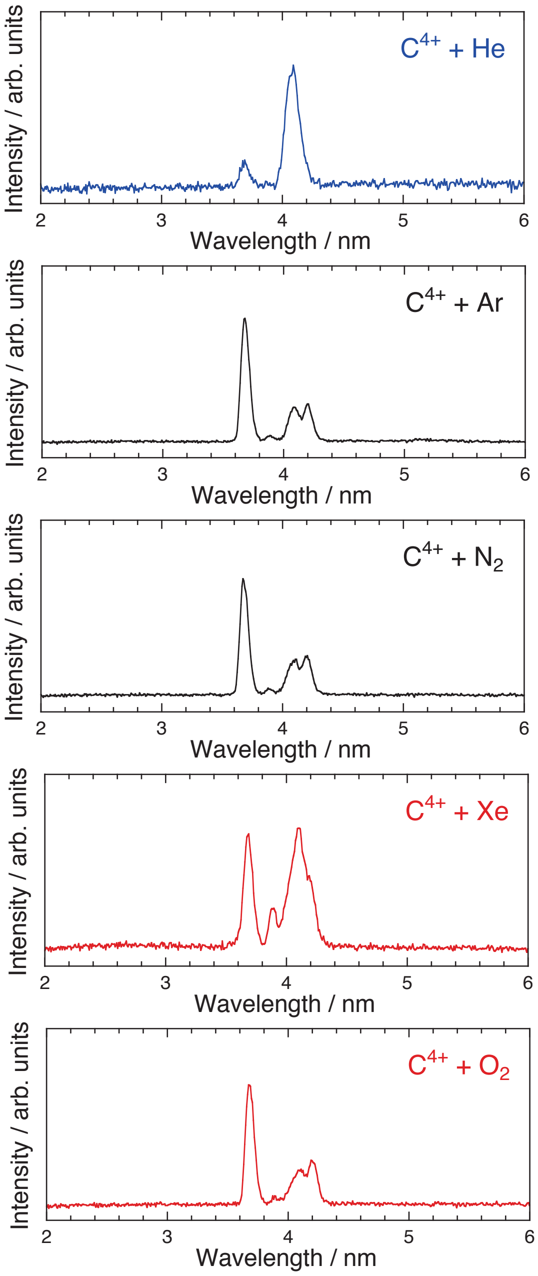

Figure 1. Soft X-ray spectra observed in collisions of C^{4+} ions with five kinds of target gases.

installed in the spectrometer. Target gas pressures in a gas cell was around 1x10^{-2} Pa, and not only single collisions but also double collisions might happen. Typical ion beam current which had been monitored at the end section of a beam line was 1 μA.

3. Results and Discussion

Figure 1 show soft X-ray emission spectra in collisions of 60 keV C^{4+} ion beam with He, Ar, N$_2$, Xe, and O$_2$ target gases. The spectrum in the C^{4+} - He system is quite similar to the previous measurement [1]. The weak peak around 3.7 nm correspond to the 1s-3p transition between 1s^{2}2s ^{2}S and 1s2s3p ^{2}P states, and the strong peak around 4.5 nm might be due to the 1s-2p transition between 1s^{2}2s ^{2}S and 1s2s2p ^{2}P states. The identification of these transition is confirmed by the comparison with the theoretical calculations [4, 5].

In the spectra of Ar and N$_2$ targets, the 1s-3p peak is prominent, and the 1s-2p peak splits to the emissions from the 1s2s3p ^{2}P and 1s2s3p ^{4}P states. Ar and N$_2$ have very similar ionization potentials of 15.76 and 15.60 eV, respectively. It is well known that the cross sections and excited state distribution after the collisions of multiply charged ions with neutral atoms/molecules depend on the ionization potential of targets. Therefore it is quite reasonable that spectra of Ar and N$_2$ targets are very similar each other.

Since Xe and O$_2$ have very similar ionization potentials of 12.13 and 12.30 eV, respectively, we expected that the spectra with both targets might be similar. However, as shown in figure 1, two spectra are significantly different. The reason of this finding is not understood yet. But, Xe is a very heavy atom and strong spin-orbit interaction might be expected. Therefor this fact might be related to the charge transfer mechanism involving spin-orbit interaction.

The soft X-ray spectra measured in the collisions of N^{5+} ions with five different target gases are shown in figure 2. In these spectra, not only the 1st diffraction by a grating but also the 2nd order diffraction which appear at the position of two-times longer wavelengths are observed at the same time. As can be seen in these spectra, the 2nd order diffraction provides us better energy resolution, and it is much useful in our measurements. In the He target case, the 1s-3p transition has about half intensity of the 1s-2p transitions. But

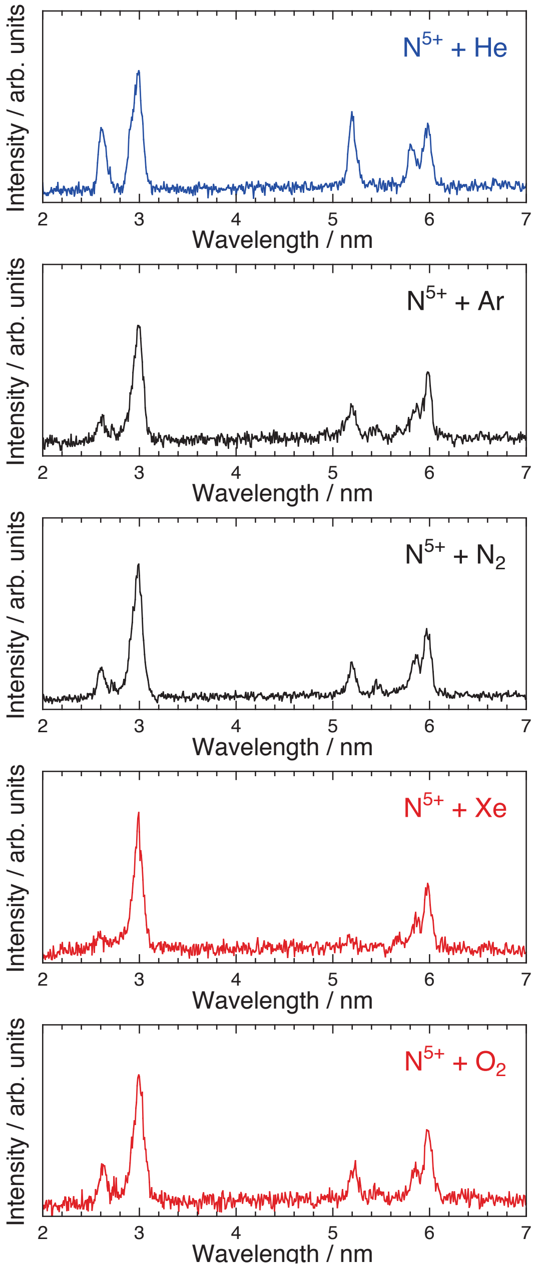

Figure 2. Soft X-ray spectra observed in collisions of N^{5+} ions with five kinds of target gases.

in other targets, the intensity of 1s-3p transitions are much smaller than the 1s-2p ones. In the 1s-2p transitions, the $1s^2 2s\ ^2S$- $1s2s3p\ ^4P$ is always stronger than the $1s^2 2s\ ^2S$- $1s2s3p\ ^2P$. Concerning to the target dependence of the emission spectra, Ar and N_2 targets show almost same spectra, and Xe and O_2 targets have significant difference in the relative intensity of 1s-3p transitions, namely a very weak 1s-3p line observed only in collisions of N^{5+} with Xe. According to the classical over the barrier model, the dominant principal quantum number of captured electron orbital must be four in the cases of Xe and O_2 targets. Therefore the missing of 1s-3p transition means the dominant state produced in the single electron capture is 4p or 4f states, and the population of 3p state created by the cascade processes might be very small. The reason why only Xe target shows different behavior might be due to the strong spin-orbit interaction in the heavy element atom.

Figure 3 shows the soft X-ray emission spectra in the collisions of O^{6+} ions with five different target gases. Here also the 2nd order diffraction has observed with the 1st order ones. The 1s-3p transition was observed only in the case of He target. And the spectra with Ar, N_2, and O_2 targets are almost same, but that with Xe show a peak corresponding to the $1s^2 2s\ ^2S$- $1s2s3p\ ^2P$ transition. This target dependence also might be related to the strong spin-orbit interaction in the heavy element atom Xe.

4. Possible Application

In the dense target gas, double and more multiple collisions of projectile ions with gas atoms/molecules will occur very frequently. Bare and hydrogen-like ions will become metastable helium-like ions and also inner-shell excited lithium-like ions. Since a few fraction of bare and hydrogen-like ions are contained in the solar wind, the soft X-ray emissions which are discussed in this work might be observed in the atmosphere of planets. Therefore the soft X-ray emissions from the inner-shell excited lithium-like ions will be a new tool for the spectroscopic analysis of the planet atmosphere by a X-ray observatory satellite.

5. Outlook

In this work, the resolution of the EUV spectrometer was about 0.1 nm. But, when we optimize the

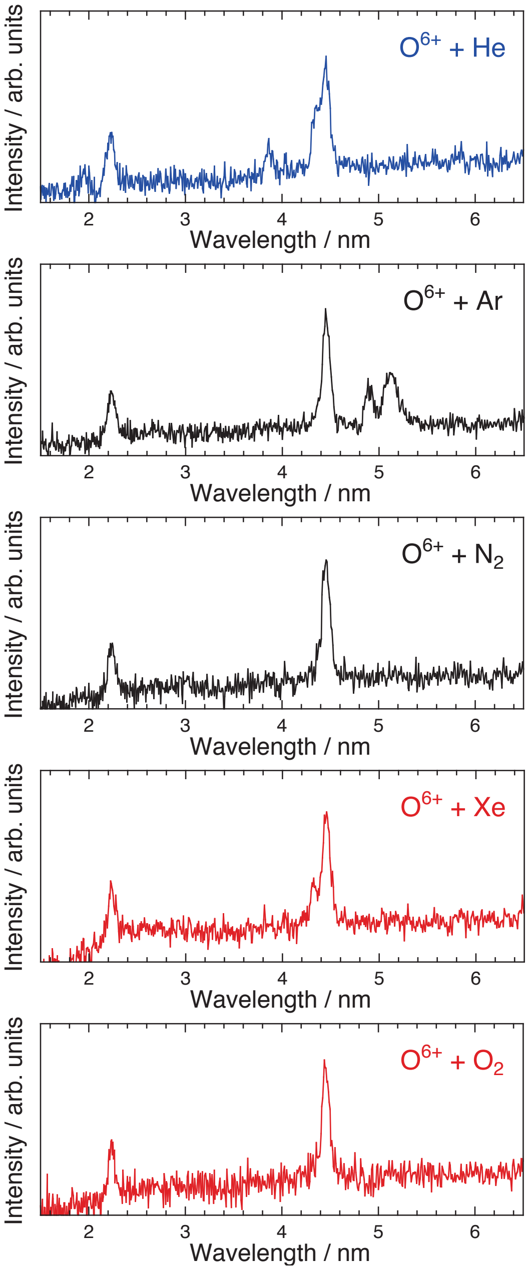

Figure 3. Soft X-ray spectra observed in collisions of O^{6+} ions with five kinds of target gases.

alignment and a slit width, the resolution of 0.02 nm might be achieved. In the preliminary high resolution measurement with long exposure time give much more narrow and weak lines. In these measurements, not only single electron capture but also transfer excitation, which produce 1s2p3*l* states, and two-electron one-photon processes, for example the transition of 1s^{2}3s ^{2}S - 1s2s(^{3}S)4p, were observed. These new results will be submitted to a journal soon [6].

Acknowledgements

We thank Kento Shimada, Yoshiyuki Uchikura, Takuto Akutsu, Yohei Yamada, and Takumi Ohna for their support of the experiments. We also thanks post Japan-China-Korea A3 Foresight Program and post Core University Program (Post CUP) for giving us the great opportunity to talk on this work and discuss in the conference.

References

[1] Suraud M G *et al* 1988 *J. Phys. B: At. Mol. Phys.* **21** 1219

[2] Guillemot L *et al* 1990 *J. Phys. B: At. Mol. Phys.* **23** 3353

[3] Bliman S *et al* 1992 *J. Phys. B: At. Mol. Phys.* **25** 2065

[4] Chen M H *et al* 1983 *Phys. Rev, A* **27** 544

[5] Goryaev F F *et al* 2017 *At. Data Nucl. Data Tables* **113** 117

[6] Numadate N *et al* 2018 *to be submitted*

Theoretical investigation of resonant multiple Auger processes of core-excited Ar $2p_{3/2}^{-1}4s$

Yulong Ma[1], Zhenqi Liu[1], Fuyang Zhou[2] and Yizhi Qu[1]*

[1]School of Optoelectronics, University of Chinese Academy of Sciences, Beijing 100049, China

[2]Data Center for High Energy Density Physics, Institute of Applied Physics and Computational Mathematics, Beijing 100088, China

Abstract

The resonant single, double, triple and quadruple Auger decays of the core-excited Ar $2p_{3/2}^{-1}4s$ are investigated using the multistep approaches, i.e., the cascade, knock-out and shake-off mechanisms within the framework of many-body perturbation theory. The calculated ion yields (in percentages) of $Ar^+ : Ar^{2+} : Ar^{3+} : Ar^{4+}$ = 65.3 : 31.0 : 3.6 : 0.09 are in agreement with the recent experimental values of 69 : 28 : 3 : 0.03 [Y. Hikosaka et al., Phys. Rev. A 89, 023410 (2014)] and 66 : 30 : 4 : 0.2 [J. A. R. Samson et al., Phys. Rev. A 54, 2099 (1996)]. Furthermore, the Auger electron spectra are obtained, which are consistent with the experimental measurements. In the direct processes, the spectator processes are essential for the populations of final states, while the participator processes become dominant as the number of emitted Auger electrons increases. Besides, the shake processes also affect significantly the final states for the direct processes.

1. Introduction

Resonant multiple Auger (RMA) decays of a core-excited state produced by exciting an inner-shell electron to a Rydberg orbital, may emit one, two and even more Auger electrons. The RMA decay is one of the important relax processes for the inner-shell excited atom upon radiationless decays, which results from the many-electron Coulomb interaction. Therefore, investigations of such processes could give important information on electron correlation effects and many-body problems in atomic processes [1,2]. As the high-order process, RMA decay is forbidden within the independent particle model and, hence, it is a good candidate for testing the theoretical models that incorporate electron correlations in such process.

In the resonant Auger decay, the Rydberg electron can: (i) remain in its orbital as a spectator, (ii) take part in the Auger process, (iii) be shaken up to a higher, or shaken down to a lower orbital, which refer to as spectator, participator and shake processes, respectively. These processes from Ar $2p_{3/2}^{-1}4s$ can be represented as follows:

$$2p_{3/2}^{-1}3s^23p^64s \rightarrow 2p^6(3s3p)^{7-q}4s + qe^- \quad \text{(spectator process)} \tag{1}$$

$$2p_{3/2}^{-1}3s^23p^64s \rightarrow 2p^6(3s3p)^{8-q} + qe^- \quad \text{(participator process)} \tag{2}$$

$$2p_{3/2}^{-1}3s^23p^64s \rightarrow 2p^6(3s3p)^{7-q}nl + qe^- \ (nl \neq 4s) \quad \text{(shake process)} \tag{3}$$

where q=1, 2,3 and 4 correspond the resonant single Auger (RSA), resonant double Auger (RDA), resonant triple Auger (RTA) and resonant quadruple Auger (RQA) decays, respectively.

---

* Corresponding author's email: yzqu@ucas.edu.cn

In this paper, we present the theoretical study of the RMA decays for the Ar atom with a $2p_{3/2}$ hole following the resonant $2p_{3/2} \rightarrow 4s$ photoexcitation. In particular, the spectator, participator and shake processes are explored for the populations of the final states. In order to obtain the Auger rates, the multistep approaches, i.e., cascade, knock-out (KO) and shake-off (SO) mechanisms [3] are employed. According to the Auger rates, we are able to present the Auger spectra and final ion yields, which are consistent with the experimental data [4].

2. Theory

The RSA rate can be expressed as [5]

$$A_{if}^{SA} = \left| \left\langle \psi_f^+, \kappa; J_T M_T \left| \sum_{p<q}^{N} \frac{1}{r_{pq}} \right| \psi_i \right\rangle \right|^2 , \tag{4}$$

where $\left|\psi_i\right\rangle$ represents the initial autoionizing state and $\left|\psi_f^+, \kappa; J_T M_T\right\rangle$ is the final ionic state $\left|\psi_f^+\right\rangle$ plus a continuum Auger electron with the relativistic angular quantum number κ. J_T and M_T are the total angular momentum and magnetic quantum number of the final state, respectively.

The direct RDA rate can be obtained by the KO and SO [3], which are expressed as

$$A_{if}^{DDA(\mathrm{KO})} = \sum_m A_{im}^{SA} \Omega_{mf}(\varepsilon_0) , \tag{5}$$

$$A_{if}^{DDA(\mathrm{SO})} = \sum_m A_{im}^{SA} \left| \left\langle \psi_f^{2+}\ \kappa; J_T M_T \middle| \psi_m^+ \right\rangle \right|^2 , \tag{6}$$

respectively. Here A_{im}^{SA} is the RSA rate for the initial state Ar $2p_{3/2}^{-1}4s$ to the intermediate Ar$^+$ states. $\Omega_{\beta\gamma}(\varepsilon_0)$ is the collision strength of the inelastic scattering by the “intermediate” Auger electron with energy ε_0 from the primary RSA process, and the matrix element $\left\langle \psi_f^{2+}\ \kappa; J_T M_T \middle| \psi_m^+ \right\rangle$ represents the overlap integral between the intermediate state Ar$^+$ and final ionic state Ar^{2+} with the second Auger electron.

In the cascade RDA decay, the initial state Ar $2p_{3/2}^{-1}4s$ can undergo a RSA decay to an intermediate autoionizing state Ar^{*+}, and then decay further to final Ar^{2+} states via the emission of another electron

$$\mathrm{Ar}\ 2p_{3/2}^{-1}4s \xrightarrow{RSA} \mathrm{Ar}^{*+} + e^- \xrightarrow{autoionization} \mathrm{Ar}^{2+} + 2e^- . \tag{7}$$

Then the cascade RDA rate can be obtained from

$$A_{if}^{CDA} = \sum_m A_{im}^{SA} A_{mf}^{SA} \Gamma_m^{-1} , \tag{8}$$

where A_{im}^{SA} and A_{mf}^{SA} are the single Auger rate for the first and second steps of the cascade RDA decay, respectively. Γ_m is the total width of the intermediate state Ar^{*+}.

We propose a multistep approach to deal with the direct RTA decay with the KO mechanism. Additional contribution of the SO mechanism is neglected as this mechanism could be rather weak for the Auger electron energies below 200 eV, which was also illustrated in our previous work for C $1s^{-1}$ [6] and Ne $1s^{-1}$ [7]. In our approach, the direct RTA decay are decomposed into a sequence of the direct RDA process and the inelastic scattering process within the KO mechanism:

$$\mathrm{Ar}\ 2p_{3/2}^{-1}4s \xrightarrow{direct\ RDA} \mathrm{Ar}^{2+} + 2e^{-} \xrightarrow{KO} \mathrm{Ar}^{3+} + 3e^{-}, \tag{9}$$

and, hence, the corresponding direct RTA rate can be obtained from the expression,

$$A_{if}^{DTA} = \sum_{m} A_{im}^{DDA} \int_{0}^{E_{im}} \rho_{im}(\varepsilon)\Omega_{mf}(\varepsilon)\,\mathrm{d}\varepsilon\,, \tag{10}$$

where A_{im}^{DDA} is the direct RDA rate from the initial state Ar $2p_{3/2}^{-1}4s$ to the intermediate state of Ar^{2+} ion, which emits simultaneously two outgoing continuum electrons sharing the continuously distributed energy of E_{im} = $\mathrm{E}_i - \mathrm{E}_m$, where E_i and E_m are the energies of the initial state Ar $2p_{3/2}^{-1}4s$ and intermediate Ar^{2+} state, respectively. $\Omega_{mf}(\varepsilon)$is the collision strength of inelastic scattering off a bound electron of the intermediate Ar^{2+} ion by two "intermediate" Auger electrons from the primary direct RDA process. We treat the "intermediate" Auger electrons as the incident electron for the inelastic scattering, which has kinetic energy range from 0 to E_{im} with symmetrical U-shape distribution [8]. In order to simulate the energy distribution $\rho_{im}(\varepsilon)$, the single energy differential cross section calculated by the binary-encounter model [9] are used.

In the cascade RTA decay, three Auger electrons are emitted in a stepwise manner through the creation and decay of intermediate autoionizing states. Based on our test calculations, the important cascade process

$$\mathrm{Ar}\ 2p_{3/2}^{-1}4s \xrightarrow{direct\ RDA} \mathrm{Ar}^{*2+} + 2e^{-} \xrightarrow{autoionization} \mathrm{Ar}^{3+} + 3e^{-} \tag{11}$$

is considered, in which the final states Ar^{3+} are attribute to a primary direct RDA decay to an intermediate autoionizing states Ar^{*2+} lying above Ar^{3+} threshold with a subsequent autoionization. Then the cascade RTA rate can be obtained with

$$A_{if}^{CTA} = \sum_{m} A_{im}^{DDA} A_{mf}^{SA} \Gamma_{m}^{-1}\,, \tag{12}$$

here A_{im}^{DDA} is the direct RDA rate of the initial state Ar $2p_{3/2}^{-1}4s$ to the intermediate autoionizing state Ar^{*2+}, and A_{mf}^{SA} represents the rate of further autoionization from the Ar^{*2+} states to the final state Ar^{3+}. Γ_m is the total width of the intermediate state Ar^{*2+}.

The direct and cascade processes are also considered for the RQA decay. Similarly to the direct RTA decay, the direct RQA decay is decomposed into a primary direct RTA decay and a subsequent KO mechanism

$$\mathrm{Ar}\ 2p_{3/2}^{-1}4s \xrightarrow{direct\ RTA} \mathrm{Ar}^{3+} + 3e^{-} \xrightarrow{KO} \mathrm{Ar}^{4+} + 4e^{-}. \tag{13}$$

Besides, the cascade process

$$\mathrm{Ar}\ 2p_{3/2}^{-1}4s \xrightarrow{direct\ RTA} \mathrm{Ar}^{*3+} + 3e^{-} \xrightarrow{autoionization} \mathrm{Ar}^{4+} + 4e^{-}, \tag{14}$$

is considered, which results from that primary three electrons are emitted simultaneously in the primary direct RTA decay populating into intermediate autoionizing states Ar^{*3+} with a further autoionization.

In this work, the rates of the RSA decay were calculated using the AUGER component of the RATIP package [10], based on the MCDF method that is implemented in the GRASP2K program [11]. The autoionizing rates and collision ionization strengths as well as the overlap integrals were obtained using the flexible atomic code (FAC) [5] with some modifications [6,7].

3. Results

The calculated ion yields of Ar^{+}, Ar^{2+}, Ar^{3+} and Ar^{4+} ions produced by the RSA, RDA, RTA and RQA decays, respectively, of the Ar $2p_{3/2}^{-1}4s$ including the cascade and direct processes are summarized in Table 1 and in agreement with the available experimental values [4,12]. Our results imply that the contributions of the direct process become dominant with the increase of the number of emitted Auger electrons, as observed in the experiment [4].

Table 1. Ion yields (in percentages) produced by the resonant single, double, triple and quadruple Auger decays represented by the RSA, RDA, RTA and RQA, respectively, of the Ar $2p_{3/2}^{-1}4s$. The calculated ion yields in the fifth column with the inclusions of the cascade and direct processes are compared with experimental data [4,12].

Ions	Decays	This work			Expt.	
		Cascade	Direct	Total	Ref. [4]	Ref. [12]
Ar^{+}	RSA	-	-	65.3	69	66
Ar^{2+}	RDA	20.4	10.6	31.0	28	30
Ar^{3+}	RTA	1.2	2.4	3.6	3	4
Ar^{4+}	RQA	0.01	0.08	0.09	0.03	0.2

The RMA spectra including the cascade and direct processes are presented in Figs. 1-4, which were obtained by convolving the Auger rates with Gaussian profile considering the energy resolving power $E/\Delta E = 60$ of the apparatus in Ref. [4]. It is found that calculated spectra agree with the experimental spectra obtained by multielectron coincidence spectroscopy [4]. The possible transitions with rates are indicated by the solid vertical lines below the plots, where the colors correspond to the configurations of the final ion that are associated with the spectator (4*s* orbital), participator (only 3*s* and 3*p* orbitals), shake-down (3*d* orbital) and shake-up (5*s* orbital) processes. In Fig. 1, the contributions of $3s^23p^44s$ are most important due to the spectator process for the RSA decay. The shake-down ($3s^23p^43d$) and shake-up ($3s^23p^45s$ and $3s3p^55s$) give rise to other peaks of the RSA spectra. For the direct RDA decay in Fig. 2(a), the spectator processes are predominant, while the contributions of the participator processes become more important for the total RDA in Fig. 2(b) with the inclusion of the cascade and direct processes. Our results reveal that the cascade process is dominant and the contribution is determined to be 66% of the total RDA decay, which is consistent with the experimental estimation of ~60% [4]. The shake processes also affect significantly the populations of final states for the RDA decay. In Fig 3(a), the participator process forming the $3s^23p^3$ states is more favored than the spectator process forming the $3s^23p^24s$ states. This indicates that the participator process becomes important for direct RTA, compared to direct RDA discussed above. For the total RTA decay in Fig. 3(b), the calculated direct RTA decay is dominant accounting for 67% of the total RTA decay, which agrees with experimental estimation of ~60% [4]. This is contrary to the total RDA decay, where the formations of the Ar^{2+} states are more favored by the cascade process than direct one. In the total RTA decay, the states belonging to the configuration $3s^23p^3$ are most populated and, hence, the participator process forming the configurations $3s^23p^3$ and $3s3p^4$ is dominant. Finally, the total RQA decay spectra are displayed in Fig. 4.

According our calculations, the contribution of the direct process is far greater than that of the cascade ones. The participator process forming the states of the configurations $3s^2 3p^2$ and $3s3p^3$ is favored, and the contributions of the spectator and shake processes are small**.**

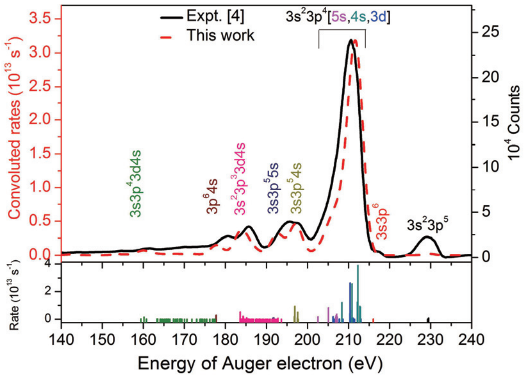

Fig. 1 Theoretical and experimental [4] resonant single Auger electron spectra of the Ar $2p_{3/2}^{-1}4s$. The vertical solid lines below the plots indicate the possible transitions, where the colors correspond to different final-state configurations that are associated with the spectator (4*s* orbital), participator (only 3*s* and 3*p* orbitals), shake-down (3*d* orbital) and shake-up (5*s* orbital) processes. The theoretical spectra was shifted 1.8 eV toward low kinetic energies.

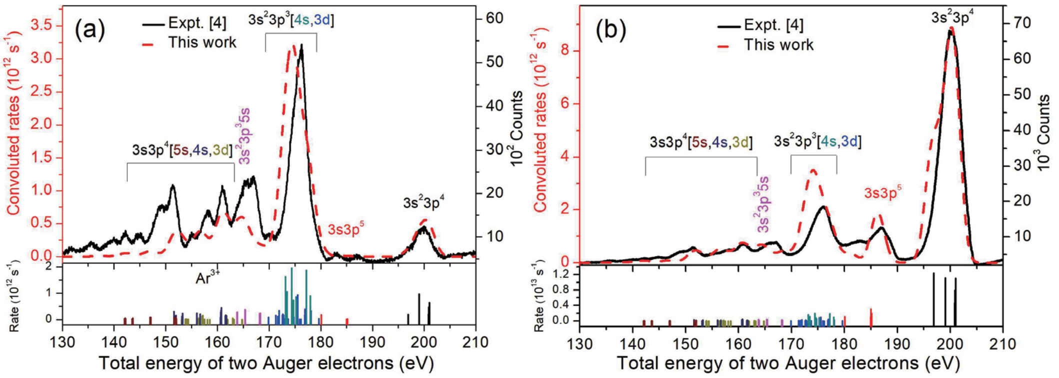

Fig. 2 Same as Fig. 1, but for (a) the direct and (b) total resonant double Auger decay including the cascade and direct processes.

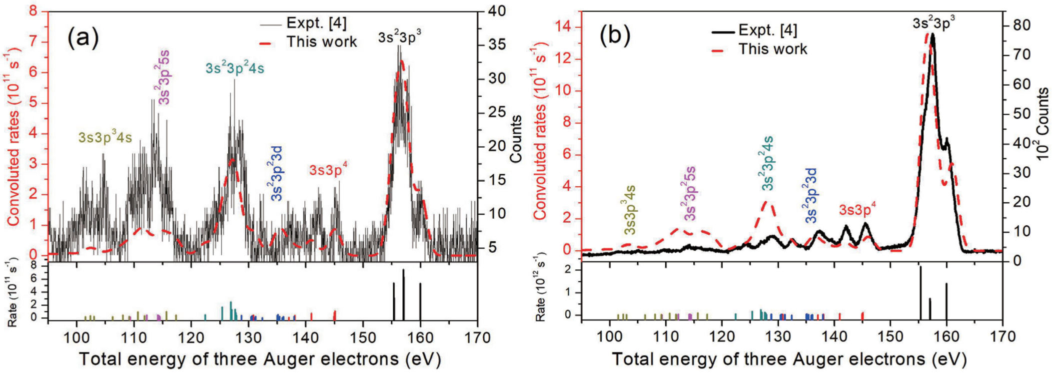

Fig. 3 Same as Fig. 1, but for (a) the direct and (b) total resonant triple Auger decay.

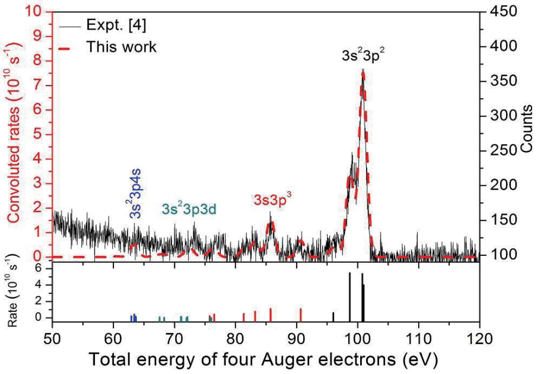

Fig. 4 Same as Fig. 1, but for total resonant quadruple Auger decay including the cascade and direct processes. The theoretical spectra was shifted 1.5 eV toward low kinetic energies.

4. Conclusion

The RSA, RDA, RTA and RQA decays following the resonant $2p_{3/2} \rightarrow 4s$ photoexcitation in neutral argon are investigated theoretically. The final ion yields and Auger electron spectra are obtained according to the Auger rates that are evaluated by using multistep approaches, namely, cascade, KO and SO mechanisms within the framework of MBPT, which are in general agreement with the experimental measurements [4]. The spectator processes are essential for the populations of final states, while the participator processes become dominant as the number of emitted Auger electrons increases for the direct processes. Besides, the shake processes also responsible for the final states during the RMA decays.

Acknowledgements

We would like to thank Y. Hikosaka for providing the experimental data from Ref. [4]. This work supported by the National Key Research and Development Program of China (Grant No. 2017YFA0402300), the National Natural Science Foundation of China (Grant Nos. 11774344 and 11474033), and the Joint Foundation of the National Natural Science Foundation and the China Academy of Engineering Physics (Grant No. U1330117).

References

[1] Pieve F D *et al* 2005 *J. Phys. B: At. Mol. Opt. Phys.* **38** 3619.

[2] Stolterfoht N *et al* 1986 *Phys. Rev. Lett.* **57** 74.

[3] Amusia M Y *et al* 1992 *Phys. Rev. A* **45** 4576.

[4] Hikosaka Y *et al* 2014 *Phys. Rev. A* **89** 023410.

[5] Gu M F 2008 *Can. J. Phys.* **86** 675.

[6] Zhou F *et al* 2016 *Phys. Rev. A* **93** 060501(R).

[7] Ma Y *et al* 2017 *Phys. Rev. A* **96** 042504.

[8] Viefhaus J *et al* 2004 *J. Electron Spectrosc. Relat. Phenom*. **141** 121.

[9] Kim Y K *et al* 1994 *Phys. Rev. A* **50** 3954.

[10] Fritzsche S 2012 *Comput. Phys. Commun*. **183** 1525.

[11] Jönsson P *et al* 2007 *Comput. Phys. Commun.* **177** 597.

[12] Samson J A R *et al* 1996 *Phys. Rev. A* **54** 2099.

Statistical properties of atomic structures of r-process elements

Daiji Kato[1,2*], **Gediminas Gaigalas**[1,3], **Masaomi Tanaka**[4,5]

[1]National Institute for Fusion Science, Toki 509-5292, Gifu, Japan
[2]Department of Advanced Energy Engineering Science, Kyushu University, Fukuoka 816-8580, Japan
[3]Institute of Theoretical Physics and Astronomy, Vilnius University, LT-10222 Vilnius, Lithuania
[4]Astronomical Institute, Tohoku University, Sendai, Miyagi 980-8578, Japan
[5]National Astronomical Observatory of Japan, Osawa, Mitaka, Tokyo 181-8588, Japan

Abstract

New calculations of atomic structures for r-process elements in ejecta of binary neutron star coalescence have been conducted using HULLAC and GRASP2K codes. The results are compared and used to evaluate impact of accuracy in the atomic calculations to opacities of electromagnetic emission from the ejecta. Universality and physical properties in complex open f-shell energy level structures of Nd II and Er II are investigated by coarse-graining methods. The energy level structures are well characterized in terms of statistics of the skewed normal distributions.

Keywords: neutron-star merger, r-process element, opacity of bound-bound transition, atomic structure calculation, coarse-graining, Kolmogorov-Smirnov test

1. Introduction

Gravitational waves by a binary neutron-star merger (NSM) have been detected on 2017 August 17 (GW170817 [1]) for the first time. Ejecta of the neutron-star merger are considered to be the cosmic origin of heavy elements created by the r-process, the rapid neutron-capture process that makes half of all elements heavier than iron. Radioactive decays of the synthesized r-process nuclei in the ejecta cause electromagnetic (EM) emission which is called as kilonova. The EM emission from the ejecta is delayed and dimmer if heavy r-process elements such as lanthanide and actinide (open f-shell) are abundant in the ejecta. Observed light curves of infra-red emission counterpart to GW170817 confirm the existence of some lanthanide contents in the ejecta [2]. However, atomic data for lanthanide are far too insufficient in available databases, *e.g.* NIST ASD [3], VALD [4] to make detail analysis of the EM emission. Thus, atomic structure calculations for the lanthanide elements are carried out by several research groups [5-9].

We present our atomic structure calculations for the r-process elements using two atomic codes, HULLAC [10] and GRASP2K [11], and opacities of bound-bound transitions with the calculated data. It is also demonstrated that potential usefulness of statistical analysis for extremely complex atomic structures of the lanthanide elements.

---

* Corresponding author's email: kato.daiji@nifs.ac.jp

2. Atomic structure calculations for opacities of bound-bound transitions

In homologous expanding gas, like points on the surface of an inflating balloon, more distant ions go away faster, i.e. velocity gradient. Because of this, line radiations from far distant ions are more red-shifted. Since the radiations are absorbed in cases that the wavelengths are red-shifted into resonance with the adjacent lines, effective opacities of bound-bound transitions in a wavelength interval becomes in proportion to densities of strong (optically thick) transitions. Lanthanide elements (open f-shell) have enormous bound-bound transitions in infra-red region giving large opacities peaking in this wavelength range. This is contrast to iron (open d-shell) which gives smaller opacities peaking in the optical range.

For the present atomic structure calculations, two different codes, HULLAC [10] and GRASP2K [11] were used. The HULLAC code, which employs a Slater-type parametric potential, is used to provide atomic data for many elements while the GRASP2K code, which enables more *ab-initio* calculations based on the multi-configuration Dirac-Hartree-Fock (MCDHF) method [12], is used to provide benchmark calculations for a few elements. In the HULLAC code calculations, the parametric potentials are optimized empirically such that the correct ground-state configuration and the lowest energies of low-lying excited-state configurations in agreement with those of NIST database are obtained. On the other hand, GRASP2K calculations are conducted by increasing the size of active space step-by-step. The GRASP2K calculation with the largest active space includes a larger number of configuration state functions than that of corresponding HULLAC calculation. Therefore, in the results of GRASP2K configuration interactions are more extensively taken into account. The Breit interaction and lowest order QED effects are included in both calculations [12].

We compared calculations using two codes and available data in NIST ASD for Nd II-III and Er II-III. Agreement between HULLAC and GRASP2K results is reasonably good. However, Er II-III energy levels of HULLAC are higher than those of GRASP2K, which may be reflecting accuracy of the GRASP2K results calculated with more extended configuration interactions. The discrepancy is most significant for excited-states of Er III. For Nd II, overall agreement of our calculations with NIST data is within 30 % which is slightly better agreement than results of Autostructure code by Kasen [2]. Both HULLAC and GRASP2K give the correct ground-state and ordering of excited-state energies, except for odd-parity states of Er II. The lowest energy of $4f^{11}6s^2$ excited-state of Er II is too high comparing with that of NIST data. It may reflect difficulty in improving electron-electron correlation effects evenly between different parity states. Further investigation is ongoing.

The opacities of Nd II-III and Er II-III calculated with transition data of HULLAC and GRASP2K codes are compared. The calculations assume the Boltzmann distribution of excited-state populations with $\rho = 1 \times 10^{13}$ g cm^{-3}, $T = 5{,}000$ K or $10{,}000$ K, and $t = 1$ day after the merger. The optical depth of rapidly expanding media is in proportion to oscillator strengths multiplied by the populations for lower levels of transitions. As expected from the good agreement in the energy levels, both results of the opacities are very similar for Nd. However, significant differences are seen in the results for Er as does in the energy levels. GRASP2K calculations give larger opacities than those of HULLAC because the populations for the lower levels of GRASP2K are larger. This discrepancy is most significant for the case of Er II and reaching to a factor of about 2 at the peak of the opacity.

3. Statistical properties of atomic structures

It is practically impossible to compare the whole open f-shell energy structures level-by-level due to uncertainty in identification of each level and quasi continuum spectra. Effective methods for evaluating such complex structures are needed for a better understanding. Coarse-graining methods are useful for understanding universal natures of complex systems and parametrization of each system. The coarse-graining methods have been applied in various fields of science including renormalization group theories [13], kinetic models of plasma turbulence [14] and molecular dynamics of complex chemical systems [15].

Figure 1 plots differential statistical-weight distributions for two excited-state configurations of Nd II binned with the finite energy interval of 0.1 eV. Results of HULLAC and GRASP2K calculations are compared with available data in NIST ASD. Although the NIST data are available only at low energies, overall profiles of the coarse-grained distributions are apparently in good agreement indicating a universal structure behind. It is noted that GRASP2K results in the figure are presented up to the ionization threshold of Nd II (10.783 eV). Based on the HULLAC results it is found that the universal structure is well depicted by the skewed normal distribution using the first three moments, i.e. mean E_{av}, variance $\sigma^2 = \langle (E - E_{\mathrm{av}})^2 \rangle$, and $\langle (E - E_{\mathrm{av}})^3 \rangle$, of the statistical-weight distribution (see Fig. 1).

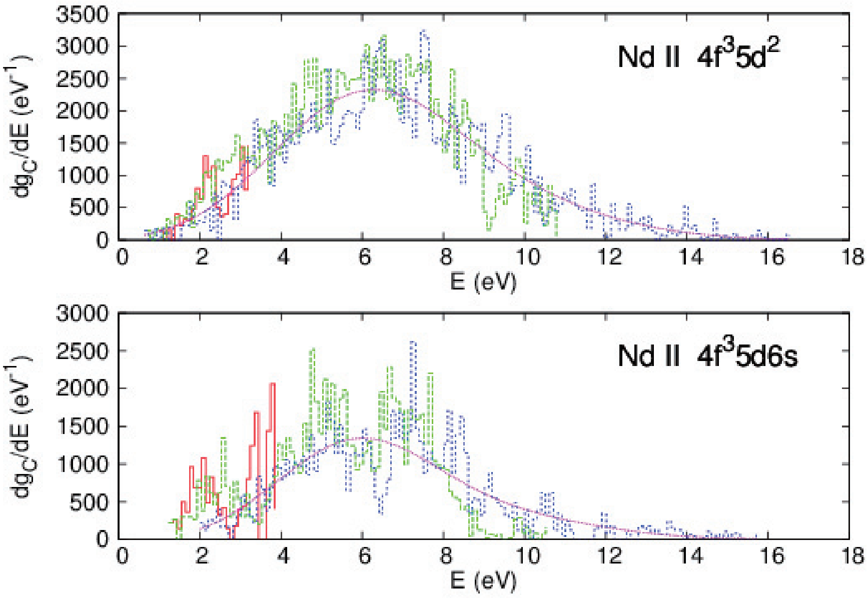

Fig. 1 Differential statistical-weight distributions of 4f^{3}5d^2 (upper) and 4f^{3}5d6s (lower) configurations. Red color stands for NIST ASD, green GRASP2K, and blue HULLAC. The results are binned with the energy interval of 0.1 eV. Corresponding skewed normal distribution functions are plotted by purple curves.

$$\frac{dg_{\mathrm{c}}}{dx}=c\left[1-\frac{1}{2}\alpha_3\left(x-\frac{x^3}{3}\right)\right]e^{-x^2/2},$$

(1)

where $x=(E-E_{av})/\sigma$ and $\alpha_3=\langle(E-E_{av})^3\rangle/\sigma^3$ (referred to as skewness). The normalization constant c is determined such that the integral of the distribution function gives the total statistical-weight of the corresponding configuration. In the earlier works [16], the skewed normal distribution has already been suggested for statistical-weight distributions of the open f-shell configurations. Signs of the skewness parameters α_3 are positive for all configurations of Nd II and Er II we have studied. This implies that large angular momentum states that possess larger statistical-weights, preferably fall into the lower energy side, which is consistent with Hund's rule as long as *LS*-coupling scheme is valid. The variances of the normal distributions for Er II are larger than those of Nd II, which should be related to that electron-electron interaction energies are larger for heavier elements due to orbital shrink in a stronger nuclear attraction force. Thus, it is encouraging to parametrize complex lanthanide atomic structures in terms of the statistics of the skewed normal distribution.

In the last part of the present work, we examine statistical properties of the energy level structures for Nd II. The coarse-graining of the energy scale is somewhat ambiguous because we can choose arbitrary energy intervals. We may ask alternatively the null hypothesis as "*Statistical distributions of energy levels obtained by stochastic sampling are the skewed normal distribution*". This is, so to speak, coarse-graining of our knowledge (information) on the energy level structures. In order to judge the null hypothesis, Kolmogorov-Smirnov (KS) test [17], which is a non-parametric statistical test without binning continuous valued samples, is applied in this study. The KS test evaluates differences between the two distributions in terms of the statistic defined as,

$$D_N\equiv\sup_E|S_N(E)-P(E)|,$$

(2)

where cumulative probability distributions $S_N(E)$ and $P(E)$ are given for our problems, respectively, as,

$$S_N(E)=\frac{1}{N}\sum_{k=1}^{N}I_{[E_{\min},E]}(E_k),$$

(3)

and

$$P(E)=\frac{1}{g_{\mathrm{c}}}\int_{E_{\min}}^{E}\frac{dg_{\mathrm{c}}}{dx}dx.$$

(4)

$I_{[E_{\min},E]}$ is the indicator function defined as,

$$I_{[E_{\min},E]}(E_k)\equiv\begin{cases}1, & E_k\in[E_{\min},E]\\ 0, & E_k\notin[E_{\min},E]\end{cases}.$$

(5)

The null hypothesis is accepted if the KS statistic D_N on average is smaller than a critical distance at a level of significance. In this study, we use the significance level of 0.05, which means that deviation of normally distributed samples over a given $P(E)$ can exceed the critical distance by chance with 5% probability. In the Fig. 2, the average values of D_N obtained by performing 1,000 tests for Nd II $4f^35d^2$ are plotted with the corresponding critical distances at the significant level of 0.05. The critical distances can be fitted by the single curve, $1.34/\sqrt{N}$. All of the averaged D_N in the figure stay below the critical distances although it is approaching to the critical distance at large N values. Thus, the null hypothesis is accepted by the present KS test for Nd II $4f^35d^2$. By increasing number of sampling N, we would acquire knowledge about more detailed energy level structures which will not completely be depicted by the skewed normal distribution resulting in the averaged D_N exceeding the critical distances.

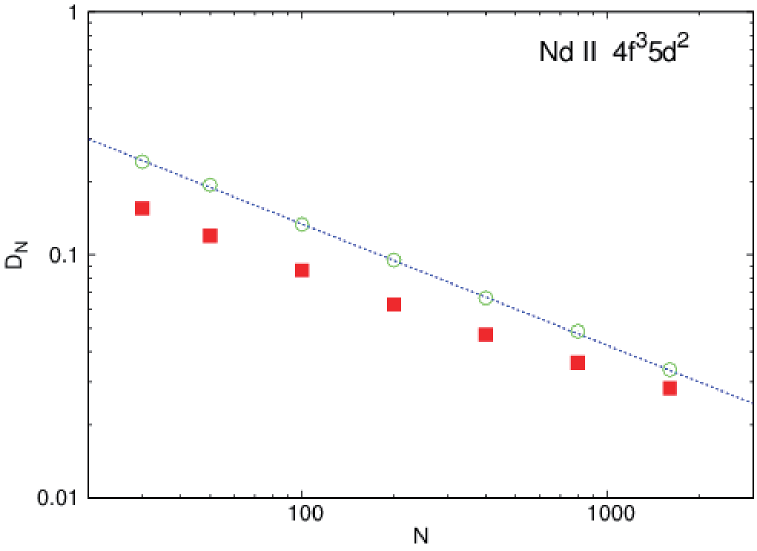

Fig. 2 KS statistic as a function of the number of sampling for $4f^35d^2$ configuration. Solid squares are D_N values averaged over 1,000 tests for each N and open circles the critical distances at the significant level of 0.05. The dotted line is the fitted critical distance curve, $1.34/\sqrt{N}$.

4. Summary and Outlook

Available atomic data (energy levels, oscillator strengths, etc) for heavy r-process elements in NSM ejecta are very limited. New calculations of the atomic data have been conducted using HULLAC and GRASP2K codes. Overall agreement in the lowest energies of configurations for Nd II-III and Er II is good. However, a significant difference remains for excited-states of Er III; GRASP2K results are in better agreement with those of NIST ASD. The lowest energy of $4f^{11}6s^2$ excited-state of Er II is too high comparing with that of NIST data. The expansion opacities of Nd II-III and Er II-III obtained with transition data calculated using HULLAC and GRASP2K are also in good agreement. The discrepancy is most significant for the case of Er II and a factor of about 2 at the peak of the opacity. Extended GRASP2K calculations, uncertainty quantification of the atomic data, and more detailed analysis on opacities obtained with the data are ongoing focusing on Nd II-IV [18].

Coarse-graining methods are applied to elucidate the universal structure in complex energy level structures of lanthanide elements. The differential statistical-weight distributions binned with a finite energy interval are well depicted by the skewed normal distribution. Physical properties in the energy level structures can be characterized in terms of the statistics. The skewness of the distributions for Nd II and Er II shows that their energy level structures are consistent with Hund's rule. Kolmogorov-Smirnov test is applied to judge whether stochastic sampling of the energy levels leads to the heuristic skewed normal distribution. This null hypothesis is accepted for Nd II $4f^3 5d^2$ at the significant level of 0.05 as long as the number of sampling is not too large.

Acknowledgements

This research was partly supported by JSPS Bilateral Joint Research Project, and the NINS program for cross-disciplinary science study. DK is grateful to the support by NINS program of Promoting Research by Networking among Institutions (Grant Number 01411702). GG is grateful to NIFS visiting professorship (7 May – 7 June, 2018).

References

[1] Abbott B P, Abbott R, Abbott T D *et al* 2017 *Phys. Rev. Lett.* **119** 161101

[2] *e.g.* Utsumi Y, Tanaka M, Tominaga N *et al* 2017 *PASJ* **69** 101

[3] Kramida A, Ralchenko Y, Reader J *et al* 2015 *NIST Atomic Spectra Database (ver. 5.3)* (Gaithersburg, MD: National Institute of Standards and Technology) http://physics.nist.gov/asd

[4] *Vienna Atomic Line Database* (Uppsala University, the Institute of Astronomy RAS in Moscow, and the University of Vienna)

[5] Kasen D, Badnell N R, and Barnes J 2013 *ApJ* **774** 25

[6] Fontes C J, Fryer C L, Hungerford A L *et al* 2017 *arXiv:1702.02990*

[7] Wollaeger R T, Korobkin O, Fontes C J *et al* 2017 *arXiv:1705.07084*

[8] Kasen D, Metzger B, Barnes J *et al* 2017 *Nature* **551** 80

[9] Tanaka M, Kato D, Gaigalas G *et al* 2018 *ApJ* **852** 109

[10] Bar-Shalom A, Klapisch M, and Oreg J 2001 *J. Quant. Spectrosc. Radiat. Trans.* **71** 169

[11] Jönsson P, Gaigalas G, Bieroń J *et al* 2013 *Comput. Phys. Commun.* **184** 2197

[12] Fischer C F, Godefroid M, Brage T *et al* 2016 *J. Phys. B: At. Mol. Opt. Phys.* **49** 182004

[13] Wilson K G and Kogut J 1974 *Phys. Reports* **12C** 75

[14] Chen Y and Parker S E 2007 *Phys. Plasmas* **14** 082301

[15] Kmiecik S, Gront D, Kolinski M *et al* 2016 *Chem. Rev.* **116** 7898

[16] Cowan R D 1981 *The Theory of Atomic Structure and Spectra* (Univ. California Press, Berkeley)

[17] Press W H, Teukolsky S A, Vetterling W T *et al* 1992 *Numerical Recipes in FORTRAN, 14. Statistical Description of Data* (Cambridge University Press 1986, 1992)

[18] Gaigalas G, Kato D, Rynkun P *et al* 2019 *ApJS* **240** 29

Estimation of photon emission coefficients in tungsten UTA transitions using LHD plasmas

S. MORITA[1,2], Y. LIU[2], I. MURAKAMI[1,2], T. OISHI[1,2], M. GOTO[1,2]

[1]National Institute for Fusion Science, Toki 509-5292, Gifu, Japan

[2]The Graduate University for Advanced Studies (SOKENDAI), Toki 509-5292, Gifu, Japan

Abstract

EUV spectra of tungsten UTA in 15-70 Å has been studied in LHD by injecting tungsten pellet. Radial profiles of the UTA line are measured with a space-resolved EUV spectrometer. Density of the W^{24+}, W^{25+} and W^{26+} ions is evaluated from the radial profile measured at specified wavelength intervals of 32.16-33.32, 30.69-31.71 and 29.47-30.47Å. In order to evaluate the ion density, a photon emission coefficient for the W^{24+}, W^{25+} and W^{26+} ions is calculated using a collisional-radiative (CR) model. The tungsten density profile of W^{24+}, W^{25+} and W^{26+} ions is obtained from the local emissivity profile and the photon emission coefficient in addition to the temperature and density profiles. A total tungsten ion density, n_W, near $\rho = 0.7$ where the W^{24+} ion locates is also estimated from the W^{24+} ion density with fractional abundance in ionization equilibrium calculated with ADAS code. The value of n_W evaluated from the present CR model seems to be large, when it is compared with n_W estimated from the number of tungsten particles injected by the pellet. Discussions are made with the n_W evaluated from the photon emission coefficient in CL version of ADAS code.

1. Introduction

Since the edge electron temperature of ITER plasmas is estimated to range in $0.2 \leq T_e \leq 4$ keV, pseudo-continuum tungsten spectra called unresolved transition array (UTA) [1] emitted at EUV wavelength ranges of 18-33 Å and 44-64 Å are very important for studying the edge tungsten behavior in ITER [2]. In LHD, the electron temperature of neutral-beam heated plasmas typically ranges in 1-4 keV and has a similar temperature range to the edge plasma of ITER. A spectral structure of the UTA has been studied by analyzing an electron temperature dependence of the UTA line intensity at each wavelength interval and measuring the peak position of radial profiles of the UTA line. As a result, it has been found that the tungsten UTA line at wavelength intervals of 32.16-33.32 Å, 30.69-31.71 Å and 29.47-30.47 Å is composed of a single ionization stage of W^{24+}, W^{25+} and W^{26+}, respectively [3].

In the present study, the tungsten ion density is evaluated as the first attempt based on the previous study on the tungsten UTA line. A vertical intensity profile of the UTA line is measured for the W^{24+}, W^{25+} and W^{26+} ions at wavelength intervals mentioned above. A photon emission coefficient (PEC) is calculated with a collisional-radiative (CR) model developed for the UTA spectrum analysis in which two effects of inner-shell excitation and configuration interaction are newly considered [4]. The tungsten ion density can be thus evaluated from the local emissivity profile and photon emission coefficient in addition to the electron temperature and density profiles measured with high accuracy. A total tungsten density can be estimated from the analyzed W^{24+} ion density profile with PEC. The total tungsten densities analyzed from CR-model and ADAS code are compared with that estimated from injected tungsten pellet size.

2. Tungsten UTA spectrum

The tungsten spectrum in the wavelength range of 18-36 Å is measured with EUV_Short spectrometer after the pellet injection, as shown in Fig. 1. The ionization stage of UTA lines in each peak group is estimated by referring the previous work from CoBIT [5] and plasma device. As shown in the figure, the tungsten UTA spectrum is composed of many ionization stages of tungsten ions, e.g. from W^{24+} to W^{33+} in the present spectrum. These UTA lines are basically formed by four transitions of 6g-4f, 5g-4f, 5f-4d and 5g-4f. In our previous work [3], the UTA line at wavelength intervals of 27.20-27.62 Å, 28.38-28.70 Å, 29.36-30.47 Å, 30.69-31.71 Å and 32.16-33.32 Å indicated with hatched regions is found to be composed of a single ionization stage of W^{28+}, W^{27+}, W^{26+}, W^{25+} and W^{24+}, respectively. In the present study, three UTA lines at 29.36-30.47 Å, 30.69-31.71 Å and 32.16-33.32 Å are used to evaluate the tungsten density profiles of W^{26+}, W^{25+} and W^{24+} ions, respectively.

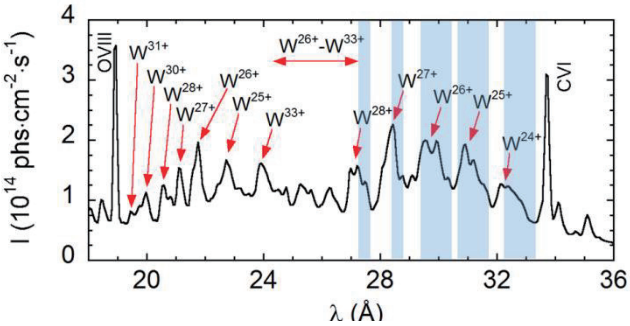

Fig. 1 Tungsten UTA spectrum at wavelength range of 18-36 Å. Shaded area indicates a wavelength interval in which UTA emission lines are composed of a single ionization stage.

3. Tungsten density profile of W^{24+} ions

Total photon emission coefficients of W^{24+}, W^{25+} and W^{26+} at wavelength intervals of 32.16-33.32, 30.69-31.71 and 29.47-30.47 Å are calculated with CR model developed for analysis of the tungsten UTA spectrum [4]. In the CR model, principal quantum number up to n = 7 and 11753, 13772 and 7515 J-resolved fine-structure levels are taken into account for W^{24+}, W^{25+} and W^{26+} ions, respectively, and 19-27 electron configurations are considered for one ion. Effects of inner-shell excitation and configuration interaction are also considered in addition to general atomic processes. The PEC at each wavelength interval then includes a lot of transitions. In practice, there are more than 100 thousands emission lines at each wavelength interval.

The result of the modeling is plotted in Fig. 2(a). The PEC is approximately constant at $T_e \geq 0.8$ keV, while it is greatly sensitive to the electron temperature at $T_e \leq 0.4$ keV. Since the tungsten ions always stay at a fixed narrow temperature window, the emission intensity is not so sensitive to the central electron temperature. In Fig. 2(b), the PEC of W^{24+}, W^{25+} and W^{26+} at 32.16-33.32, 30.69-31.71 and 29.47-30.47 Å is calculated with ADAS code [6] (CL version). In this version, 28-29 electron configurations are considered, while an energy level splitting among sublevels is not taken into consideration. The photon emission coefficient of the W^{24+} ion obtained from ADAS code is three times larger than that from the present CR model. A cascade process from higher excited levels and 5g-4f inner-shell excitations may enhance the photon emission coefficient in the ADAS code calculation.

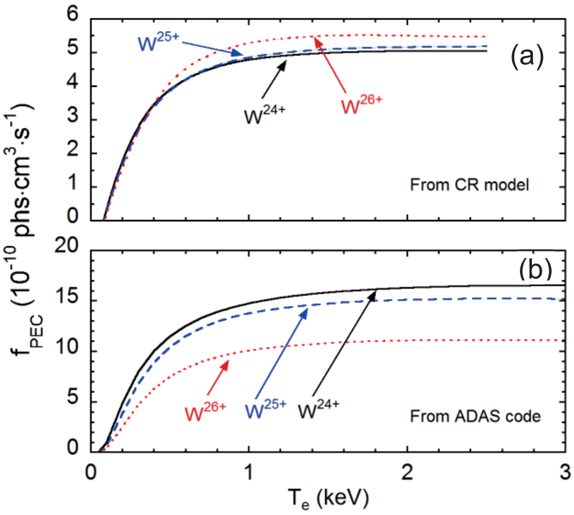

Fig. 2 Total PEC of W^{24+} (32.16-33.32 Å: solid line), W^{25+} (30.69-31.71 Å: dashed line) and W^{26+} (29.47-30.47 : dotted line) calculated with (b) the present CR model and (c) ADAS code.

4. Tungsten density profile of W^{24+} ions

The W^{24+} ion density profiles analyzed with CR-model at different temperatures are shown in Fig. 3(a). The W^{24+} ion density distributes in range of 3-5 × 10^9 cm^{-3}. The density profile of W^{24+} ions is also analyzed using PEC from ADAS code, as shown in Fig. 3(b). It is obvious that the W^{24+} ion density from CR-model is roughly three times larger than that from ADAS code, reflecting the difference in the PEC.

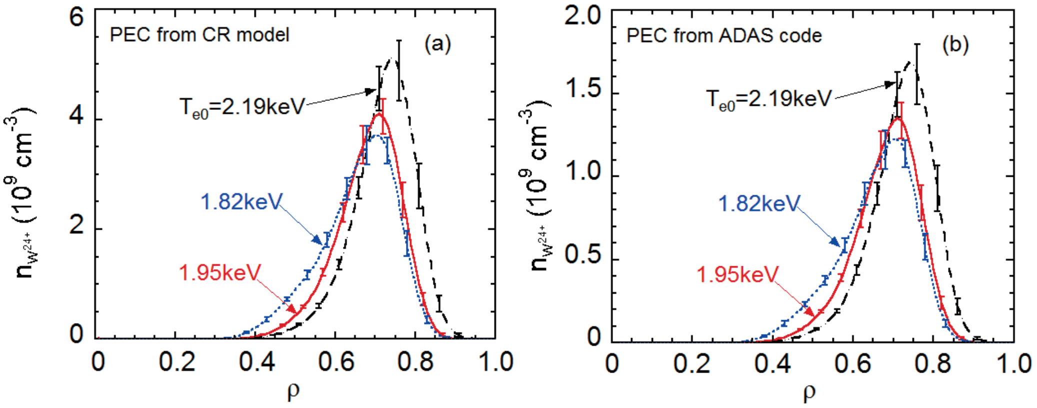

Fig. 3. Density profiles of W^{24+} ions at T_{e0} = 2.19 (dashed line), 1.95 (solid line) and 1.82 keV (dotted line) using PEC calculated with (a) the present CR model and (b) ADAS code.

Based on the analyzed W^{24+} ion density profile, the total tungsten density, $n_w(\rho)$, is estimated from an equation of the fractional abundance of W^{24+}. Here, the total tungsten density is estimated only from the peak value of W^{24+} ion profile in the vicinity of ρ = 0.7. The result is shown in Fig. 4 for the PEC from the present CR model (solid line) and ADAS code (dashed line). It is shown in the figure that the total tungsten density continuously decreases after the tungsten pellet injection at t = 4.3 s, while the reduction becomes slower as a function of time.

From the profile measurement of EUV line emissions in several tungsten ionization stages, the tungsten ion slowly expands in the radial direction toward the plasma center. The result in Fig. 4 indicates such an expansion process. In the present case the tungsten ion almost completes the expansion at Δt = 0.5 s after the pellet injection, i.e., t = 4.8 s in Fig. 4. If all the tungsten ions are uniformly distributed in the LHD plasma, we obtain $n_W = 4.1 \times 10^9$ cm^{-3} from the number of tungsten particles injected by the pellet. The n_W from PEC with the present CR model is 3.6 times larger than the n_W estimated from the pellet size. If it is compared with n_W based on PEC from ADAS code, the n_W from ADAS code is 1.2 times larger than the n_W from the pellet size. At present, however, it is difficult to discuss on the accuracy in the PEC because another model in the ADAS code has entirely different values for the PEC due to different number of electron configurations in the model. In addition, the present CR model includes possible all atomic processes and J-resolved levels, while the inner-shell excitation of 5g-4f transitions is not accurately considered and the dielectric recombination is not included. We need further efforts for quantitatively and accurately understanding the UTA line intensity.

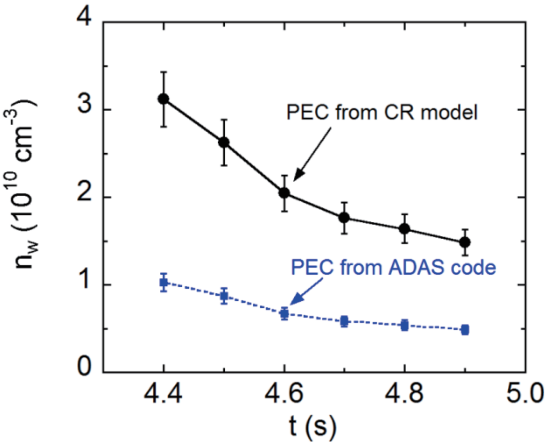

Fig. 4. Time trace of total tungsten density in the vicinity of ρ = 0.7 calculated at peak value of W^{24+} ion density profile (solid circles: the present CR model, solid squares: ADAS code).

References

[1] S. Morita, C.F. Dong, M. Goto et al., 2-13 AIP Conf. Proc. **1545,** 143.

[2] Y. Liu et al., 2018 Plasma Fusion Res. **13,** 3402020.

[3] Y. Liu, S. Morita, X.L. Huang, T. Oishi, M. Goto and H.M. Zhang, 2017 J. Appl. Phys. **122**, 233301.

[4] I. Murakami, H.A. Sakaue, C. Suzuki et al., 2015 Nucl. Fusion **55**, 093016.

[5] H.A. Sakaue, D. Kato, N. Yamamoto, N. Nakamura and I. Murakami, 2015 Phys. Rev. A **92**, 012504.

[6] H.P. Summers, 2004 The ADAS User Manual, version 2.6 http://www.adas.ac.uk.

Application of matrix decomposition technique to tungsten spectra measurement data

Takehiko Esaka[1*], Izumi Murakami[2, 3], Shigeru Morita[2, 3],
Masahiro Hasuo[1], Keisuke Fujii[1]

[1]Graduate School of Engineering Kyoto University, Kyoto Nishikyo-ku, Kyoto, 615-8246, Japan
[2]Department of Helical Plasma Research, National Institute for Fusion Science, Toki, Gifu 509-5292, Japan
[3]Department for Fusion Science, The Graduate University for Advanced Studies SOKENDAI, Toki, Gifu 509-5292, Japan

Abstract

Because of the overlap of the fractional abundance profiles of highly charged W ions, their spectra has been observed as a sum of the emission from W ions in many charge states. In this study, we applied one of matrix decomposition techniques to the W spectra observed for LHD with electron temperature of 0.5-3.0 keV. All the observed spectra were expressed with 5 spectral bases, which is much fewer than the number of charge states in plasmas expected from the theoretical fractional abundance data. From the comparison with the theoretical spectral profiles, we found that this low rank characteristics of the data is caused by the highly correlated dynamics of ions in similar charge states.

1. Introduction

Tungsten (W) was decided as the divertor material of ITER [1]. One concern of the use of W is its high radiation loss rate when W contaminates in the plasmas. Understandings of its dynamics from the divertor region to the plasma core are essential to establish efficient plasma confinement. Almost only the method to estimate the W transport is emission spectroscopy. However, because of the temperature gradient along the line of sight and the significant overlaps of the fractional abundance profiles of the W ions [2], the observed spectrum $y(\lambda_m)$ is a sum of the emission lines from W ions in many charge states,

$$y(\lambda_m) = \sum_q f_q \, \phi_q \, (\lambda_m) \qquad (1)$$

where m indicates the index of the measurement wavelength, $\phi_q(\lambda_m)$ is the spectrum from the W ion in charge state q, and f_q is its coefficient, which is the product of the emission rate and the ion density in each charge state along the line of sight. If the exact shape of $\phi_q(\lambda_m)$ is known, f_q can be determined by minimizing $\sum_m \left(y(\lambda_m) - \sum_q f_q \phi_q\,(\lambda_m)\right)^2$. However the exact shape of $\phi_q(\lambda_m)$ is not known yet and therefore a theoretical estimate $\phi_q^{\mathrm{theo}}(\lambda_m)$ has been used to fit the observed spectrum. Figure 1(a) shows $\phi_q^{\mathrm{theo}}(\lambda_m)$ for q = 25, 26 in 1.2−4.3 nm, which is calculated by a collisional-radiative (CR) model for W ions [3, 4]. Figure 1(b) shows observed W spectrum in 1.2−4.3 nm (black points) (the detail will be described

---

[*] esaka.takehiko.86a@st.kyoto-u.ac.jp

later) and the reconstruction result $\sum_q f_q\, \phi_q^{\mathrm{theo}}(\lambda_m)$ (blue curve) by using the estimated coefficients. As shown in this figure, thanks to the recent accuracy advances, $\phi_q^{\mathrm{theo}}(\lambda_m)$ reconstruct the observed spectra well in this wavelength range [3, 4, 5]. However, the observed spectra of some transitions (e.g. $4\mathrm{p}^5 4\mathrm{d}^{n+1} - 4\mathrm{p}^6 4\mathrm{d}^{n-1} 4\mathrm{f}$ transition of $\mathrm{W}^{21+} - \mathrm{W}^{35+}$ [3]) have not been represented by the theories.

On the other hand, the estimation of the coefficient f_q and the basis $\phi_q^{\mathrm{theo}}(\lambda_m)$ from a lot of data can be viewed as a matrix decomposition problem. However, the application to the emission spectrum analysis has not been reported yet. In this work, we applied one of the matrix decomposition technique to the W spectra observed in LHD for the first time.

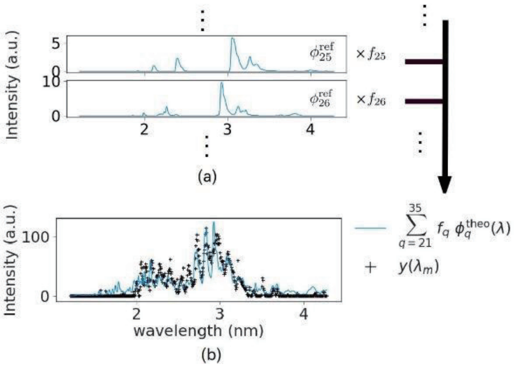

Fig. 1 (a) Theoretical calculation results of emission spectra $\phi_q^{\mathrm{theo}}(\lambda_m)$ ($q = 25, 26$). (b) The observed W spectrum (black point) and the reconstruction result by the conventional analysis (blue curve).

2. Experiments

In LHD, the emission observation of highly charged W ions has been performed with W pellet injections [6, 7]. Figure 2(a) and 2(b) show the temporal development of electron temperature (T_e) and density (n_e) at major radius R = 3.6 m (near the plasma center) measured with the Thomson scattering system [8] for a typical W pellet injection experiment. Figure 2(c) and 2(d) show the spatial distributions of T_e and n_e as a function of effective minor radius r_{eff}. After the pellet injection, T_e near the plasma center dropped from 3 keV to 0.5 keV, while n_e increased from $10^{19}\mathrm{m}^{-3}$ to $7.0 \times 10^{19}\mathrm{m}^{-3}$. These changes indicate the significant contamination of W ions in the plasma during 4.3−8.5 s.

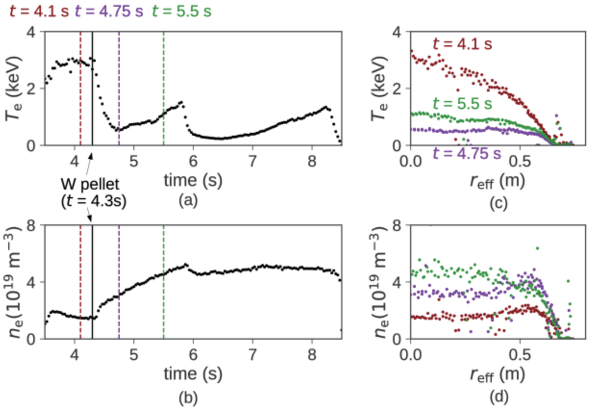

Fig. 2 (a) The temporal developments of T_e and n_e at plasma center (R = 3.6 m) for discharge #121517. (b) The spatial distribution of T_e and n_e in t = 4.0 s, t =4.75 s and t = 5.5 s for discharge #121517.

The emission was observed in 1.2–7.5 nm wavelength range with 5.0×10^{-3} nm resolution. Figure 3 shows the emission spectra observed at *t* = 4.0 s ($y^{(20)}$) (before the W pellet injection) and *t* = 4.5s ($y^{(150)}$), 5.5 s ($y^{(300)}$) (after the pellet injection), where the superscript of y indicates the index of the exposure. After the pellet injection, the quasi continuum spectra appeared. The shapes of the spectra changed depending on the measurement timings. Since the dominant charge states of W ions are considered to be $\mathrm{W}^{21+} - \mathrm{W}^{35+}$ in this temperature range based on the fractional distribution [2] (later shown in Fig. 8), the spectra are also expected from these charge state ions. We repeated the similar experiment for 5 times and the total of the observed spectra is 4580.

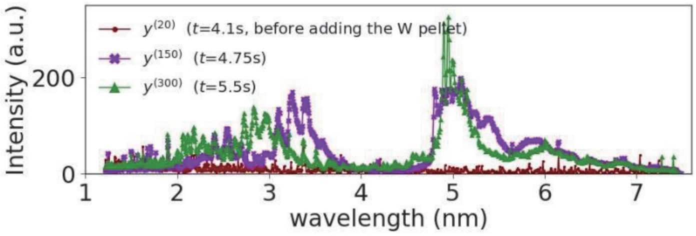

Fig. 3 Observed emission spectra $y^{(20)}$, $y^{(150)}$ and $y^{(300)}$.

3. Method

We consider multiple observed spectra, $y^{(0)}(\lambda_m)$, $y^{(1)}(\lambda_m)$, …, $y^{(n)}(\lambda_m)$, …, $y^{(4580)}(\lambda_m)$. On the assumption that the spectral shape of charge state q is common in all observed spectra (i.e., their electron temperature and density dependences are small enough), each spectrum can be rewritten as follows.

$$y^{(n)}(\lambda_m) = \sum_q f_q^n \, \phi_q(\lambda_m) \qquad (2)$$

where f_q^n depends on *n*. The spectral shape difference, which is seen in Fig. 3, indicates the variation of the coefficient values. We perform a matrix factorization to the observed spectra in order to find the coefficient and the basis matrices that most represent the observed spectral matrix. Since it is yet unclear whether the coefficients and bases estimated from the matrix decomposition exactly match f_q^n and $\phi_q(\lambda_m)$. We denote them as c_i^n and $\psi_i(\lambda_m)$, respectively, where *i* indicates the index of the basis. Figure 4 shows a schematic illustration of the matrix decomposition. We use 4580 sets of experimental data for matrix. Because c_i^n and $\psi_i(\lambda_m)$ should be non-negative, we utilize non-negative matrix factorization (NMF) [9], which constrains both two matrix to be non-negative. We estimate c_i^n and $\psi_i(\lambda_m)$ by calculating the following optimization.

$$\text{minimize} \sum_{n,m}^{4580,600} D\left(y^{(n)}(\lambda_m) \,\middle|\, \sum_i^I c_i^n \, \psi_i(\lambda_m) \right) \qquad (3)$$

where $D(a|b)$ is the distance measure between a and b, a typical example of which is the squared error $D_{\mathrm{EU}}(a|b) = (a-b)^2$. In this study, we use KL-divergence $D_{KL}(a|b) = b\log(\frac{a}{b}) - a + b$. We first set the random values to c_i^n and $\psi_i(\lambda_m)$, and repeat the iterative update scheme reported in Ref.[9] for 1500 times, which is close enough to the convergence.

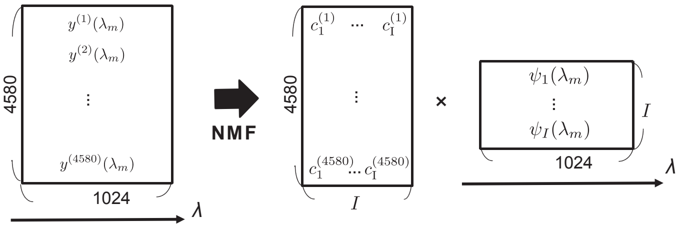

Fig. 4 The schematic image of NMF.

4. Results

We performe the NMF to the observed spectra with several matrix rank I. Figure 5 shows the relation I and the loss function defined in Eq. (3). It can be seen from this figure that the error does not greatly improve with $I \geq 5$, although at least $q = 21 - 35$ charge states are considered to exist in the plasma.

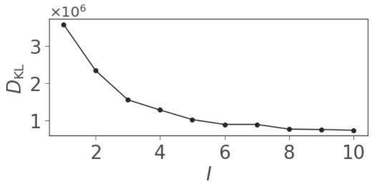

Fig. 5 The relation between I and the loss function $D_{KL}(y^{(n)}(\lambda_m)| \sum_i c_i^n \psi_i(\lambda_m))$ with the optimized c_i^n and $\psi_i(\lambda_m)$.

Figure 6(a) shows all the estimated bases with NMF (blue) with $I = 5$. Figure 6(b) show two results of the reconstruction (green, red). The values estimated coefficients for these observations are also indicated in the figure. Figure 6(c) shows an expanded view of the reconstruction by our method and the one by using theoretical calculation results $\phi_q^{\mathrm{theo}}(\lambda_m)$. The observed spectra are well fitted with $I = 5$ decomposition.

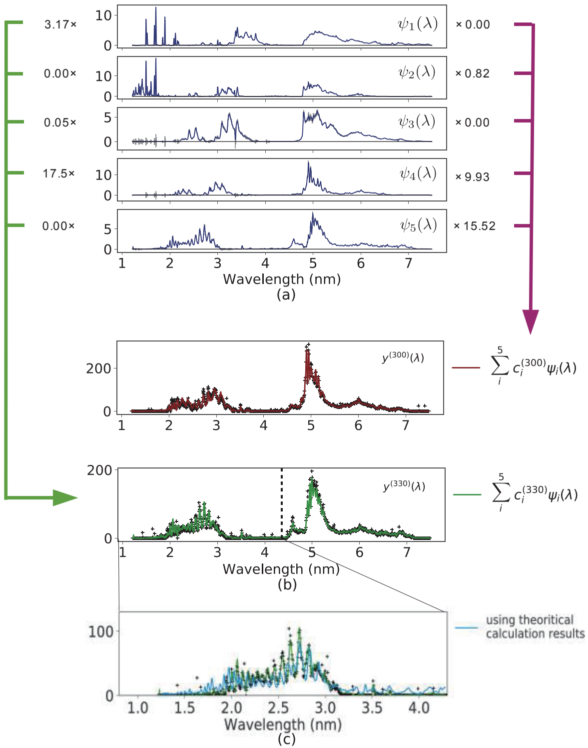

Fig. 6 (a) The bases estimated with $I = 5$. (b) The reconstruction results with the estimated bases and the coefficients. (c) Expanded view of the reconstruction by our method and the one by using the theoretical calculation results.

5. Discussion

Since the observed spectra are well represented by fewer bases than the expected total number of charge states in the plasma, the following relation is expected,

$$\sum_i c_i^n\ \psi_i(\lambda_m) = \sum_i \left\{ \sum_q f_q^n\ w_{i,q}^{-1} \sum_q w_{i,q}\, \phi_q(\lambda_m) \right\} \qquad (4)$$

where $\sum_q f_q^n\ w_{i,q}^{-1} = c_i^n$ and $\sum_q w_{i,q}\, \phi_q(\lambda_m) = \psi_i(\lambda_m)$ are satisfied, where each spectral bases is written as a weighted sum of true emission spectra from several charge states ions. Figure 7(a) shows one of the estimated basis $\psi_3(\lambda_m)$, and four theoretical emission spectra from W^{q+} for q = 23, 24, 25 and 26. While the theoretical emission spectra has one peak for one charge state in 3−4nm, the estimated basis has four peaks in this wavelength region. This is consistent to the above relation, where the estimated basis is the superposition of multiple true spectra. In order to determine the weight $w_{i,q}$ for i-th basis, we fit the superposition of the theoretical profiles to the estimated bases. We estimate $w_{i,q}$ by calculating the following.

$$\text{minimize}\left(\psi_i(\lambda_m) - \sum\nolimits_q w_{i,q}\, \phi_q^{\text{theo}}(\lambda_m) \right)^2 \qquad (5)$$

where the wavelength range of 1.2−4.3 nm is used for this fit. The results of calculated $w_{i,q}$ are shown in Fig. 7(b). The weight estimated basis has large values in similar charge states q. It indicates that the density dynamic of the similar charge state ions in plasma are highly correlated.

Figure 8(a) shows the fractional abundance for $\mathrm{W}^{21+} - \mathrm{W}^{35+}$ from [2]. As shown in Fig. 8(a), the electron temperature dependence of the fractional abundance for each charge state ion heavily overlaps each other. This overlap is consistent to the large correlation of the density dynamics of the similar charge state ions in plasmas.

We note that although the second peak can be seen in Fig. 7(b) around q =31−35 in $\psi_3(\lambda_m) - \psi_5(\lambda_m)$, they may be an artifact due to the inaccurate theoretical calculation used to estimate $w_{i,q}$.

Figure 8(b) shows the time developments of T_e and the estimated coefficients c_i^n. c_3^n takes a maximum when T_e ~ 0.5 keV, and becomes smaller as T_e becomes larger. Since $\psi_3(\lambda_m)$ mainly contains the emission from charge states $q = 22 - 27$ ions, this behavior is also consistent to the theoretical calculation of the fractional abundance, where $q = 21 - 23$ ions are dominant in this temperature region.

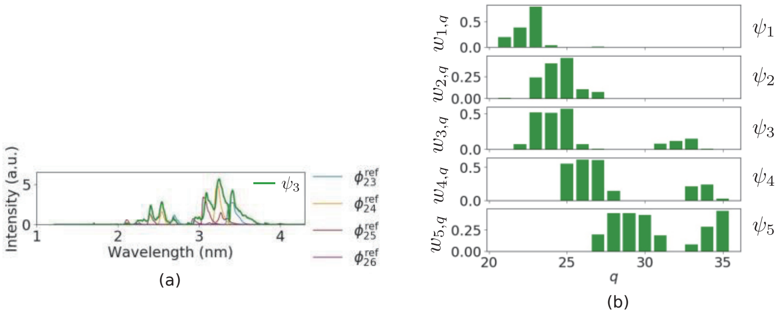

(a)

(b)

Fig. 7 (a) One of the estimated bases (green), and three examples of atomic structure calculation results (blue, yellow, red). (b) Estimated values of $w_{i,q}$ for each q.

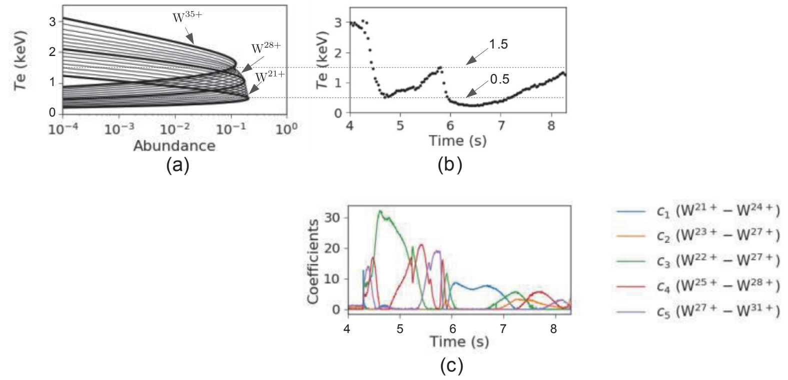

Fig. 8 (a) The fractional abundance for W^{21+}-W^{35+} [2]. (b) The time developments of T_e and the estimated coefficients c_i^n.

In summary, we applied NMF method into the W observed spectra with the various decomposition rank. From the loss function between observed spectra and the reconstruction, 5 spectral bases were enough to express the observed spectra, which was smaller than the number of charge states expected from the theoretical fractional abundance data. We assumed each estimated basis was the sum of true emission spectra from W ions in several charge states. By fitting the superposition of the theoretical W ion profiles to each estimated basis, we determined the W ions included in the basis. The basis includes W ions in similar charge states, and it suggests the correlation between the densities of W ions in similar charge states in the plasma.

Acknowledgements

One of the authors (T. E.) wishes to thanks to post Japan-China-Korea A3 Foresight Program and post Core University Program (Post CUP). We acknowledge the LHD experiment group for the LHD experiments.

References

[1] Merola M *et al 2014 Fusion Engineering and Design*, **89** pp. 890-895

[2] Asmussn K. *et al,* 1998 *Nucl. Fusion,* **38** 967

[3] Murakami I *et al*, 2015, *Nucl. Fusion*, **55** 093016

[4] Bar-Shalom A *et al,* 2001 *J. Quant. Spectrose. Radiat. Transfer*, **71** pp. 169-188

[5] Nakano T *et al* 2013*, J. Phys. B: At. Mol. Opt. Phys.*, **46** 175701

[6] Katai R. *et al* 2007*, Japan. J. Appl. Phys.* **46** 3667

[7] Sudo S. 1993, *J. Plasma Fusion Res.* **69** 1349

[8] Narihara K *et al*, 2011 *J. Nucl. Mater.*, **415** S327-33

[9] Lee D and Seung H, 2000 *Neural Information Processing Systems (NIPS)*, pp. 556-562

Estimation of density profiles of W^{43+}-W^{45+} in EAST H-mode plasma

L. Zhang[1], S. Morita[2,3], Z. W. Wu[1], Z. Xu[4,5], X. D. Yang[1,6], Q. Zang[1], H. Q. Liu[1], X. Z. Gong[1], L. Q. Hu[1]

[1]Institute of Plasma Physics Chinese Academy of Sciences, Hefei 230026, Anhui, China
[2] National Institute for Fusion Science, Toki 509-5292, Gifu, Japan
[3] Department of Fusion Science, Graduate University for Advanced Studies, Toki 509-5292, Gifu, Japan
[4] Advanced Energy Research Center, Shenzhen University, Shenzhen 518060, China
[5]Key Laboratory of Optoelectronic Devices and Systems of Ministry of Education and Guangdong Province, College of Optoelectronic Engineering, Shenzhen University, Shenzhen 518060, China
[6]Science Island Branch of Graduate School, University of Science and Technology of China, Hefei 230026, China

Abstract

In order to study the behavior and radial transport of tungsten ions in long-pulse H-mode plasmas, a space-resolved spectrometer working at 30-520Å has been newly developed to measure a radial profile of the tungsten line emission. The radial profiles of tungsten line emissions from W^{42+} – W^{45+} ions with 4p-4s and 4d-4p transitions measured at 45-70Å and 120-140Å are analyzed for the ion density evaluation based on the photon emissivity coefficient from ADAS database. The result shows that the densities of W^{43+} – W^{45+} ions range at 2-6×10^8cm^{-3} in steady H-mode discharges with $T_e(0)$=3keV and $n_e(0)=4\times10^{13}$cm^{-3}.

1. Introduction

Impurity plays an important role in sufficiently sustaining an original performance of magnetically confined fusion plasmas because of the radiation power loss and ion dilution. In particular, the radiation loss in the core plasma quickly increases with atomic number of the impurity element. In ITER, on the other hand, tungsten is used as the divertor material instead of carbon. The use of tungsten is also planned in CFETR. In order to examine effects of the tungsten divertor on tokamak discharges, several tokamak devices have installed the tungsten plasma facing component (PFC), e.g. ASDEX-U [1] and WEST [2] with full tungsten environment, JET with ITER-like wall [3]. In addition EAST tokamak has been equipped with upper tungsten divertor since 2014 to improve the heat exhaust capability and to examine the ITER-like divertor configuration [4]. To study the tungsten transport in EAST discharges, the tungsten spectra have been measured with fast-time-response EUV spectrometers working in wavelength ranges of 10-130Å (EUV_Short) and 20-500Å (EUV_Long) [5] at time resolution of 5ms. Recently, a space-resolved EUV spectrometer working in 30-520Å (EUV_Long2) has been developed to measure a radial profile of the tungsten line emission in long-pulse H-mode discharges with high heating power.

2. The space-resolved EUV spectrometer

In the space-resolved EUV spectrometer newly developed a flat-field focal plane along the wavelength dispersion direction, which enables the use of a linear detector such as CCD, is achieved by a laminar VLS concave holographic grating (Shimadzu 3-002) with an angle of incidence of 87°. A back-illuminated CCD

(Andor DO920-BN) with sensitive area of 26.6×6.6mm^2 and pixel numbers of 1024×255 (26×26μm^2/pixel) is used for recording the two-dimensional image. The long axis of CCD is set perpendicular to the horizontal wavelength dispersion for the radial profile measurement along the vertical direction, while the short axis of CCD is set along the horizontal wavelength dispersion for the spectrum measurement. A stepping motor installed on the spectrometer makes possible to move the CCD along the wavelength dispersion on the focal plane for the wavelength range selection to be measured. The vertical observation range of the space-resolved EUV spectrometer (EUV_Long2) is indicated in Figure 1. The line of sight of the fast-response EUV spectrometers (EUV_Long and EUV_Short) is also plotted in Figure 1.

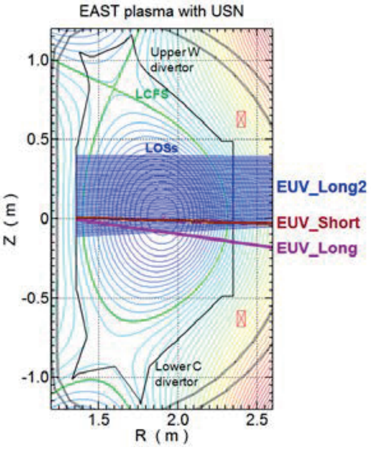

FIGURE 1. Lines of sight (LOSs) of EUV_Long2 (blue thin lines) and LOS of EUV_Long (purple thick line) and EUV_Short (brown thick line).

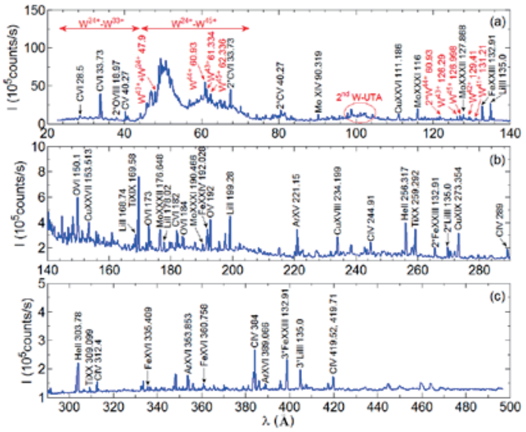

FIGURE 2. Typical EUV spectra observed with EUV_Long from EAST H-mode discharges in wavelength ranges of (a) 20-140Å, (b) 140-290Å and (c) 290-500Å.

3. Radial profiles of tungsten spectra in H-mode discharges

Figure 2 illustrates typical EUV spectra from EUV_Long observed in RF heated H-mode discharges of EAST with heating power of P_{LHW}=2.0-2.5, P_{ICRH}=1.2-1.8 and P_{ECRH}=0.3MW. The discharges are carried out at line-averaged electron density of n_e=3.5×10^{13}cm^{-3}, and T_{e0}=3.0-3.5keV. In the spectra the pseudo-continuum called unresolved transition array (UTA) is clearly appeared at 40-75 Å as a typical indication of the tungsten spectrum. Line emissions from highly ionized ions in high-Z impurities are also observed in the spectra, e.g., Ti^{18+}-Ti^{19+}, Cu^{25+}-Cu^{26+}, Mo^{30+}-Mo^{31+} and W^{41+}-W^{45+}. The W-UTA (5f-4d, 5p-4d, 6g-4f and 5g-4f transitions) composed of W^{24+}-W^{33+} ions appeared in the wavelength range of 20-40 Å is very weak, while the W-UTA (4f-4d, 4d-4p and 5d-4f transitions) composed of W^{24+}-W^{45+} appeared in the wavelength range of 45-70 Å is strong. The second order of W-UTA near 50Å is also observed near 100Å. Although isolated line emissions from highly ionized tungsten ions, e.g., W^{41+}-W^{45+}, can be identified at 120-140Å, the intensity is very weak. Then, the tungsten spectrum extended at 45-135 Å is plotted in Figures 3(a)-(c). As seen in Figure 3, there exist many tungsten line emissions in the wavelength range. Detailed identifications are made for all the tungsten line emissions. In order to make the accurate identification of tungsten line emissions, radial profiles of the tungsten line are extremely important as described in a previous report [6].

Tow-dimensional images of tungsten line emissions are observed in H-mode discharges as shown in Figure 4. Identified line emissions are denoted in right hand of the CCD image. Vertical profiles of tungsten line emissions are obtained from the CCD image, as plotted in Figures 5 (a)-(c). Figure 5 (a) shows the vertical profile of tungsten lines from highly ionized tungsten ions existing in the W-UTA, W^{43+} ($4s^24p\ ^2P_{2/1}$ –

4s4p^2 $^2D_{3/2}$) at 61.334Å, W^{44+} (4s^2 $^1S_0$ – 4s4p (1/2,3/2)$_1$) at 60.93Å and W^{45+} (4s $^2S_{1/2}$ – 4p $^2P_{3/2}$) at 62.336 Å. Based on the vertical profile of line emissions from W^{43+}-W^{45+} ions, the ionization stage of other tungsten lines can be easily estimated. Vertical profiles at the wavelength intervals indicated by shaded areas in Figure 3 (a) are plotted in Figure 5 (b). When we compare the peak position among three radial profiles, each peak locates in different radial positions. Then, we can easily identify that three wavelength intervals of 48.81-49.02 Å, 49.24-49.57 Å and 49.79-50.01 Å arise from W^{26+}, W^{27+} and W^{29+}, respectively [6]. The ionization stage of other tungsten line emissions at the W-UTA in Figure 3 (a) is also determined through the analysis of vertical profiles observed from EUV_Long2.

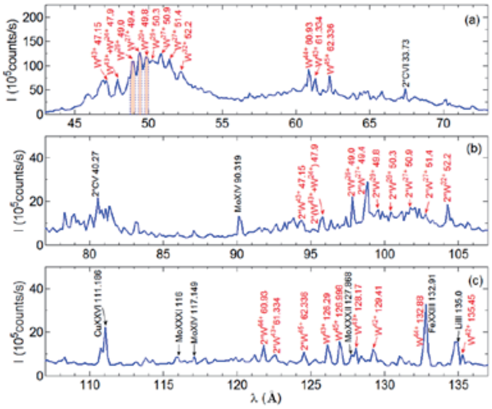

FIGURE 3. Tungsten spectra in different wavelength ranges of (a) 43-73 Å, (b) 77-107 Å and (c) 107-137 Å in RF heated H-mode discharges (T_{e0}=3.3keV).

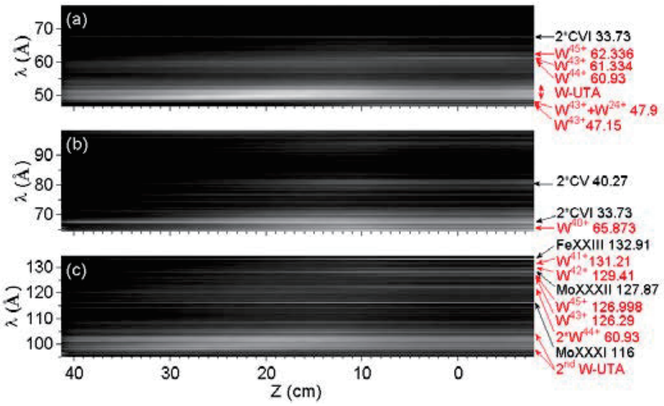

FIGURE 4. Typical two-dimensional CCD images observed from H-mode discharges (T_{e0}=2.9-4.0keV and n_e~3.5×10^{19}m^{-3}); (a) 46.6-76.9 Å, (b) 64.4-98.3 Å, (c) 95.1-134.4 Å

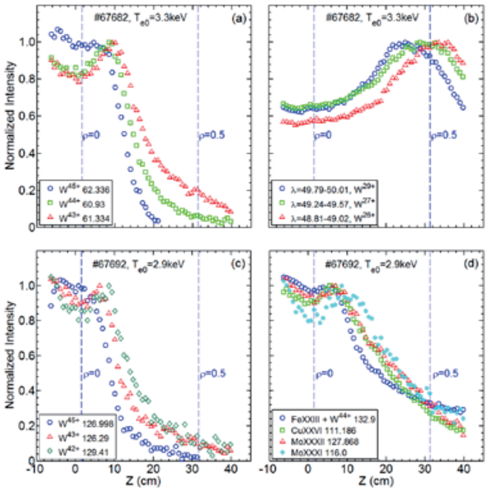

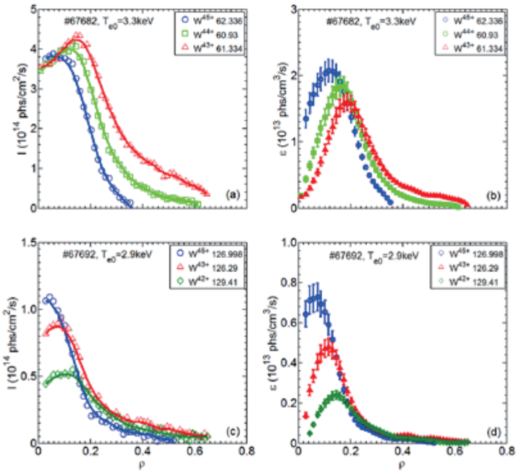

FIGURE 5. Radial profiles of (a) chord-integrated line intensity and (b) local emissivity of W^{45+} (62.336Å), W^{44+} (60.93Å) and W^{43+} (61.334Å) and (c) chord-integrated line intensity and (d) local emissivity of W^{45+} (126.998 Å), W^{43+} (126.29 Å) and W^{42+} (129.41 Å). Data are taken from H-mode discharges with T_{e0}=3.3keV ((a) and (b)) and 2.9keV ((c) and (d)).

FIGURE 6. Vertical intensity profile of (a) W^{45+} (62.336Å), W^{44+} (60.93Å) and W^{43+} (61.334 Å) in W-UTA, (b) W^{26+}-W^{29+}, (c) W^{45+} (126.998 Å), W^{43+} (126.29 Å) and W^{42+} (129.41 Å) and (d) Fe XXIII blended with W^{44+} (132.9 Å), Cu XXVI (111.186 Å), Mo XXXII (127.868 Å) and Mo XXXI (116.0 Å) . Data are taken from H-mode discharges with T_{e0}=3.3keV ((a) and (b)) and 2.9keV ((c) and (d)).

Vertical profiles of isolated line emissions are plotted in Figures 5 (c) and (d). Figure 5 (c) shows vertical profiles of W^{42+} ($4s^24p^2\ {}^3P_0 – 4s^24p^2\ {}^1D_2$) at 129.41Å, W^{43+} ($4s^24p\ {}^2P_{1/2} – 4s^24p\ {}^2P_{3/2}$) at 126.29 Å and W^{45+} ($4s\ {}^2S_{1/2} – 4p\ {}^2P_{1/2}$) at 126.998Å. We notice that the radial profiles are more peaked compared to those in Figure 5 (a) due to the relatively low electron temperature of T_{e0}=2.9keV. Figure 5 (d) shows vertical profiles of other heavy impurities, i.e. Cu XXVI ($2s^2\ {}^1S_0$ - $2s2p\ {}^1P_1$, E_i=2479eV) at 111.186 Å, Mo XXXI ($3s^2\ {}^1S_0$ - $3s3p\ {}^1P_1$, E_i=1730eV) at 116.0 Å and Mo XXXII ($3s\ {}^2S_{1/2}$ - $3p\ {}^2P_{3/2}$, E_i=1791eV) at 127.868 Å and Fe XXIII ($2s^2\ {}^1S_0$ - $2s2p\ {}^1P_1$, E_i=1950eV) at 132.9 Å. The line emission from Fe XXIII at 132.91 Å is totally overlapped with W^{44+} ($4s^2\ {}^1S_0 – 4s4p\ P_{1/2}$, E_i=2355eV) at 132.88Å. When we compare the radial profile between inner and outer regions near the plasma center, i.e. $-10 \leq Z \leq 0$cm and $0 \leq Z \leq 10$cm, it may suggest an asymmetric profile. Further experiments are necessary to confirm the truth by changing the vertical observation range.

4. Preliminary analysis of tungsten ion density profile

The chord-integrated intensity of tungsten line at vertical position of Z is calculated by integrating the local emissivity along the line of sight of EUV_Long2, l, in the equation of

$$I^{W^{q+}}(Z) = \int \varepsilon^{W^{q+}}(Z,l)dl = \int n^{W^{q+}}(Z,l)PEC^{W^{q+}}(Z,l)n_e(Z,l)dl\ , \qquad (1)$$

where $I^{W^{q+}}$ and $\varepsilon^{W^{q+}}$ mean the intensity and local emissivity of line emission from tungsten ions with ionization stage of q, and $n^{W^{q+}}$ and $PEC^{W^{q+}}$ mean the density of W^{q+} ions and photon emissivity coefficient of the line emission. Tungsten ion density profile is then analyzed from the vertical profile of tungsten spectral intensity. Firstly, the spectral intensity measured with spectrometer has to be absolutely calibrated, and then the emissivity profile of tungsten line can be calculated from the vertical intensity profile based on Abel inversion technique. Finally, the density profile of tungsten ions is obtained with measured T_e and n_e profiles and the PEC data.

The absolute calibration for the space-resolved EUV spectrometer has been excellently carried out at high density discharges with $n_{e0}=2.2\times10^{14}cm^{-3}$ in LHD [7, 8]. The EUV bremsstrahlung continuum intensity is accurately calculated from measured visible bremsstrahlung intensity profile with considering T_e profile. The calibration factor can be then obtained by comparing the EUV bremsstrahlung intensity profile between measurement and calculation. Since the operational density range of EAST is relatively low, e.g. $n_{e0}=5.5\times10^{13}cm^{-3}$, the EUV bremsstrahlung intensity from EUV_Long2 is weak due to the relatively low throughput compared to EUV_Long. In addition, the visible bremsstrahlung measurement diagnostic in EAST has no sufficient profile data. Then, the calibration of EUV_Long2 is only carried out at short wavelength range where the EUV bremsstrahlung emission is strong referring the data from EUV_Long from which the spectral intensity has been already calibrated [5], e.g. $4\times10^9 phs\cdot cm^{-2}\cdot s^{-1}/(counts\cdot s^{-1})$ at 62 Å, and $8.5\times10^9 phs\cdot cm^{-2}\cdot s^{-1}/(counts\cdot s^{-1})$ at 130Å. Since the same grating and CCD as LHD are being used in EAST, we assume the wavelength dependence of the calibration factor is identical between EAST and LHD. Thus, the vertical intensity profiles are obtained for tungsten line emissions as shown in Figures 6 (a) and (c). Figure 6 (a) shows the intensity profiles of W^{45+} at 62.336Å, W^{44+} at 60.93Å and W^{43+} at 61.334 Å from H-mode plasmas with T_{e0}=3.3keV and Figure 6 (c) shows W^{45+} at 126.998 Å, W^{43+} at 126.29 Å and W^{42+} at 129.41 Å from H-mode plasmas with T_{e0}=2.9keV.

The local emissivity profiles of tungsten line emissions reconstructed from Figures 6 (a) and (c) are plotted in Figures 6(b) and (d), respectively. The local emissivity of tungsten line emissions at the peak position increases with the ionization stage, in particular, in the low-temperature discharge in Figure 6(d). It is not clear at the moment whether the increase indicates the tungsten accumulation in the H-mode discharge. Impurity transport simulation is necessary for further study.

In order to evaluate the tungsten ion density, PEC data from open-ADAS (arf40_ic series) is used in the present study. Based on T_e and n_e profiles measured during the H-mode phase shown in Figures 7 (a) and (b), the density profiles of W^{43+} and W^{45+} are obtained. The result is plotted in Figure 8. As a result it is found that the density of W^{43+}-W^{45+} ions distributes in range of 2-6 $\times 10^8 cm^{-3}$ in H-mode discharges of EAST which we have analyzed in the present study.

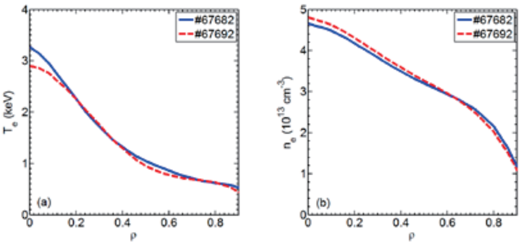

FIGURE 7. Radial profiles of (a) electron temperature and (b) electron density.

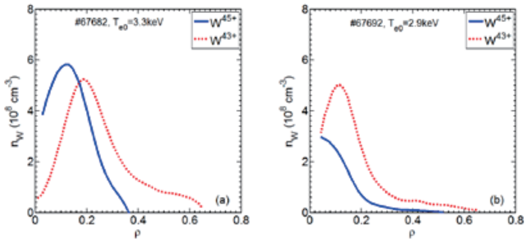

FIGURE 8. Calculated radial profiles of W^{45+} and W^{43+} ion density in steady-state H-mode phase in (a) T_{e0}=3.3keV and (b) T_{e0}=2.9keV.

5. Summary

A space-resolved spectrometer working at 30-520Å is newly developed to measure the tungsten emission profiles. As a result, vertical profiles from several impurities are successfully observed from H-mode plasmas in EAST tokamak. Vertical profiles of tungsten emissions from W^{42+} - W^{45+} ions are also measured at 45-70 Å and 120-140 Å in high-temperature discharges at $T_e \geq 2.5$keV. The density profile of such highly ionized tungsten ions is evaluated from the vertical profile. The preliminary analysis shows that the densities of W^{43+}-W^{45+} ions range in 2-6$\times 10^8 cm^{-3}$ in H-mode plasmas. The emission profile measurement by the space-resolve spectrometer enables impurity transport study in H-mode discharges of EAST. In particular, the tungsten transport study is crucially important in long pulse H-mode operations of EAST with tungsten divertor.

Acknowledgements

This work was supported by the National Natural Science Foundation of China (Grant Nos. 11575244, 11775269) and the National Magnetic Confinement Fusion Science Program of China (Grant Nos.2014GB124006, 2015GB101000)

References

[1] Neu R et al 2007 Plasma Phys. Control. Fusion 49 B59
[2] Bucalossi J et al 2014 Fusion Eng. Des. 89 907-912
[3] Matthews G F et al 2011 Phys. Scr. T145 014001
[4] Yao D et al 2015 Fusion Eng. Des. 98-99 1692
[5] Zhang L et al 2015 Rev. Sci. Instrum. 86 123509
[6] Liu Y et al 2017 J. Appl. Phys. 122 233301
[7] Dong C F et al 2011 Rev. Sci. Instrum. 82 113102
[8] Dong C F et al 2012 Plasma Fusion Res. 7 2402139

A consideration on the accuracy of GRASP calculations

Fumihiro Koike[*]

Faculty of Science and Technology, Sophia University, 7-1 Kioi-cho, Chiyoda-ku, Tokyo 102-8554, Japan

Abstract

We discuss the use of Multi-Configuration (numerical) Dirac-Fock (MCDF) method that is employed in General purpose Relativistic Atomic Structure Program (GRASP) family of codes in relation to the tactics of obtaining accurate and reliable results. The proper use of spectroscopic and correlation orbitals in the calculation is quite important. The proper choice of target states for simultaneous optimization in the calculation is also quite important. Several examples have been illustrated for precision calculations of the atomic and ionic systems. .

1. Introduction

Accurate and reliable calculations of atomic electronic states and their transition properties are indispensable for proper understandings of fusion and other plasmas. Accurate atomic data may enable us to perform precision plasma modeling calculations and help us with precision plasma spectroscopy measurements. Quite a deal of efforts has been made for this subject. For a theoretical method based on a variational principle, atomic codes such as FAC, HULLAC, Cowan’s code, GRASP family of codes[1], and others, have been developed and they are now available. Among them, the GRASP (General purpose Relativistic Atomic Structure Program) family of codes[1] provides us with a non-empirical relativistic method and is believed that the code gives most reliable result if treated properly. In recent years, an elaborate large scale calculation has become feasible using a parallel processing technology to produce a large amount of numerical values that are usable for plasma analysis.

However, we must be aware that the GRASP family of codes has its own characteristics to be treated carefully. The method is based on a variational principle with a positive indefinite Hamiltonian; we cannot avoid the possibility of variational collapse in the procedure of self-consistent iteration. And, furthermore, in cases of excited state calculations, similar collapse may occur due to the possible inaccuracies of numerical procedure. The atomic orbitals are restricted to the L_2 normalizable functions, which causes the introduction of correlation functions in the MCDF procedure. They are sometimes quite unphysical. We must take care of those functions carefully as to behave properly if we want to calculate the excited states.

In this report, we discuss possible tactics to minimize the errors in GRASP calculations showing several examples that may give undesired results.

2. Characteristics of MCDF method

Based on the independent particle model, we introduce a CSF (Configuration State Function) Φ for the

---

[*] Corresponding author’s email: koikef@sophia.ac.jp

N-electron system in terms of the product of single electron atomic orbitals. That is

$$\Phi = \prod_{i=1}^{N} \phi_{k_i}(r_i) \ , \tag{1}$$

where, ϕ_{k_i} is a single electron atomic orbital with quantum number k_i and r_i is the position of the i'th electron. The CSF Φ may be adjusted as to satisfy the constraint such as parity or Pauli's principle. The MCDF method requires the introduction of an ASF (Atomic State Function) Ψ. That is

$$\Psi = \sum_{j=1}^{j_{max}} \Phi_j \, c_j, \tag{2}$$

where, c_j are the expansion coefficients, j_{max} is the number of CSF's in the ASF. The set of atomic orbitals $\{\phi_{k_i}\}$ and the state vector $\{c_j\}$ are the target of optimization under the following variational condition.

$$\delta\langle\Psi|H_{DC}|\Psi\rangle = 0, \tag{3}$$

where, H_{DC} is the Dirac-Coulomb Hamiltonian of the atomic system. The GRASP family of codes treats also Breit interaction and a part of QED corrections to produce better results by means of perturbation.

The MCDF method is based on a variational principle. If the problem is solved properly, an excited state atomic state function does not contain any lower lying configuration state functions, in other words, the excited state can be expanded in terms of only the configurations that are lying energetically higher than the target state. However, some care must be taken into account for configurations that contain atomic orbitals with different parities. The parity constraint applies only for the total atomic state.

$$P\Psi = \pm 1\Psi. \tag{4}$$

Individual single electron atomic orbitals are not necessarily being required to have a fixed parity. Both configurations $\phi^{\text{even}}(r_i) \otimes \phi^{\text{even}}(r_j)$ and $\phi^{\text{odd}}(r_i) \otimes \phi^{\text{odd}}(r_j)$ can contribute in the same atomic state functions. For example, $2s2p3s = 2p(2s3s)$ and $2p^2 3p = 2p(2p3p)$ configurations strongly mix in the lithium hollow atomic states [2]. This feature sometimes prevents us from assigning the atomic states in terms of the occupation numbers for electrons in atomic orbitals.

Generally speaking, the effect of electron correlations is the strongest near the nucleus, where the electrons have larger chance to be close each other. The correlation orbitals which are introduced in MCDF calculations have a maximum near to the nucleus. By taking those functional shapes, we can expect that the set of orbital functions spans a complete bases space under the restriction of L_2 normalizable basis.

In the followings, we illustrate two numerical examples.

3. The sub-valence inner-shell hole states of rare gas ions

Sub-valence inner-shell vacancy states of rare gas atomic ions with $nsnp^6$ configuration decay into the ground states with ns^2np^5 configuration exclusively through the optical-dipole transitions. It is worthy to investigate the role of electron correlations in atomic ions under such simple circumstances. In most of the atoms with moderate atomic number, there are energy differences between sub-shell atomic orbitals due to the deviation of the effective potentials from Coulombic nature. In the case of Ar^+ ions, for example, the energy difference between $3s$-orbital and 3p-orbital is not very different from the energy difference between $3p$-orbital and $3d$-orbital. Thus the $3s$ sub-shell single-hole configuration $3s3p^6$ may have strong interaction with the $3p$ sub-shell single-electron excited configuration $3s^2 3p^4 3d$ when both configurations belong to the same symmetry. The actual system is to be represented by the linear combination of $3s3p^6$ and $3s^23p^43d$ configurations; the $3s$ sub-shell hole is, in reality, partially filled by electron. The electric dipole transitions to fill the hole with electrons inevitably suffer modification by the configuration mixing. In spite of the simple appearance of the problems, theoretical calculations have not yet been tackled with sufficient accuracy. The anomalous behavior of the sp^6 and also the s^2p^4d configurations has been pointed out since a couple of decades. Cowan et al [4] discussed energy positions of the sp^6 state in neutral chlorine and other halogens in relations to the interaction with continuum configurations. Berrington et al [5] have made an R-matrix calculation for rare gas sub-valence hole states. Suzuki et al [6] have measured and calculated the lifetime of Ar^+ $3s$ sub-shell hole state.

We have calculated the sp^6 states of Ar^+, Kr^+, and Xe^+, and also calculated their lifetimes against the electric-dipole transition into s^2p^5 doublet states. The calculated lifetimes are given in the last column in table 1. For each ionic species, the upper entry gives Coulomb gauge (velocity form) calculation, and the lower entry gives Babushkin gauge (length form) calculation. We have also illustrated in table 2 the lifetime values for artificial states considering only the singly occupied ns sub-shell configurations and only the fully occupied ns^2 sub-shell configurations. We can see that the mixing of sp^6 and s^2p^4d configurations realizes the extreme lifetime elongation.

Table 1. Calculated lifetimes (in 10^{-9} seconds) of lowermost ^1S states with different sets of configurations for singly charged ions of argon, krypton, and xenon.

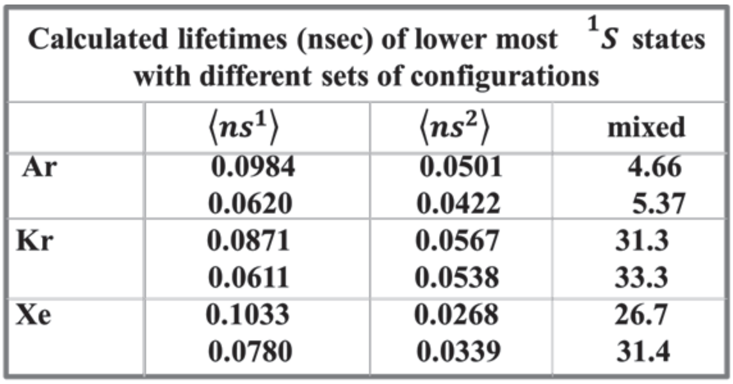

Calculated lifetimes (nsec) of lower most ^1S states with different sets of configurations

	$\langle ns^1\rangle$	$\langle ns^2\rangle$	mixed
Ar	**0.0984**	**0.0501**	**4.66**
	0.0620	**0.0422**	**5.37**
Kr	**0.0871**	**0.0567**	**31.3**
	0.0611	**0.0538**	**33.3**
Xe	**0.1033**	**0.0268**	**26.7**
	0.0780	**0.0339**	**31.4**

4. The fine structure levels of tungsten highly charged ions

Tungsten is thought as one of the good wall materials for magnetic confinement fusion reactor. Calculations for the properties of multiply charged tungsten ions are highly desired. W^{26+} ion is the simplest system with multiple $4f$-orbital electrons in the ground state. The ground state configuration of W^{26+} is $[\mathrm{Kr}]4f^2 = \cdots 4s^24p^64d^{10}4f^2$, and the magnetic dipole (M1) transitions between the fine structure levels in the ground state configurations enter in the wavelength range of the visible light. From the viewpoint of atomic physics, this system is interesting in the effects of correlations between the $4f$-orbital electrons. The atomic ground state has less difficulty for variational calculation; a large scale MCDF procedure is feasible for such systems. Recently, X. B. Ding et al [3] have made an extensive MCDF calculation for this system. They pointed out that the experimentally observed line at 389.4 nm is of the M1 transition between the first $^3H_5$ and the third $^3H_4$ fine structure levels with the calculated transition wavelength of 388.4 nm. To obtain the result, they optimized the all the possible 13 fine structure levels simultaneously by applying the EOL option for GRASP calculation. Because the whole range of the level energies extends to almost 20 eV, the optimum shape of the orbitals might differ between the higher most and lower most levels. In the present paper, we tried to improve the calculation by optimizing only the levels that are responsible for ${}^3H_5 - {}^3H_4$ transition, i.e., by applying the EOL option only for the first and the third fine structure levels. The results of calculation and the convergence feature of the present active space method are illustrated in table 2. And, the present result has been compared to the experiment in table 3.

Table 2. Convergence feature of W^{26+} ${}^3H_5 - {}^3H_4$ transition wavelength. The last column gives the difference of the wavelength from the immediately preceding calculation.

Basis included	Target levels to optimize	Wavelength (nm) of ${}^3H_5 - {}^3H_4$ line	Difference
minimal	1 ~ 13	395.859	
minimal	1,3	395.859	0.000
n=4, SD from 4d	1 ~ 13	393,466	2.393
n=4, SD from 4d	1, 3	390.097	3.369
n=4, SD from 4s,4p,4d	1, 3	389.098	0.999
n=4, 5d,5f, SD from 4s,4p,4d,4f	1, 3	389.098	0.000.

Table 3. Comparison of the present calculation with experiments and previous calculation [3].

Method	Wavelength (nm)
EBIT Experiment	**389.4**
LHD Experiment	**389.404 (6)**
Previous Calculation	**388.4**
Present Calculation	**389.1**

Acknowledgements

The present work has been partly supported by post Japan-China-Korea A3 Foresight Program and post Core University Program (Post CUP).

References

[1] Dyall K G *et al* 1989 *Comp. Phys. Communications* **55** 425. Parpia F A *et al* 1996 *Comp. Phys. Communications* **94** 249. Fritzsche S 2012 *Comp. Phys. Communications* **183** 1525. Joensson P *et al* 2007 *Comp. Phys. Communications,* **177** 597.

[2] Azuma Y *et al* 1995 *Phys. Rev. Lett.* **74** 3768.

[3] Ding X B *et al* 2012 *J. Phys. B: At. Mol. Opt. Phys.* **45** 035003

[4] Cowan R D *et al* 1974 J. Opt. Soc. Am. **64** 1474.

[5] Berrington K A *et al* 2001 J. Phys. B: At. Mol. Opt. Phys. **34** L149.

[6] Suzuki N *et al* 2016 *J. Phys. B: At. Mol. Opt. Phys.* **49** 145002.

Visible spectra of multiply charged heavy ions obtained with a compact electron beam ion trap

NAKAMURA Nobuyuki
Inst. for Laser Science, The Univ. of Electro-Communications, Tokyo 182-8585, Japan

Abstract

Visible spectra of multiply charged ions are useful not only for testing quantum mechanics theories but also for applications such as plasma diagnostics and precise atomic clocks. We present visible spectra of tungsten and lanthanide ions obtained with a compact electron beam ion trap.

Keywords: visible spectra multiply charged ions, electron beam ion trap

1.Introduction

Visible transitions in multiply charged heavy ions are of interest for many applications. For example, transitions in multiply charged W ions are in strong demand for the stable operation of the large scale fusion reactor ITER under construction. Since W is the material of the plasma facing wall of ITER, sputtered W ions are considered to be the main impurity in the ITER plasma [1]. Thus it is important to diagnose and control the W influx and charge evolution through spectroscopic diagnostics of W ions. Although all the wavelength ranges, including short wavelength ranges such as EUV and x-rays, are important for the diagnostics, transitions in the visible range are especially important due to the advantage that a variety of common optical components, such as mirrors, lenses, and fiber optics, can be applied.

As another example, optical transitions in multiply charged ions have been proposed for a new type of an optical clock that has a significantly enhanced sensitivity to the fine-structure constant variation due to the strong relativistic effects [2]. The variation of fundamental constants arises in many theories beyond the Standard Model of particle physics and is hinted by the astrophysical observations. Recently, it was suggested that dark matter may lead to oscillations of fundamental constants or transient effects that may be potentially detectable with such clocks [3]. It is also an advantage that the wavefunction of the electron tightly bound in a highly charged ion is less sensitive to the perturbation such as external fields.

In this contribution, we present visible spectra of multiply charged ions relevant to such applications obtained with a compact electron beam ion trap, called CoBIT [4]. Recent results for tungsten [5] and lanthanide ions [6] are compared with theoretical calculations.

2. Experiment

The present experiments were performed using a compact EBIT, called CoBIT. Detailed description of CoBIT is given in Ref. [4]. Briefly, it consists of an electron gun, a drift tube (DT), an electron collector, and a high-critical-temperature superconducting magnet. The DT is composed of three successive cylindrical electrodes that act as an ion trap by applying a positive trapping potential (typically 30 V) at both ends (DT1 and 3) with respect to the middle electrode (DT2). The electron beam emitted from the electron gun is accelerated towards the DT while it is compressed by the axial magnetic field (typically 0.08 T) produced by the magnet surrounding the DT. The space charge potential of the compressed high-density electron beam acts as a radial trap in combination with the axial magnetic field. Highly charged ions are produced through the successive ionization of the trapped ions. For producing tungsten ions, a vapor of tungsten hexacarbonyl $W(CO)_6$ was introduced through a gas injection system On the other hand, for producing lanthanide ions, the element of interest was introduced with an effusion cell. The temperature of the cell was 900 - 950 °C.

The setup for observing visible spectra was essentially the same as that used in our previous studies, where the visible emission lines of tungsten ions were observed [7, 8]. Briefly, the emission from the trapped lanthanide ions was focused by a convex lens on the entrance slit of a commercial Czerny-Turner type of visible spectrometer (Jobin Yvon HR-320) with a focal length of 320 mm. For survey observations, a 300 gr/mm grating blazed at 500 nm was used, whereas for wavelength determination, a high resolution 1200 gr/mm grating blazed at 400 nm was used. The diffracted light was detected with either a liquid-nitrogen-cooled back-illuminated CCD (Princeton Instruments Spec-10:400B LN) operated at -115 °C or a Peltier-cooled back illuminated CCD (Andor iDus 416) operated at -70 °C. The wavelength scale was calibrated using emission lines from several standard lamps placed outside CoBIT.

3. Results and discussion

Figure 1 shows tungsten spectra obtained with electron energies of 630 to 825 eV. As seen in the figure, most of the observed lines revealed a distinct appearance energy, from which the responsible ion for each line can be identified. For example, the lines at 389 nm and 464 nm observed in the 825 eV spectrum can be assigned as the transitions in W^{26+}

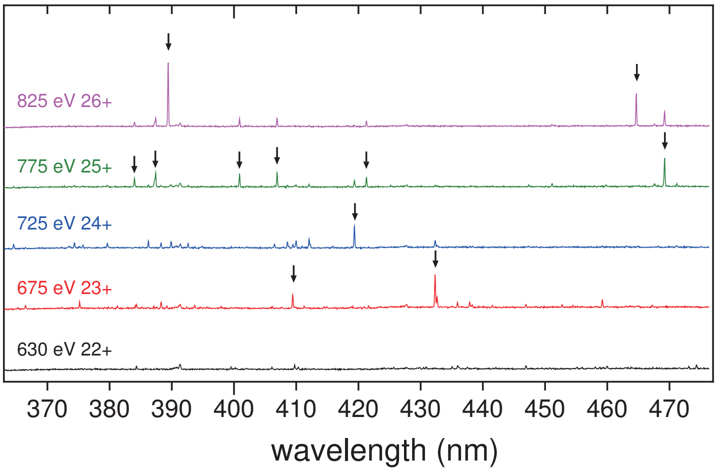

Figure 1: Visible spectra of highly charged W ions observed with a compact EBIT.

because their appearance energy is just above the ionization energy of W^{25+} (784 eV). Similarly, the lines marked by the arrows in the spectra of 775 eV, 725 eV, and 675 eV can be assigned as transitions in W^{25+}, W^{24+}, and W^{23+} respectively. As shown in this example, the charge state can be assigned to observed lines by observing the dependence on electron energy. However, it is generally difficult to identify the transition. Among the observed lines shown in Fig. 1, the W^{26+} lines at 389 nm and 464 nm have been identified through the comparison with theoretical calculation as $M1$ transitions between the fine structure levels in $4f^2\ {}^3H_J$, $J = 4 \leftarrow 5$ and $J = 5 \leftarrow 6$, respectively [7, 9]. The other lines, however, have not yet been identified due to the complexity increasing with the number of $4f$ electrons. This is only one instance, and many lines observed so far [8] are awaiting their identification.

Figure 2 shows visible spectra of Ho ($Z = 67$), Er (68), and Tm (69). From the energy dependence, the prominent peak in each spectrum has been assigned to the Ag-like ion of each element. The Ag-like isoelectronic sequence in this Z region has a simple configuration with only on valence electron in $4f$. The observed lines can thus be identified as the $M1$ transition between the doublet in the ground term ${}^2F$. We have also observed several lines of Cd-like ions, and identified them as $M1$ transitions between the fine structure levels of the ground state configuration $4f^2$ through the comparison with theoretical calculations [6]. The final goal of the present lanthanide spectroscopy is to identify visible line in Ho^{14+}, which has six $4f$ electrons in its ground state. We have observed electron energy dependence of Ho spectra, and assigned several lines to 14+ [10]. However, the complexity of the system prevent us to identify the transition. Further systematic studies

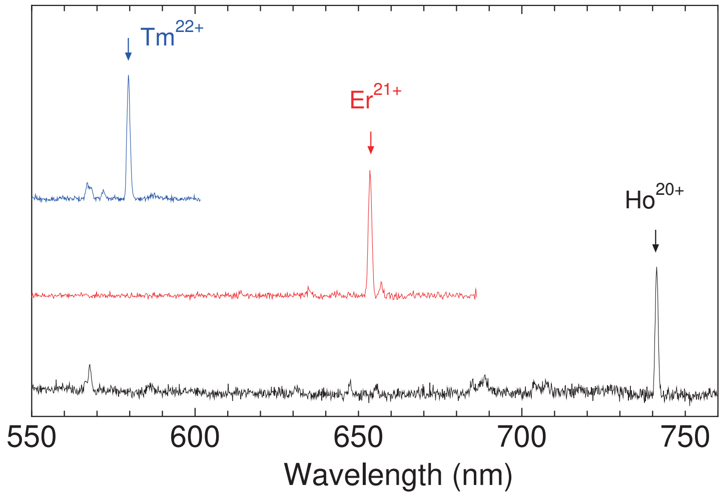

Figure 2: Visible spectra of highly charged W ions observed with a compact EBIT.

along isonuclear and isoelectronic sequences are needed.

Collaborators

Collaborators for tungsten work: Xiaobin Ding (NWNU), Chenzhong Dong (NWNU), Daiji Kato (NIFS), Fuihiro Koike (Sophia Univ.), Izumi Murakami (NIFS), Hiroyuki A. Sakaue (NIFS).
Collaborators for lanthanide work: Marianna S. Safronova (Univ. Delaware, Univ. Maryland), and Ulyana I. Safronova (Univ. Nevada).

References

[1] C. H. Skinner, Can. J. Phys. **86**, 285 (2008).
[2] J. C. Berengut *et al.*, Phys. Rev. Lett. **105**, 120801 (2010).
[3] A. Derevianko and M. Pospelov, Nature Phys. **10**, 933 (2014).
[4] N. Nakamura *et al.*, Rev. Sci. Instrum. **79**, 063104 (2008).
[5] M. Mita *et al.*, Atoms **5**, 13 (2017).
[6] S. Murata *et al.*, Phys. Rev. A **96**, 062506 (2017).
[7] A. Komatsu *et al.*, Phys. Scr. **T144**, 014012 (2011).
[8] A. Komatsu *et al.*, Plasma Fusion Res. **7**, 1201158 (2012).
[9] X.-B. Ding *et al.*, J. Phys. B **44**, 145004 (2011).
[10] T. Nakajima *et al.*, Nucl. Instrum. and Methods B **408**, 118 (2017).

Oscillator strengths and integral cross sections of the valence-shell excitations of oxygen molecule studied by fast electron and X-ray scattering

Ya-Wei Liu[1,2], Tao Xiong[1,2], Ke Yang[3], Nozomu Hiraoka[4], Ku-Ding Tsuei[4],
and Lin-Fan Zhu[1,2*]

[1]Hefei National Laboratory for Physical Sciences at Microscale and Department of Modern Physics, University of Science and Technology of China, Hefei, Anhui 230026, People's Republic of China

[2]Synergetic Innovation Center of Quantum Information and Quantum Physics, University of Science and Technology of China, Hefei, Anhui 230026, People's Republic of China

[3]Shanghai Institute of Applied Physics, Chinese Academy of Sciences, Shanghai 201204, People's Republic of China

[4]National Synchrotron Radiation Research Center, Hsinchu 30076, Taiwan, Republic of China

Abstract

The oscillator strengths and integral cross sections of the Schumann-Runge continuum, Longest-Band and Second-Band of oxygen molecule have wide applications in the studies of the Earth's atmosphere and the stellar atmospheres, but there still exist apparent discrepancies among the available data. In this work, the generalized oscillator strengths of the valence-shell excitations of oxygen have been determined independently by the high-energy electron scattering and high-resolution inelastic X-ray scattering. Based on the cross-checked generalized oscillator strengths, the optical oscillator strengths and integral cross sections of these excitations have been obtained, which give an independent cross-check to the previous experimental and theoretical results.

1. Introduction

The oscillator strengths and integral cross sections of the Schumann-Runge (SR) continuum, Longest-Band (LB) and Second-Band (SB) of oxygen molecule have significant applications in the studies of the Earth's atmosphere and the stellar atmospheres. Recently, molecular oxygen was detected by the Rosetta spacecraft in the coma of the comet 67P/CG for the first time [1]. Comets such as the comet 67P/CG, are the theorized candidates for the building blocks of bodies like Pluto, this naturally motivates a search for molecular oxygen in the atmosphere of Pluto by making use of the data sets acquired by the *New Horizons* mission during its flyby in 2015 July [2]. In the *New Horizons*, the Alice extreme-/far-ultraviolet imaging spectrograph [3] has the bandpass of 52 nm to 187 nm, which covers the SR continuum, LB and SB of oxygen. In order to explain the complex spectra observed, the OOSs and ICSs of the SR continuum, LB and SB of molecular oxygen are the basic and important input parameters for the theoretical modeling. However, serious discrepancies among the available data for the dynamic parameters still exist.

---

[*] Corresponding author's email: lfzhu@ustc.edu.cn

2. Experimental method

In this work, the generalized oscillator strengths (GOSs) of these excitations have been determined independently by the electron energy loss spectroscopy (EELS) and the high-resolution inelastic X-ray scattering (IXS). Typical energy-loss spectra of oxygen are shown in Fig. 1 along with the excited states assigned. The different experimental techniques provide a strict cross-check for the present GOSs of oxygen, which excludes the systematic error to a large extent. Then, the OOSs of oxygen have been obtained by extrapolating the present cross-checked GOSs to the limit of the squared momentum transfer $K^2 \rightarrow 0$, and the ICSs of oxygen in a wide energy region have been determined with the aid of the newly-developed *BE*-scaling method.

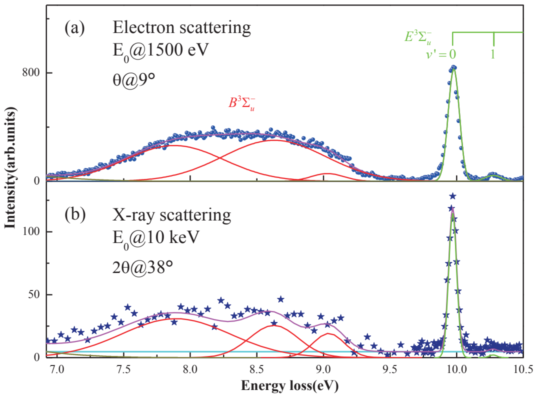

Fig. 1 Typical energy-loss spectra of the valence-shell excitations of molecular oxygen.

3. Results and discussion

The present GOSs of the SR continuum of oxygen measured by the high-energy EELS at 1500 eV and high-resolution IXS are shown in Fig. 2. It is clear in Fig. 2 that, the present GOSs of the SR continuum measured by the EELS and IXS are in excellent agreement, which indicates that the first Born approximation (FBA) is satisfied at 1500 eV in the whole squared momentum transfer region due to the fact that the IXS is

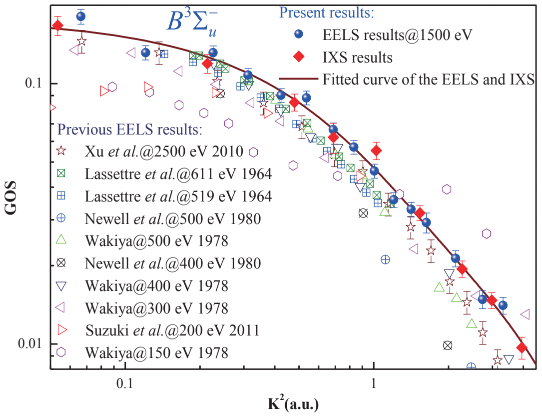

Fig. 2 The present and previous GOSs of the SR continuum $B^3\Sigma_u^-$ of oxygen.

free from the high-order Born terms [4]. As shown in Fig. 2, with the increasing of the incident electron energies the GOSs of Wakiya at 150-500 eV [5], Suzuki et al. at 200 eV [6], Newell et al. at 400 eV and 500 eV [7] and Lassettre et al. at 519 eV and 611 eV [9] approach to the present EELS and IXS GOSs gradually, which is in agreement with the asymptotic behaviors of the FBA.

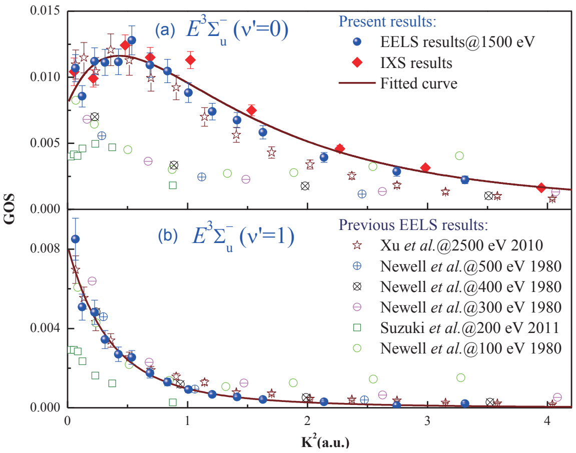

Fig. 3 The present and previous GOSs for (a): LB $E^3\Sigma_u^-(v'=0)$ and (b): SB $E^3\Sigma_u^-(v'=1)$ of oxygen.

The present GOSs of the LB and the SB of oxygen molecule by the high-energy EELS and high-resolution IXS are shown in Fig. 3. It is clear in Fig. 3(a) that, the present GOSs of the LB measured by the EELS and IXS are in excellent agreement, which indicates the FBA is also satisfied at 1500 eV for the LB in the whole squared momentum transfer region. It is clear from Fig. 3(a) that, the GOSs of Newell et al. at 100-500 eV [7] and Suzuki et al. at 200 eV [6] are obviously lower than the present ones. So the FBA is not satisfied for the GOSs of the LB of oxygen at the low incident electron energies less than 500 eV. As for the weak SB, it is clear in Fig. 3(b) that, the present EELS GOSs of the SB at 1500 eV are in reasonable agreement with the ones of Newell et al. at 400 eV and 500 eV [7] and Xu et al. at 2500 eV [8].

The accurate OOSs of oxygen are determined by extrapolating the present GOSs to the limit $K^2 \rightarrow 0$ and are shown in Fig. 4. As shown in Fig. 4(a), the present OOSs for the SR continuum, LB and SB of oxygen are in excellent agreement with the EELS results of Chan et al. [10] and Lassettre & Skerbele [9], while the discrepancies can be noticed with the ones of Huebner et al. [11] and Wakiya [5] except for the OOS of the SB. It is clear from Fig. 4(b) that, although the strong SR continuum is thought that it should not be subject

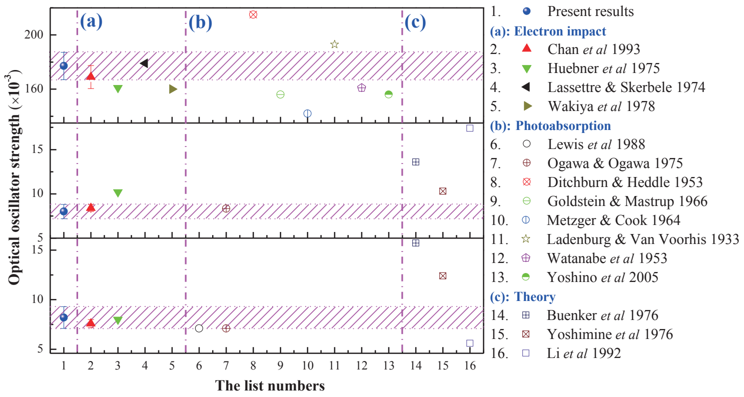

Fig. 4 The present and previous OOSs of the SR continuum, LB and SB of oxygen from top to bottom.

to the line-saturation effects due to its broad nature [9], the apparent discrepancies between the present OOS and the photoabsorption results [12-17] are still observed, even for the recent photoabsorption result of Yoshino et al. [17]. Meanwhile, the present OOS of LB and SB of oxygen are in reasonable agreement with the photoabsorption OOSs [18-19], which may be free from the line-saturation effect due to their broader nature of the LB and SB of oxygen. In theory (see Fig. 4(c)), Buenker et al. [20], Yoshimine et al. [21] and Li et al. [22] have calculated the OOSs of the LB and SB of oxygen by the ab initio configuration interaction method. It is clear that, the present results of the LB and SB of oxygen are obviously different from the theoretical OOSs [18-19].

According to the present cross-checked GOSs, the *BE*-scaled ICSs of the SR continuum, LB and SB of oxygen were determined in a wide energy region by the BE-scaling method. It is clearly seen in Fig. 5 that, the present *BE*-scaled ICSs are slightly higher than the *BE*-scaled ICSs of Xu et al. [8] and the *BEf*-scaled ICSs of Suzuki et al. [6], but are in excellent agreement with the experimental ICSs of Suzuki et al. at 15-200 eV [6] and Wakiya at 150-500 eV [5]. Meanwhile, it is clear in Fig. 5 that, the present *BE*-scaled ICSs of the SR continuum of oxygen are lower than the early experimental ICSs of Trajmar et al. [23], Wakiya [5] and Shyn et al. [24] at the low-incident electron energies (⩽100 eV) except the experimental ICS of Shyn et al. [24] at 50 eV.

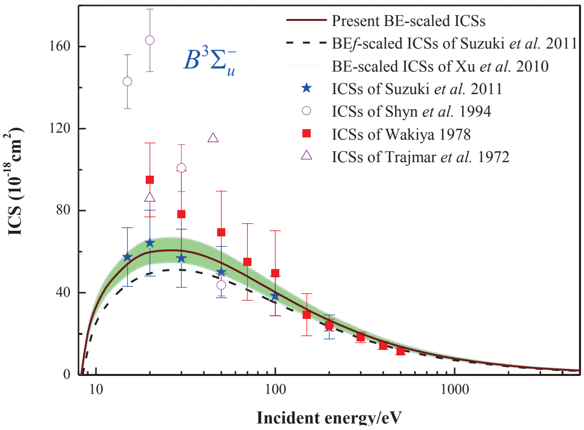

Fig. 5 The present *BE*-scaled ICSs and the previous ICSs of the SR continuum of oxygen. The presently estimated uncertainties are shown as the shadow region.

It can be seen in Fig. 6(a) that, the present *BE*-scaled ICSs of the LB are obviously higher than the *BE-/BEf-* scaled ICSs of Xu et al. [8] and Suzuki et al. [6] at the low- and moderate-incident electron energies. Based on the obvious discrepancies [6] between their *BEf*-scaled ICSs and experimental ICSs [6] for the LB, Tanaka et al. [25] thought that the well-known Rydberg-valence perturbation influences the LB [20,26], and results in the failure of the *BEf*-scaling method for the determination of the ICSs of the LB of oxygen. However, as shown in Fig. 6(a), the reasonable agreement between the present *BE*-scaled ICSs and the experimental ICSs of Suzuki et al. [6] indicates that, the BE-scaling method may still be valid for the determination of the ICSs of the LB of oxygen based on the present cross-checked GOSs. As for the ICSs of the SB, it can be seen clearly in Fig. 6(b) that the present *BE*-scaled ICSs of the SB are slightly higher that

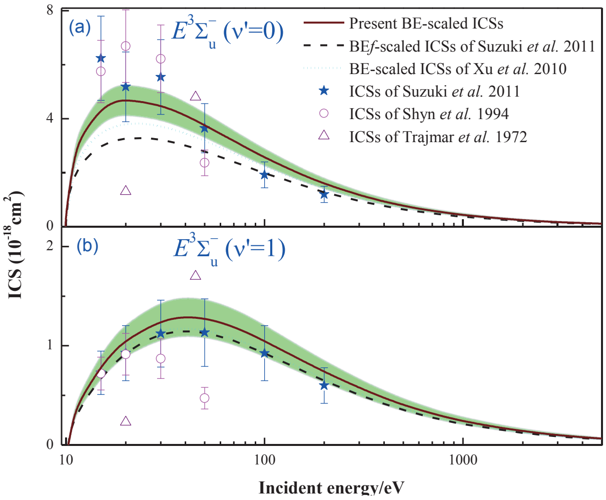

Fig. 6 The present *BE*-scaled ICSs and the previous ICSs of the LB and the SB of oxygen. The presently estimated uncertainties are shown as the shadow region.

the *BE-/BEf-* scaled ICSs of Xu et al. [8] and Suzuki et al. [6], but are in reasonable agreement with the experimental ICSs of Shyn et al. [27] at 15 and 20 eV and Suzuki et al. at 15-200 eV [6] within the experimental uncertainties except the experimental ICSs of Shyn et al. [27] at 30 and 50 eV.

4. Summary and conclusion

In this work, the GOSs of the SR continuum, LB and SB of oxygen have been determined by the high-energy EELS and high-resolution IXS. Based on the present cross-checked GOSs, the OOSs and ICSs of the SR continuum, LB and SB of oxygen have been determined. The present OOSs and *BE*-scaled ICSs of the SR continuum, LB and SB of molecular oxygen play a vital role in modeling the abundance of oxygen in the atmospheres of Earth, Venus, Saturn, Pluto, Europa, and other outer planets and satellites, and are important for improving these atmospherical models.

Acknowledgements

This work is supported by the National Key Research and Development Program of China (Grant Nos. 2017YFA0402300 and 2017YFA0303500) and the National Natural Science Foundation of China (Grant Nos. 11504361, U1732133 and 11320101003). The IXS experiment was carried out in a beam time approved by Japan Synchrotron Radiation Research Institute (Proposal No.2016A4265) and National Synchrotron Radiation Research Center, Taiwan, Republic of China (Proposal No. 2016-2-022-1).

References

[1] Bieler, A., Altwegg, K., Balsiger, H., et al. 2015, Nature, 526, 678
[2] Kammer, J. A., Stern, S. A., Young, L. A., et al. 2017, Astron. J., 154, 55
[3] Stern, S. A., Slater, D. C., Scherrer, J., et al. 2008, Space. Sci. Rev., 140, 155
[4] Xie, B. P., Zhu, L. F., Yang, K., et al. 2010, Phys. Rev. A., 82, 032501
[5] Wakiya, K. 1978, J. Ph. B: Atom. Molec. Phys., 11, 3913
[6] Suzuki, D., Kato, H., Ohkawa, M., et al. 2011, J. Chem. Phys., 134, 064311

[7] Newell, W. R., Khakoo, M. A., & Smith, A. C. H. 1980, J. Ph. B: Atom. Molec. Phys., 13, 4877

[8] Xu, W. Q., Sun, J. M., Wang, Y. Y., & Zhu, L. F. 2010, Phys. Rev. A., 82, 042716

[9] Lassettre, E. N., Silverman, S. M., & Krasnow, M. E. 1964, J. Chem. Phys., 40, 1261

[10] Chan, W. F., Cooper, G., & Brion, C. E. 1993, Chem. Phys., 170, 99

[11] Huebner, R. H., Celotta, R. J., Mielczarek, S. R., & Kuyatt, C. E. 1975, J. Chem. Phys., 63, 241

[12] Ladenburg, R., & Van Voorhis, C. C. 1933, Phys. Rev., 43, 315

[13] Watanabe, K., Inn, E. C. Y., & Zelikoff, M. 1953, J. Chem. Phys., 21, 1026

[14] Ditchburn, R. W., & Heddle, D. W. O. 1953, Proc. R. Soc. London, Ser. A., 220, 61

[15] Metzger, P. H., & Cook, G. R. 1964, J. Quant. Spectrosc. Radiat. Transf., 4, 107

[16] Goldstein, R., & Mastrup, F. N. 1966, J. Opt. Soc. Am., 56, 765

[17] Yoshino, K., Parkinson, W. H., Ito, K., & Matsui, T. 2005, J. Mol. Spectrosc., 229, 238

[18] Lewis, B. R., Gibson, S. T., et al. 1988, J. Quant. Spectrosc. Radiat. Transf., 40, 469

[19] Ogawa, S., & Ogawa, M. 1975, Can. J. Phys., 53, 1845

[20] Buenker, R. J., Peyerimhoff, S. D. et al. 1976, Chem. Phys. Lett., 42, 383

[21] Yoshimine, M., Tanaka, K., Tatewaki, H., et al. 1976, J. Chem. Phys., 64, 2254

[22] Li, Y., Honigmann, M., Bhanuprakash, K., et al. 1992, J. Chem. Phys., 96, 8314

[23] Trajmar, S., Williams, W., & Kuppermann, A. 1972, J. Chem. Phys., 56, 3759

[24] Shyn, T. W., Sweeney, C. J., Grafe, A., & Sharp, W. E. 1994, Phys. Rev. A., 50, 4794

[25] Tanaka, H., Brunger, M. J., Campbell, L., et al. 2016, Rev. Mod. Phys., 88, 025004

[26] Lewis, B. R., England, J. P., Gibson, S. T., Brunger, M. J., & Allan, M. 2001, Phys. Rev. A., 63, 022707

[27] Shyn, T. W., Sweeney, C. J., & Grafe, A. 1994, Phys. Rev. A., 49, 3680

Electron-ion recombination of Be-like Ca

Shu-Xing Wang[1], Zhong-Kui Huang[2], Wei-Qiang Wen[2], Simon Preval[3], N. R. Badnell [4], Stefan Schippers[5], Han-Bing Wang[2], Li-Jun Dou[2], Xin-Wen Ma[2] and Lin-Fan Zhu[1*]

[1] Hefei National Laboratory for Physical Sciences at Microscale and Department of Modern Physics,
University of Science and Technology of China (USTC), Hefei, Anhui 230026, P. R. China
[2] Institute of Modern Physics, Chinese Academy of Sciences, 730000 Lanzhou, P. R. China
[3]Department of Physics and Astronomy, University of Leicester, University Road, Leicester, LE1 7RH, UK
[4]Department of Physics, University of Strathclyde, Glasgow G4 0NG, UK
[5]I. Physikalisches Institut, Justus-Liebig-Universität Gießen, D-35392 Giessen, Germany

Abstract

Electron-ion recombination rate coefficients of Be-like Ca in the center of mass energy from 0 to 51.88 eV have been measured by means of merged-beam technique at the main cooler storage ring (CSRm). The calculation conducted with AUTOSTRUCTURE code was also presented and compared with the experimental results. Dielectronic recombination associated with $2s^2$ [$^1S_0$] → $2s2p$ [$^3P_{0,1,2}$,$^1P_1$] and trielectronic recombination associated with $2s^2$ [$^1S_0$] → $2p^2$ [$^3P_{0,1,2}$,$^1D_2$,$^1S_0$] transitions have been measured. In addition, recombination of parent ions at the $2s2p$ $^3P_0$ meta-stable state has also been identified from the measured spectrum. Plasma recombination rate coefficients in the temperature range of 10^3-10^8 K were derived from the measured recombination rates and compared with the results from the AUTOSTRUCTURE code as well as previous calculations. An agreement of better than 25% iss found for the collisionally ionized plasmas while the discrepancies are higher for photo-ionized plasmas.

1. Introduction

Astronomy is primarily an observational science by detecting photons. Various types of space-based observatories, such as, Solar Maximum Mission (NASA), Solar and Heliospheric Observatory (NASA) and XMN-Newton (ESA), have been launched to collect high-resolution X-ray data [1]. Electron-ion collision processes which can result in line emissions, in particular, radiative recombination (RR) and dielectronic recombination (DR), are consequently important sources of radiations in astrophysical plasmas. Thus, DR rate coefficients are required to interpret the observed spectra by plasma modeling. In addition, electron-ion recombination rate coefficients and electron impact ionization cross sections are essential for deducing the charge state distribution in a plasma. Furthermore, determination of the man-made or astrophysical plasma properties, such as the thermal structure and elemental abundances, requires accurate charge state distribution data [2, 3]. Reliable recombination rate coefficients are required for understanding and modeling laboratorial or astrophysical plasmas, while most available rate coefficients are from theory. However, the prediction of DR resonance positions and strengths at low energy range by different theories is still a challenging task since an infinite number of states are involved in DR process and relativistic many body effects should be taken into account in high orders. Presently available atomic structure codes are not able to provide resonance positions in the low energy region with sufficient precision. Therefore, accurate experimental DR rate

Table 1. Fitted parameters for the resonant recombination channels derived from experimental and calculated rate coefficients. The unit of c_i and E_i are 10^{-5}cm^{-3}s^{-1}K$^{3/2}$ and eV, respectively.

No.	Experiment		AUTOSTRUCTURE (n_{max}=1000)	
i	c_i	E_i	c_i	E_i
1	5.022	0.554	3.623	0.058
2	6.169	0.038	47.571	1.307
3	260.089	3.252	151.739	4.801
4	453.854	1.715	257.922	2.001
5	1193.660	9.227	825.993	10.562
6	2916.733	23.188	1610.587	25.048
7	6298.331	57.720	5795.376	60.088

coefficients are required to benchmark different theoretical methods to produce more reliable electron-ion recombination data.

Calcium was found to be one of the most abundant element in the solar system [4, 5]. The solar atmosphere contains plasma at all temperatures and the solar element abundances can reflect the element abundances in the universe [6]. Line emissions caused by $2s2p\ ^1P_1$ - $2s^2\ ^1S_0$ transition of Ca XVII at 192.8 Å were widely observed in X-ray solar flare spectra by the Extreme-Ultraviolet Imaging Spectrometer (EIS) on Hinode [7]. Observation of the Tycho supernova remnant by XMM-Newton and Cassiopeia A by Chandra have also shown the strong emission from the calcium ions [8, 9]. A summary of the spectral lines for Ca XVII can be found in a topical review by Doschek & Feldman [6] and the atomic data table summarized by Landi & Bhatia [10]. Laboratory study of the spectra of highly ionized calcium in the 100-250 Å range applied to solar flare diagnostics had also been made with TEXT tokamak [11].

Our experimental results constitute a series of benchmark data for use in astrophysical and fusion plasmas. The comparison between the measured and calculated resonances proposed that the theoretical model for calculate the TR resonance strengths still needs some improvement.

2. Experimental result

The details of the experiment and the theoretical calculations can be found in the recent published papers [12, 13]. Fig. 1 presents the measured electron-ion merged-beam recombination rate coefficients as well as the theoretical calculation by AUTOSTRUCTURE code. The comparison shows that the DR resonances can be calculated with a high precision for both the resonance positions and strengths. However, the TR resonance strengths cannot be produced very well within the present theoretical model. Most of the TR resonance strengths were underestimated by the theoretical calculation.

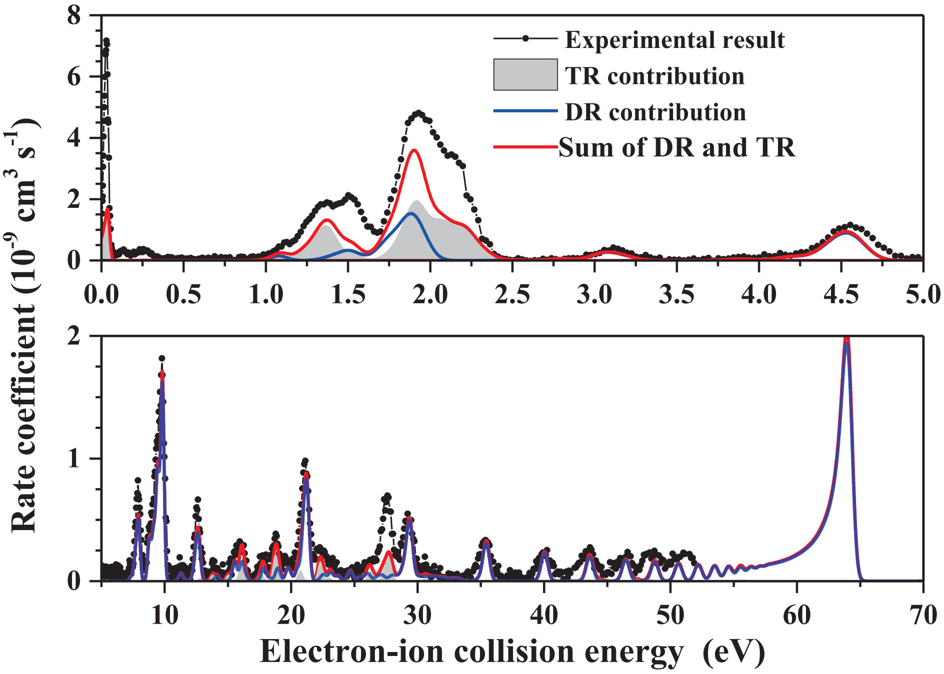

Fig. 1 Present measured merged-beam electron-ion recombination rate coefficients compared with the separate theoretical calculation with AUTOSTRUCTURE code.

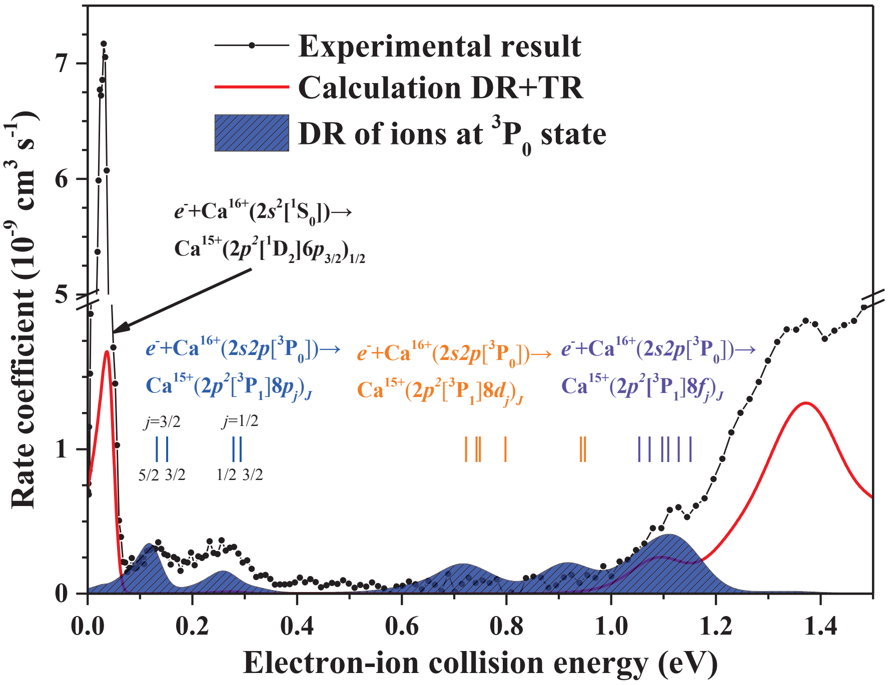

Fig. 2 Electron-ion recombination resonances at low collision energies. DR associated with parent ions at the $2s2p$ $^3P_0$ state has been identified in the measured spectrum.

Considering that the lifetime of the $2s2p$ $^3P_0$ meta-stable state is rather long (~7.8×10^5s) compared to the experimental time scale, the ions at other meta-stable states will decay to the ground-state since their lifetimes are much shorter than the delay time for ion beam cooling before the measurement. A fraction of about 5% ions stored in the ring were estimated at this state. Several extremely strong resonances originating from the parent ions at the meta-stable state have been identified from the measurement. Fig. 2 shows the results of DR from metastable state. The present study proposed a chance to investigate the lifetime of the $2s2p\ ^3\mathrm{P}_0$ state decay to the ground-state by E1M1 two-photon transition.

In addition, for applications in astrophysics and fusion plasmas, the plasma recombination rate coefficients have been derived from the present measured recombination rates and compared with the AUTOSTRUCTURE calculation and previous calculated results (see [13] for discussions in detail). For convenient use in plasma modeling codes, the plasma rate coefficients have been fitted with the formula below:

$$\alpha(T_e) = T_e^{-3/2} \sum_i c_i \exp\left(-\frac{E_i}{kT_e} \right) \quad (1.1).$$

The associated fitting parameters are listed in the Table. 1.

Acknowledgements

This work is partly supported by the National Key R&D Program of China under grant No. 2017YFA0402300, the National Natural Science Foundation of China through No. 11320101003, No. U1732133, No. 11611530684, the Strategic Priority Research Program of the Chinese Academy of Sciences, grant No. XDB21030300 and the Key Research Program of Frontier Sciences, CAS, grant No. QYZDY-SSW-SLH006. The authors acknowledges the post Japan-China-Korea A3 Foresight Program and post Core University Program (Post CUP).

References

[1] Paerels F B *et al* 2002 *Annu. Rev. Astron. Astrophys.* **41** 291

[2] Savin D W & Laming J M 2003 *Astrophys. J.* **566** 1166

[3] Beiersdorfer P 2003 *Annu. Rev. Astron. Astrophys.* **41** 343

[4] Asplund M *et al* 2013 *Annu. Rev. Astron. Astrophys.* **47** 481

[5] Feldman U & Laming J M 2000 *Phys. Scr.* **61** 222

[6] Doschek G A & Feldman U 2000 *J. Phys. B: At. Mol. Opt. Phys.* **43** 232001

[7] Ko Y K *et al* 2009 *Astrophys. J.* **697** 1956

[8] Decourchelle A *et al* 2001 *A & A* **365** L218

[9] Hwang U & Laming, J. M. 2003 *Astrophys. J.* **597** 362

[10] Landi E & Bhatia A K *et al* 2009 *At. Data Nucl. Data Tables* **95** 155

[11] Lippmann S *et al* 1987 *Astrophys. J.* **316** 819

[12] Huang Z K *et al* 2018 *Astron. Astrophys. Suppl. Ser.* **235**:2(8pp)

[13] Wang S X *et al* 2018 *Astrophys. J.* **862**:134(7pp)

Statistical Analysis of Hydrogen Recycling in the Peripheral Region of LHD

Takuya Osugi[1*], Masahiro Hasuo[1], Keisuke Fujii[1]

[1]Graduate School of Engineering, Kyoto University, Kyoto Nishikyo-ku, Kyoto 615-8246, Japan

Abstract

In order to understand the behavior of atoms and plasma particles in the peripheral region of the Large Helical Device (LHD), the ion particle outflux to the divertor plates and the hydrogen atom influx to the plasma are statistically investigated using the ion saturation current and the Balmer-α emission intensity measured in multiple diagnostic ports. The correlations among the AC components of the ion saturation current are large between the pairs of port 2-4, 2-6 and 4-6. The correlations among the AC components of the Balmer-α emission intensity are large in all the ports. The correlations between these two measurements are large in ports 2, 4 and 6. These results suggest that the ion particle outflux is non-axisymmetric, that the hydrogen atoms generated in some ports instantaneously spread to all the ports, and that the hydrogen atoms are mainly generated from the direct recombination in the port 2, 4, and / or 6.

1. Introduction

In magnetic confined fusion plasmas, it is one of important studies to control particle recycling at the plasma facing components such as first wall and divertor for improvement of the confinement performance [1]. The behavior of atoms and charged particles in the peripheral region are determined by a lot of elementally processes such as recombination, absorption and sputtering. Since there are huge uncertainties not only in the reaction rates but also in the plasma parameters near the divertor region, it is difficult to evaluate their behaviors from the first principle quantitatively. In the Large Helical Device (LHD), the recycling flux has been estimated from the particle flux on the divertor plates by the particle balance model [2]. However, this model gives a lower estimation of the divertor recycling flux by assuming the rate of the ion particle loss that does not reach the divertor plates equals to 0 than without assumption.

In this study, we fit a statistical model to experimental data of ion saturation current on the divertor plate and Balmer-α emission intensity measured for LHD plasmas, and quantified the correlations among measurement data in multiple ports.

2. Experiment

Figure 1 (a) shows a schematic top view of LHD. LHD was designed 10-fold rotational symmetry in the toroidal direction. The Langmuir probes were embedded in the divertor plates in the port 2, 4, 6, 7, 8, 9 and 10. Each of them measured the ion saturation current for the LHD plasma (shot number 137144). The sampling frequency was 200 Hz. The Balmer-α emissions from this plasma were measured in the port 2, 3, 5 ,6, 7, 8, 9 and 10. The sampling frequency was 200 Hz. In this paper, measurement data of the ion

---

[*] Corresponding author's email: osugi.takuya.85u@st.kyoto-u.ac.jp

saturation current and the Balmer-α emission intensity in port p are denoted by $i_{\mathrm{is}}^{(p)}$ and $I_{\mathrm{H}}^{(p)}$, respectively. Figure 1 (b) shows temporal evolution of $i_{\mathrm{is}}^{(2)}$ and $I_{\mathrm{H}}^{(2)}$ measured for this plasma.

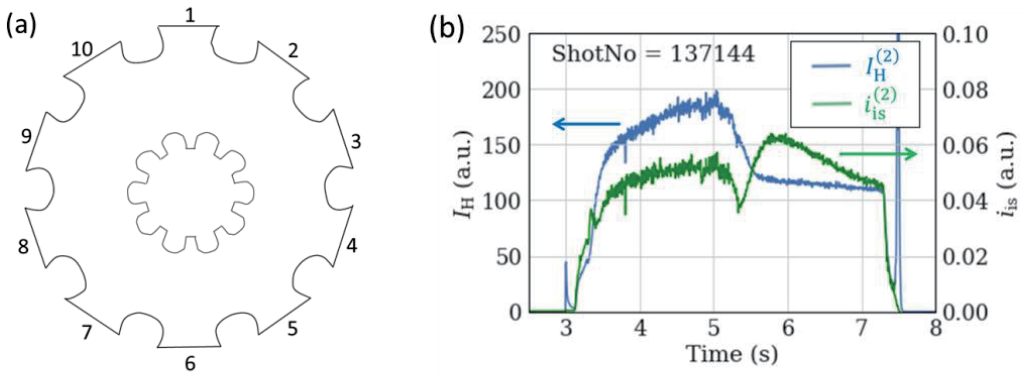

Fig. 1 (a) Schematic top view of LHD. (b) Measurement data of the Balmer-α intensity in port 2, $I_{\mathrm{H}}^{(2)}$ (blue line, left axis), and the ion saturation current in port 2, $i_{\mathrm{is}}^{(2)}$ (green line, right axis). The superscripts of $I_{\mathrm{H}}^{(2)}$ and $i_{\mathrm{is}}^{(2)}$ denote the port numbers.

As can be seen in Fig. 1 (b), these two measurements have the rapidly fluctuating components in addition to their slow trends. In this study, we focus on the fluctuation component of these data.

We extracted the AC component by subtracting the DC component of these two measurements, which were obtained from a 5-point moving average. Typical AC components of $i_{\mathrm{is}}^{(p)}$ and $I_{\mathrm{H}}^{(p)}$ are shown in Fig. 2 (a) and Fig. 2 (b), respectively.

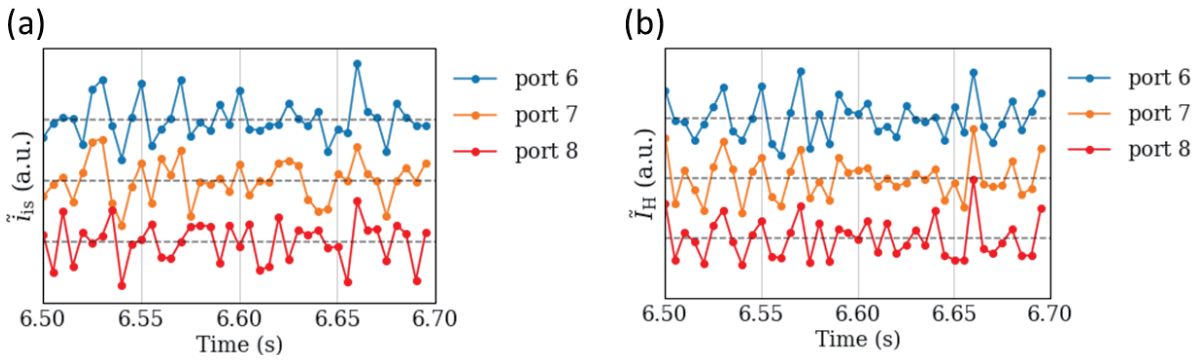

Fig. 2 (a) Temporal evolution of $\widetilde{i_{\mathrm{is}}}^{(6)}$, $\widetilde{i_{\mathrm{is}}}^{(7)}$ and $\widetilde{i_{\mathrm{is}}}^{(8)}$ at $t = 6.5\sim6.7$ s, where $\widetilde{i_{\mathrm{is}}}^{(p)}$ denotes the AC component of $i_{\mathrm{is}}^{(p)}$. The mean values of these measurements are properly shifted for the cleaner view. (b) Temporal evolution of $\widetilde{I_{\mathrm{H}}}^{(6)}$, $\widetilde{I_{\mathrm{H}}}^{(7)}$ and $\widetilde{I_{\mathrm{H}}}^{(8)}$ at $t = 6.5\sim6.7$ s, where $\widetilde{I_{\mathrm{H}}}^{(p)}$ denotes the AC component of $I_{\mathrm{H}}^{(p)}$.

$i_{is}^{(p)}$ and $I_{\mathrm{H}}^{(p)}$ are assumed to be proportional to the ion particle outflux to the divertor plate and the hydrogen atom influx to the plasma, respectively. Then the following relation is obtained,

$$\tilde{\Gamma}_{\mathrm{i}}^{(p)} \propto \widetilde{i_{\mathrm{is}}}^{(p)} \tag{1}$$

where $\tilde{\Gamma}_{\mathrm{i}}^{(p)}$ is the AC component of the ion particle outflux in port p, $\Gamma_{\mathrm{i}}^{(p)}$.

3. Statistical Modeling for particle fluxes

In order to understand plasma wall interactions, the surveys have been conducted taking various generation paths for hydrogen into consideration [3]. The generation paths are classified into two in terms of the time scale. Some atoms are generated by the recombination (radiative, three body, charge exchange, surface assisted recombinations) from ions and electrons and go into the plasma. We call this path as direct recycling. On the other hand, some other atoms are absorbed into divertor plate or first walls, and released after some conditions are met, e.g. the temperature increase of the material (indirect recycling). The direct recycling occurs in the time scale determined by the elementary process rate ($\sim 10^6$ /s), while the time scale of the indirect one should be larger than the direct one because this time scale depends on the divertor temperature, which doesn't change rapidly.

Let $\mathit{\Gamma}_{\mathrm{H}}^{(p)}$ be the neutral hydrogen atom influx from the divertor plate in port p. $\mathit{\Gamma}_{\mathrm{H}}^{(p)}$ is expected to be written as a sum of direct recombination effect, which equals to $\mathit{\Gamma}_{\mathrm{i}}^{(p)}$, and slow-time-scale indirect recombination effect. We approximate this relation by the following form,

$$\tilde{\mathit{\Gamma}}_{\mathrm{H}}^{(p)} = \tilde{\mathit{\Gamma}}_{\mathrm{i}}^{(p)} + \varepsilon^{(p)} \tag{2}$$

where $\tilde{\mathit{\Gamma}}_{\mathrm{H}}^{(p)}$ is the AC component of $\mathit{\Gamma}_{\mathrm{H}}^{(p)}$, while $\varepsilon^{(p)}$ approximates the remaining cause of the atom generation in port p. We further approximate $\tilde{\mathit{\Gamma}}_{\mathrm{i}}^{(p)}$ and $\varepsilon^{(p)}$ follow independent zero-mean Gaussian distribution functions,

$$\tilde{\mathit{\Gamma}}_{\mathrm{i}}^{(p)} \sim \mathcal{N}\left(0, \left(\sigma_{\mathrm{i}}^{(p)}\right)^2\right) \tag{3}$$

$$\varepsilon^{(p)} \sim \mathcal{N}\left(0, \left(\sigma_{\varepsilon}^{(p)}\right)^2\right) \tag{4}$$

where $\left(\sigma_{\mathrm{i}}^{(p)}\right)^2$ and $\left(\sigma_{\varepsilon}^{(p)}\right)^2$ are variance of $\tilde{\mathit{\Gamma}}_{\mathrm{i}}^{(p)}$ and $\varepsilon^{(p)}$, respectively. Under these assumptions, $\tilde{\mathit{\Gamma}}_{\mathrm{i}}^{(p)}$ and $\tilde{\mathit{\Gamma}}_{\mathrm{H}}^{(p)}$ follow a multivariate Gaussian distribution,

$$p\left(\begin{bmatrix} \tilde{\mathit{\Gamma}}_{\mathrm{i}}^{(p)} \\ \tilde{\mathit{\Gamma}}_{\mathrm{H}}^{(p)} \end{bmatrix}\right) = \mathcal{N}\left(\begin{bmatrix} 0 \\ 0 \end{bmatrix}, \begin{bmatrix} \left(\sigma_{\mathrm{i}}^{(p)}\right)^2 & \left(\sigma_{\mathrm{i}}^{(p)}\right)^2 \\ \left(\sigma_{\mathrm{i}}^{(p)}\right)^2 & \left(\sigma_{\mathrm{i}}^{(p)}\right)^2 + \left(\sigma_{\varepsilon}^{(p)}\right)^2 \end{bmatrix}\right) \tag{5}$$

The correlation coefficient between $\tilde{\mathit{\Gamma}}_{\mathrm{i}}^{(p)}$ and $\tilde{\mathit{\Gamma}}_{\mathrm{H}}^{(p)}$ is

$$\mathrm{cor}\left[\tilde{\mathit{\Gamma}}_{\mathrm{i}}^{(p)}, \tilde{\mathit{\Gamma}}_{\mathrm{H}}^{(p)}\right] = \sqrt{\frac{\left(\sigma_{\mathrm{i}}^{(p)}\right)^2}{\left(\sigma_{\mathrm{i}}^{(p)}\right)^2 + \left(\sigma_{\varepsilon}^{(p)}\right)^2}} \tag{6}$$

When this correlation coefficient is large, $\left(\sigma_{\varepsilon}^{(p)}\right)^2$ is smaller than $\left(\sigma_{\mathrm{i}}^{(p)}\right)^2$. Then $\tilde{\mathit{\Gamma}}_{\mathrm{i}}^{(p)}$ in Eq. (1) becomes dominant compared with $\varepsilon^{(p)}$. Therefore, this suggests that hydrogen atoms are mainly generated from the direct recombination of ions on the divertor plates and in the peripheral region.

In order to investigate hydrogen recycling based on this model, we calculate correlation coefficients among $\widetilde{i_{\mathrm{IS}}}^{(p)}$ and $\widetilde{I_{\mathrm{H}}}^{(p)}$ in different toroidal position and those between $\widetilde{i_{\mathrm{IS}}}^{(p)}$ and $\widetilde{I_{\mathrm{H}}}^{(p)}$ in a time window of 150 ms. These results are shown in the next section.

4. Results

The correlations among the ion particle outfluxes were evaluated from the ion saturation currents based on Eq. (1). Figure 3 (a) and (b) show the scatter diagrams of $\widetilde{i_{\mathrm{IS}}}^{(4)}$ versus $\widetilde{i_{\mathrm{IS}}}^{(6)}$ and $\widetilde{i_{\mathrm{IS}}}^{(4)}$ versus

$\widetilde{i_{\mathrm{is}}}^{(8)}$, respectively. The correlation coefficient in Figure. 3 (a) is large while that in Fig. 3 (b) is small. Figure 3 (c) shows the correlation coefficients between all the pairs of $\widetilde{i_{\mathrm{is}}}^{(p)}$. As can be seen in Fig. 3 (c), $\mathrm{cor}[\widetilde{i_{\mathrm{is}}}^{(2)}, \widetilde{i_{\mathrm{is}}}^{(4)}]$, $\mathrm{cor}[\widetilde{i_{\mathrm{is}}}^{(2)}, \widetilde{i_{\mathrm{is}}}^{(6)}]$ and $\mathrm{cor}[\widetilde{i_{\mathrm{is}}}^{(4)}, \widetilde{i_{\mathrm{is}}}^{(6)}]$ were larger than the others.

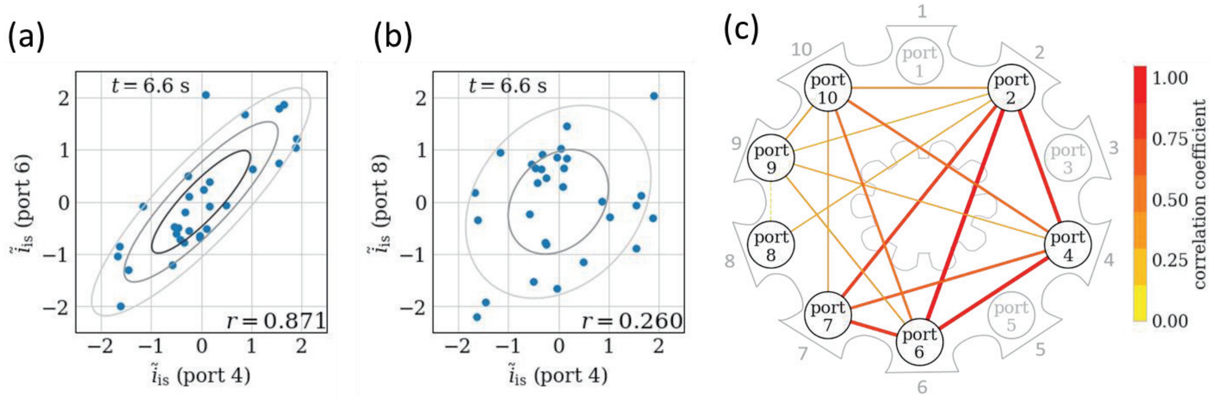

Fig. 3 (a) and (b) are scatter diagrams of $\widetilde{i_{\mathrm{is}}}^{(4)}$ versus $\widetilde{i_{\mathrm{is}}}^{(6)}$ and $\widetilde{i_{\mathrm{is}}}^{(4)}$ versus $\widetilde{i_{\mathrm{is}}}^{(8)}$ in a time window of 150 ms at $t = 6.6$ s, respectively. Each variable is normalized to mean 0 and standard deviation 1. The correlation coefficient r is shown in the lower right of each figure. (c) Correlation coefficients between all the pairs of $\widetilde{i_{\mathrm{is}}}^{(p)}$, which is indicated by the color of the lines.

The correlations among the temporal changes of the hydrogen atom influxes were evaluated from the AC components of the Balmer-α emissions. Figure 4 (a) shows the scatter diagram of $\widetilde{I_{\mathrm{H}}}^{(3)}$ versus $\widetilde{I_{\mathrm{H}}}^{(6)}$. Figure 4 (b) shows the correlation coefficients between all the pairs of $\widetilde{I_{\mathrm{H}}}^{(p)}$. As can be seen in Fig. 4 (b), the correlation coefficients of all the pairs of $\widetilde{I_{\mathrm{H}}}^{(p)}$ are more than 0.8.

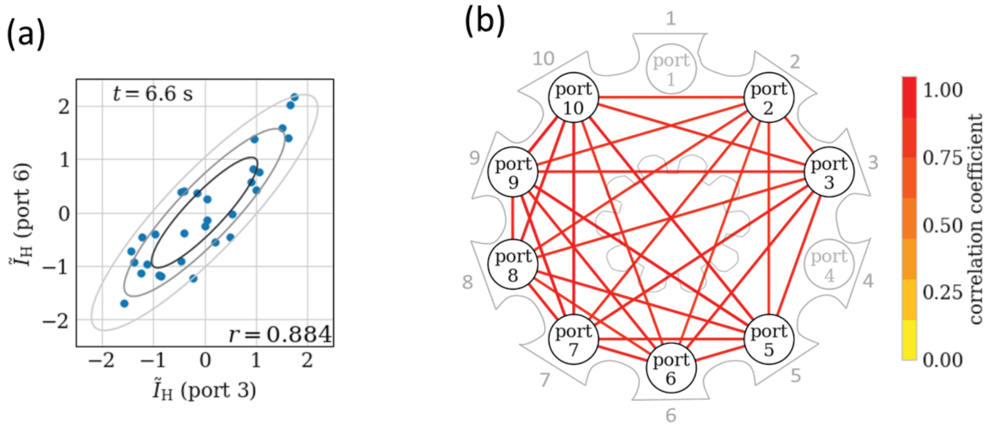

Fig. 4 (a) Scatter diagram of $\widetilde{I_{\mathrm{H}}}^{(3)}$ versus $\widetilde{I_{\mathrm{H}}}^{(6)}$ in a time window of 150 ms at $t = 6.6$ s. (b) Correlation coefficients of all the pairs of $\widetilde{I_{\mathrm{H}}}^{(p)}$.

The correlation coefficients between the ion particle outflux and the hydrogen atom influx were evaluated by that between $\widetilde{i_{\mathrm{is}}}^{(p)}$ and $\widetilde{I_{\mathrm{H}}}$, where $\widetilde{I_{\mathrm{H}}}$ is the averaged values of $\widetilde{I_{\mathrm{H}}}^{(p)}$ for all the ports. Figure 5 shows the result of $\mathrm{cor}[\widetilde{i_{\mathrm{is}}}^{(p)}, \widetilde{I_{\mathrm{H}}}]$ in all the ports. As can be seen in Fig. 5, $\mathrm{cor}[\widetilde{i_{\mathrm{is}}}^{(2)}, \widetilde{I_{\mathrm{H}}}]$,

$\mathrm{cor}\left[\widetilde{i_{\mathrm{IS}}}^{(4)}, \widetilde{I_{\mathrm{H}}}\right]$ and $\mathrm{cor}\left[\widetilde{i_{\mathrm{IS}}}^{(6)}, \widetilde{I_{\mathrm{H}}}\right]$ are larger than the others.

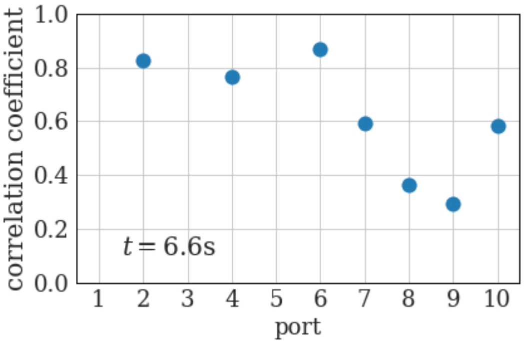

Fig. 5 Correlation coefficients between $\widetilde{I_{\mathrm{H}}}$ and $\widetilde{i_{\mathrm{IS}}}^{(p)}$ in a time window of 150 ms at $t = 6.6$ s.

5. Discussion

From the correlation analysis of the ion saturation current, it is found that the ion particle outflux from the plasma to the divertor plate fluctuates coherently in port 2, 4 and 6, and those to other ports behaves independently, i.e., the ion particle outflux is non-axisymmetric. On the other hand, the Balmer-α intensity has a large correlation in all the ports. Because the Balmer-α intensity is proportional to the neutral particle influx to the plasma [4] but not the generation flux of atoms; this large correlation indicates either of the following two hypotheses; hydrogen atoms are generated at all the divertor plates axisymmetrically, or the generation of hydrogen atoms itself is asymmetric but they instantaneously spread to all the ports resulting in axisymmetric particle influx and Balmer-α emission intensity fluctuation. However, the strong correlation between the Balmer-α intensity and the ion saturation current at the particular port suggests the latter one, i.e. the hydrogen atoms are mainly generated in the port 2, 4, and / or 6. Note that it is not possible in the current analysis to evaluate which ports are the dominant generation ports because the Balmer-α intensity fluctuates coherently with the hydrogen atom influx in the dominant generation ports.

In this work, we performed statistical analysis of the Balmer-α intensity and the ion saturation current. The correlation coefficient among the AC components of the ion saturation current are larger between the ports 2-4, 2-6 and 4-6 than the others. The correlation coefficients among the AC components of the Balmer-α intensity are larger than 0.8. The correlation coefficients between these two measurements are larger in port 2, 4 and 6 than the others. As the results, we found the followings; the ion particle outflux is non-axisymmetric, the hydrogen atoms generated in some ports instantaneously spread to all the ports, and the hydrogen atoms are mainly generated from the direct recombination in the port 2, 4, and / or 6.

Acknowledgements

The authors would like to thank preparation of the seminar by post Japan-China-Korea A3 Foresight Program and post Core University Program (Post CUP). This work is supported by NIFS.

References

[1] U Samm and the TEXTOR-94 Team 1999 *Plasma. Phys. Control. Fusion* **41** B57

[2] Miyazawa J *et al* 2004 *Nucl. Fusion* **44** 154

[3] D. E. Post *J. Nucl. Mater.* 220-222 (1995) 143-157

[4] U. Wenzel, M. Goto *J. Nucl. Mater* 415 (2011) S1170-S1173

Three-body fragmentation dynamics of CF_4^{2+} induced by 1 keV electron collision

Lei Chen[1], Zhenjie Shen[1], Enliang Wang[2], Xi Zhao[1], Xu Shan[1], Xiangjun Chen[1*]

[1]Hefei National Laboratory of Physical Sciences at the Microscale and Department of Modern Physics,
University of Science and Technology of China, Hefei 230026, China.
[2]Max Plank Institute for Nuclear Physics, Heidelberg 69117, Germany.

Abstract

We report the investigation on three-body fragmentation of CF_4^{2+} induced by 1 keV electron collision utilizing a newly built ion momentum spectrometer. With the help of coincidence measurement, more than seven dissociation channels are observed. For the fragmentation of CF_4^{2+} into F^++CF_2^++F, three dissociation pathways are identified, including one sequential and two concerted pathways. Kinetic energy release distributions for these pathways are deduced. We found that one concerted pathway is the predominated, and the sequential breakup is likely to take place through highly-excited electronic states of CF_4^{2+}.

1. Introduction

Investigations on dissociative ionization of molecules are of intensive interest in physics, chemistry as well as biology. One of the major challenges in this area is to comprehend the molecular bond cleavage selectivity [1]. The past few decades have witnessed tremendous progresses in the development of coincidence momentum imaging techniques [2, 3], making it feasible to reveal multi-body fragmentation dynamics for small molecules.

The CF_4 molecule, in its ground states, has a tetrahedral structure with high symmetry. It is an important plasma etching gas in the semiconductor industry and also a potent greenhouse gas in the earth atmosphere. Although CF_4 has been extensively studied by plenty of experimental methods [4, 5], reports on the breakup mechanics are still scarce.

In this work, the three-body fragmentation of CF_4^{2+} into F^++CF_2^++F is studied. The precursor ion, CF_4^{2+}, is created by electron impact at 1 keV energy. The two fragment ions are detected in coincidence by a momentum imaging system. By employing the Dalitz plot [6] and Newton diagram, two concerted and one sequential fragmentation pathways are identified. We deduced the kinetic energy release distributions for these three pathways and found that the sequential breakup is likely to take place through highly-excited electronic states of CF_4^{2+}.

2. Experimental Setup

The experiment was performed using a recently built ion momentum spectrometer. As shown in Fig. 1, a pulsed electron beam from a photoelectron emission gun collides with the gas target in the reaction zone. The electrons are emitted from a Tantalum cathode that is illuminated by a 266 nm pulsed laser (…). The repetition frequency and pulse duration of the laser are 20 kHz and less than 600 ps, respectively. The spot size of the electron beam is collimated to about 1 mm diameter at the reaction zone. After the collision, the electron beam is dumped and monitored by a Faraday cup, which comprises a 1 mm inner cup and a 6 mm diameter outer cup. An effusive gas target is introduced into the reaction zone by a copper capillary mounted on a three-dimensional manipulator. The internal diameter and length of the capillary are 0.1 mm and 60 mm, respectively. After the collision of electrons with the molecular target, a pulsed extraction field will be triggered on. The fragment ions are accelerated and analyzed by a Wiley-Mclaren type time of flight (TOF) mass spectrometer [7] towards a two-dimensional (2D) time- and position- sensitive detector (PSD), which consists of a pair of microchannel plates (MCP) of 100 mm diameter in chevron configuration and followed by a delay line anode. Momentum vector of each ion can be obtained by the time of flight and position on the detector.

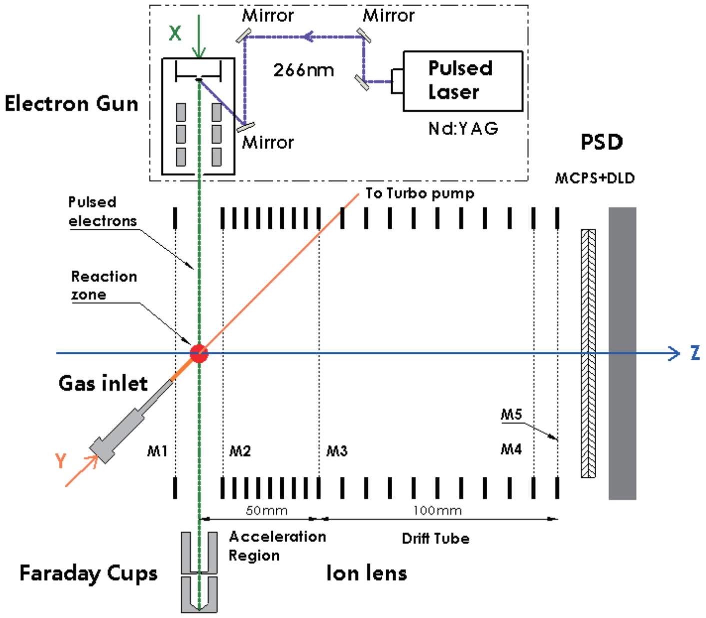

Fig. 1 Schematic graph of Ion Momentum Spectrometer

In the experiment, the electric field of the acceleration region is kept at 50 V/cm. M1 to M5 are Molybdenum meshes installed to create uniform electric fields. The reaction chamber is pumped by a 700 l/s (Pfeiffer Hipace700) turbo-pump. The background pressure is better than 2×10^{-6} Pa and the working pressure is about 4×10^{-5} Pa.

3. Results and Discussion

Fig. 2 shows the ion-ion coincidence map of the CF_4 fragmentation, where more than seven fragmentation channels can been observed. The thee-body dissociation channel $CF_4^{2+} \longrightarrow F^+ + CF_2^+ + F$ is labeled by a red oval. The momenta of the two ionic fragments (F^+ and CF_2^+) are obtained directly from their TOF and positions on the detector. The momentum of neutral F atom is deduced by using the principle of momentum conservation. It is worthwhile to mention that the fragment channels of CF_4^{q+} ($q\geq3$) have not been observed in present experiment.

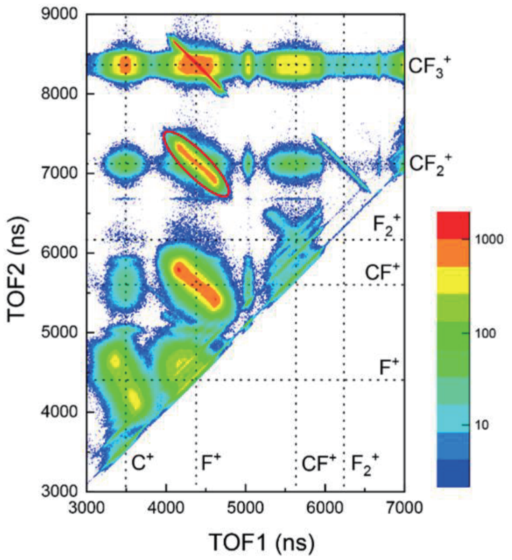

Fig. 2 Ion-ion coincidence map observed in the fragmentation of CF_4 induced by 1 keV electron impact.

In order to identify the fragmentation mechanisms of this channel, we employ the Dalitz plot [6]. It is a powerful analytic tool for visualization of three-body fragmentation processes. Each point in the plot represents a specific momentum correlation in terms of the normalized energies of the fragments. The Dalitz plot for the channel $CF_4^{2+} \longrightarrow F^+ + CF_2^+ + F$ is shown in Fig. 3(a), where the three distinct regions (labelled I, II, and III) can be clearly observed. We adopt Newton diagrams to directly visualize the momentum correlation of the three fragments in these three regions in Fig. 3(b)-(d). In the diagrams, the normalized momentum vectors of the fragments are plotted with one of them fixed at the x-axis and the other two plotted on the upper and lower halves of the diagram.

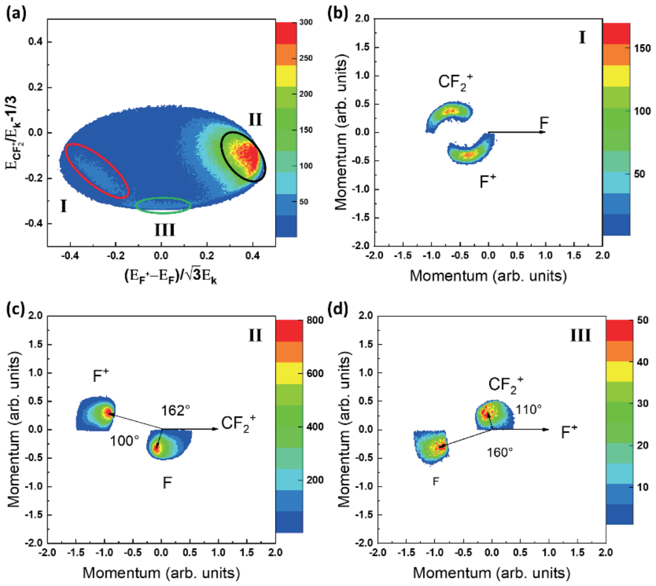

Fig. 3 (a) Dalitz plot of CF_4^{2+} dissociation into $F^+ + CF_2^+ + F$; (b) Newton diagram for region I; (c) Newton diagram for region II; (d) Newton diagram for region III.

The Newton diagram for region I is shown in Fig. 3(b), where a circular structure can be clearly observed. This structure is due to the rotation of CF_3^{2+} before the final charge separation and the neutral F atom is lost at the first step. Therefore, the events in region I originate from sequential breakup, i.e. $CF_4^{2+} \longrightarrow F + CF_3^{+} \longrightarrow F^{+} + CF_2^{+} + F$. Fig. 3(c) presents the Newton diagram for Region II. Both of the momenta of F^{+} and F scatter on a localized area along the x-axis, indicating the existence of a concerted breakup. From the Dalitz plot in Fig. 3(a), we know pathway II is the dominated one. As shown in Fig. 3(d), the Newton diagram for Region III is a little like that of region II. The difference is, in this case, F atom obtains more momentum than CF_2^{+}, revealing another concerted breakup pathway. However, it is not usual for the neutral fragment to obtain more energy than the charged ones, because Coulomb forces are usually stronger between charged ions. So we propose that a charge transfer process may occur. That is, after the breakup, F^{+} captures one electron and becomes a neutral F atom.

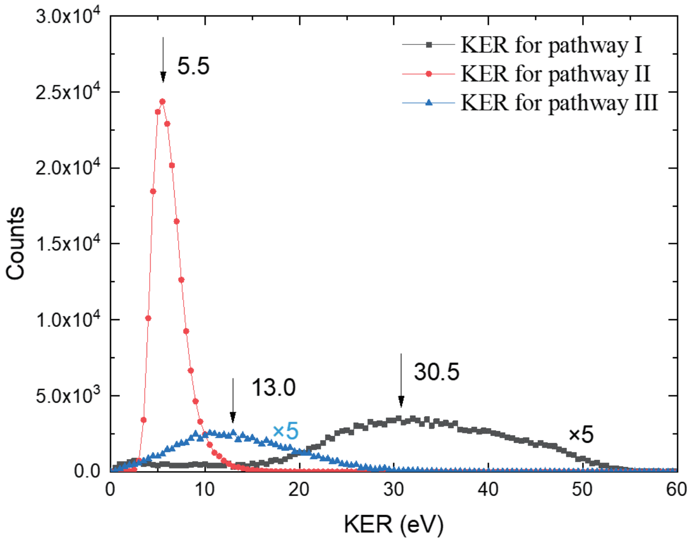

Fig. 4 KER distributions for different dissociation pathways.

Fig. 4 demonstrates the KER distributions for pathway I, II and III. The peak values are 30.5 eV, 5.5 eV and 13.0 eV, respectively. The KER for pathway I (the sequential breakup) distributes on higher energy side. This indicates that the sequential pathway may take place through high-lying states of CF_4^{2+}.

4. Conclusion

To conclude, we built a new ion momentum spectrometer for investigating fragmentation dynamics of polyatomic molecules. Three-body dissociation of CF_4^{2+} into $F^{+} + CF_2^{+} + F$ is studied in present experiment. Three breakup pathways are identified and their KER distributions are obtained. We found that concerted breakup (pathway II) is the dominated one among the three pathways. And sequential breakup (pathway I) is likely to happen through the high-lying states of CF_4^{2+}.

Acknowledgements

This work is supported by the National Key Research and Development Program of China (2017YFA0402300) and the National Natural Science Foundation of China (11534011).

References

[1] Neumann N et al 2010 *Phys. Rev. Lett.* **104** 103201.

[2] Dörner R et al 2000 *Phys. Rep.* **330** 95.

[3] Ullrich J et al 2003 *Rep. Prog. Phys.* **66** 1463.

[4] Codling K et al 1991 *J. Phys. B: At. Mol. Opt. Phys.* **24** 951.

[5] Motohashi K et al 2003 *J. Phys. B: At. Mol. Opt. Phys.* **36** 1811.

[6] Dalitz R H 1953 *Philos. Mag.* **44** 1068.

[7] Wiley W C and McLaren I H 1955 *Rev. Sci. Instrum.* **26** 1150.

The 7th China- Japan-Korea Joint Seminar on Atomic and Molecular Processes in Plasma (AMPP2018)
Scientific Program

23 July 2018 (Monday)

Registration: 15:00-21:00

24 July (Tuesday)

Session 1 (Opening & Category) Chair: L.Q. Hu (ASIPP)	08:30		**Registration**
	09:00		**Announcement & Introduction**
	09:10		**Welcome address**
	09:20		**Welcome address**
	09:30		**Opening remark & Group photo**
	09:40	L. Wang (ASIPP)	Progress of Advanced Steady State Operation & Plasma-Wall Interaction Control in EAST
	10:05	H. Q. Liu (ASIPP)	Overview of the EAST diagnostics
Coffee Break 10:30-10:50			
Session 2 Chair: C.Z. Dong (NWNU)	10:50	L.F. Zhu (USTC)	Comparative investigations of atomic and molecular dynamic parameters by fast-electron and inelastic x-ray scattering
	11:15	M. Takahashi (Tohoku Univ.)	Recent progress in (e,2e) electron momentum spectroscopy of atoms and molecules
	11:40	S.X. Tian (USTC)	Ion momentum imaging study of the ion-molecule reactions of Ar$^+$ + NO and Ar$^+$ + N$_2$
Lunch Break12:05-14:00			
Session 3 Chair: N. Nakamura (UEC)	14:00	H. Tanuma (TMU)	Soft X-ray emissions from inner-shell excited Li-like ions in charge transfer collisions of meta-stable He-like ions with neutral gases
	14:25	J. L. Zeng (NUDT)	Triple-core hole states produced in the interaction of solid-state density plasmas with a relativistic femtosecond optical laser
	14:50	Y.Z Qu (UCAS)	Theoretical studies on multiple Auger process of hollow atom
	15:15	Daiji Kato (NIFS)	Statistical tests for oscillator strength distributions of Lanthanide elements
	15:40	Y. Tachibana (Tohoku Univ.) (15 min)	Development of electron impact spectroscopy for directly observing the nuclear motions in molecular systems
Coffee Break 15: 55-16:15			
Session 4 Chair: J.M. Yuan (GSCAEP)	16:15	B. He (IAPCM)	Ab initio simulation of the energy loss experiment for alpha particles moving in discharged H plasmas
	16:40	D.H. Kwon (KAERI)	Optical emission spectroscopy and collisional radiative modeling for Ar plasma
	17:05	Y.M. Yu (IOP,CAS)	Proposal of highly charged ions for atomic clock with 10^{-19} accuracy
Bus 17:40			

25 July (Wednesday)

Session 9 **Chair:** Y. Z. **Qu** (UCAS)	08:30	S. Morita (NIFS)	Estimation of photon emission coefficients in tungsten UTA transitions using LHD plasmas
	08:55	K. Fuji (Kyoto Univ.)	Experimental evaluation of fractional abundance data for W^{23+}–W^{28+}
	09:20	T. Esaka (Kyoto Univ.) (15 min)	Estimating the emission spectra of W^{23+} - W^{30+} by the numerical decomposition of multiple spectra observed from LHD plasmas
	09:35	L. Zhang (ASIPP)	Estimation of density profile of W^{43+}-W^{45+} in EAST H-mode plasma
Coffee Break 10:00- 10:20			
Session 10 **Chair:** D.H. Kwon (KAERI)	10:20	J. Yu (SJTU)	Diagnostics of laser-induced plasma during its evolution in the background gas over different of times scales
	10:45	H.B. Ding (DLUT)	Diagnosis of atomic and ionic species in laser-induced tungsten plasma using TOF-MS and LIBS
	11:05	Q. Min (NWNU)	Experimental and theoretical investigation of radiation and dynamics properties in laser-produced plasmas
	11:30	C. Gao (NUDT)	Ultrafast nonequilibrium electron dynamics in a solid-density aluminum interacting with an ultra-intense ultrafast x-ray pulse
Lunch Break 12:15 – 14:00			
Session 11 Chair Y. Wu (IAPCM)	14:00	J.M. Yuan (GSCAEP)	Temporal space localization of electrons ejected from continuum atomic processes in hot dense plasma
	14:25	F. Koike (Sophia Univ.)	A consideration on the accuracy of GRASP calculations
	14:50	Q.P.Wang (USTC)	Spectrometer techniques development – a brief review
	15:15	Y. T. Zhao (XJU)	Stopping and transportation of ion beam in plasma
15:40-17:40			
Session 12	15:40	EAST Tour	
Session 13	16:40	Post session at EAST Hall	
Bus 17:40			

26 July (Thursday)

Session 14 Chair: F. Koike (Sophia Univ.)	08:30	N. Nakamura (UEC)	Visible spectra of multiply charged heavy ions obtained with a compact electron beam ion trap
	08:55	G. Xiong (CAEP)	Experimental studies on the atomic processes related ICF plasmas at Shanghai-EBIT
	09:20	C. J. Shao (IMP)	Production of K-shell hollow atoms in collisions with swift heavy ions
	09:45	Y.W. Liu (USTC)	Oscillator strengths and integral cross sections of the valence-shell excitations of oxygen molecule studied by fast electron and inelastic X-ray scattering

Coffee Break 10:10 - 10:30			
Session 15 **Chair:** **J. L. Zeng** (NUDT)	10:30	Jun. Jiang (NWNU)	Atomic Polarizabilities for high-precision measurement of atomic spectra
	10:55	Y. Yang (Fudan Univ.)	High-resolution tungsten spectroscopy relevant to the diagnostic of high-temperature tokamak plasmas
	11:20	S.X. Wang (USTC)(15min)	DR and TR rate coefficients of Be-like Ca
	11:35	T. Osugi (Kyoto Univ) (15 min)	Statistical Analysis of Hydrogen Recycling in the Peripheral Region of LHD
	11:40	L. Chen (USTC)(15 min)	Three-body fragmentation dynamics of CF_4^{2+} induced by 1 keV electron collision
Summary of the Seminar (Daiji Kato, NIFS)			
Lunch Break 12:10 – 14:00			

Collection of Abstracts

Oscillator strengths and integral cross sections of the valence-shell excitations of oxygen molecule studied by fast electron and inelastic X-ray scattering

Lin-Fan Zhu[1], **Ya-Wei Liu**

Hefei National Laboratory for Physical Sciences at Microscale and Department of Modern Physics, University of Science and Technology of China, Hefei, Anhui 230026, People's Republic of China
Synergetic Innovation Center of Quantum Information and Quantum Physics, University of Science and Technology of China, Hefei, Anhui 230026, People's Republic of China

The oscillator strengths and integral cross sections of the Schumann-Runge(SR) continuum, Longest-Band(LB) and Second-Band(SB) of oxygen molecule have significant applications in the studies of the Earth's atmosphere and the stellar atmospheres. Recently, molecular oxygen was detected by the Rosetta spacecraft in the coma of the comet 67P/CG for the first time [1]. Comets such as the comet 67P/CG [1], are the theorized candidates for the building blocks of bodies like Pluto, this naturally motivates a search for molecular oxygen in the atmosphere of Pluto by making use of the data sets acquired by the *New Horizons* mission during its flyby in 2015 July [2]. In the *New Horizons*, the Alice extreme-/far-ultraviolet imaging spectrograph [3] has the bandpass of 52 nm to 187 nm, which covers the SR continuum, LB and SB of oxygen. In order to explain the complex spectra observed, the OOSs and ICSs of the SR continuum, LB and SB of molecular oxygen are the basic and important input parameters for the theoretical modeling. However, serious discrepancies among the available data for the dynamic parameters still exist.

In this work, the generalized oscillator strengths (GOSs) of these excitations have been determined independently by the high-energy electron-scattering and the high-resolution inelastic X-ray-scattering. Typical energy-loss spectra of oxygen are shown in Figure 1 along with the excited states assigned. The different experimental techniques provide a strict cross-check for the present GOSs of oxygen, which excludes the possibility of any systematic error. Then, the OOSs of oxygen have been obtained by extrapolating the present cross-checked GOSs to the limit of the squared momentum transfer $K^2 \to 0$, and the ICSs of oxygen have been determined in a wide energy region with the aid of the newly-developed BE-scaling method.

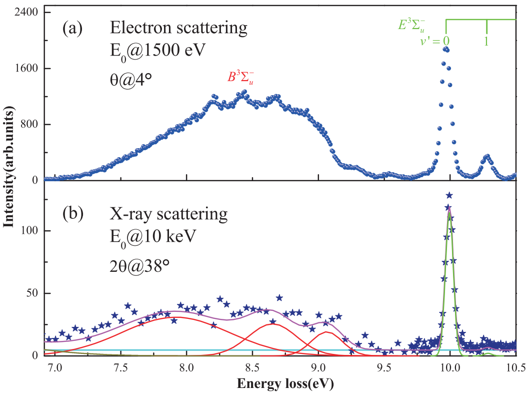

Fig. 1. The typical energy-loss spectra of the valence-shell excitations of molecular oxygen. (a): a electron energy loss spectrum at 4°; (b): a high-resolution inelastic X-scattering spectrum at 38°, solid lines are the fitted curves.

The present data can be used as the basic input parameters of the theoretical models for the astronomical observations, and are helpful to deepen our understanding of the atmospheres of the Earth, Venusian, Saturn, Pluto, Europa, and other oxygen-rich planets and satellites.

References

[1] A. Bieler et. al., 2015 *Nature.* **526** 678.

[2] J.A. Kammer, S.A. Stern et. al., 2017 *Astron. J.* **154** 55.

[3] S.A. Stern, D.C. Slater et. al., 2008 *Space. Sci. Rev.* **140** 155.

---

[1] E-mail: lfzhu@ustc.edu.cn

Recent progress in (e,2e) electron momentum spectroscopy of atoms and molecules

Masahiko Takahashi [1]

Institute of Multidisciplinary Research for Advanced Materials, Tohoku University, Sendai 980-8577, Japan

Over the last half-century an experimental method has been developed for looking at the spatial distributions of each electron orbital in momentum space. The method, called electron momentum spectroscopy (EMS) [1], is a sort of (e, 2e) spectroscopy and is a kinematically-complete electron-impact ionization experiment under the Compton scattering conditions [2]. The value of EMS lies in the exciting possibility of measuring Compton profiles associated with target electrons at different energy levels separately. Note that from consideration of the nature of the Fourier transform Compton profiles are expected to be particularly sensitive to the behavior of the outer, loosely bound valence electrons that are of central importance in chemical properties such as bonding, chemical reactivity, and molecular recognition. One is thus capable to realize momentum space chemistry by using EMS. Indeed, the idea of such momentum space chemistry can be traced back to the early 1940's. For instance, in 1941 a series of theoretical papers [3] were reported by C. A. Coulson who greatly contributed to understanding of chemical bonding.

In spite of the unique ability, however, application of EMS had largely been limited to studies on electronic structure of atoms and simple molecules, due mainly to its inherently small cross sections. Under those circumstances, we have joined this research field, in 1992. Firstly, we have improved the collection efficiency of EMS measurements, eventually by a factor of nearly 500,000 through a series of development of a multi-channel coincidence technique [4, 5]. We have then started various kinds of attempts to exploit the unique ability of EMS for momentum space chemistry [6]. For instance, measurements of 3-dimensional electron momentum densities of gaseous, isolated molecules have for the first time been made [7], as well, such as the first experimental determination of spatial orientations of the constituent atomic orbitals in molecular orbitals [8] and studies on distortion of molecular orbitals due to molecular vibration [9].

Extension of the applicability of EMS to transient species is also one of the challenges to be tackled, because the change of electron motion is the driving force behind chemical reactions. We have therefore developed time-resolved EMS (TR-EMS) by replacing the continuous incident electron beam with 5-kHz electron pulses, each having 1 ps temporal width [10], and applied it to the highest occupied molecular orbital (HOMO) of a molecular excited state with a life time of 13.5 ps [11], opening the door to time-resolved orbital imaging for chemical reactions [12]. Furthermore, we are additionally developing a time-resolved version of atomic momentum spectroscopy (TR-AMS) [13], which aims to measure in real time the momentum distribution of each atom with different mass numbers in a decaying system. We believe that the joint use of TR-EMS and TR-AMS would provide a completely new, momentum-space approach to studying chemical reaction dynamics.

References

[1] E. Weigold, I.E. McCarthy, *Electron Momentum Spectroscopy* (Kluwer/Plenum, New York, 1999).
[2] *Compton Scattering*, ed. by B. Williams (McGraw-Hill, New York, 1977).
[3] C.A. Coulson and W.E. Duncanson, 1941 *Proc. Cambridge Philos. Soc.* **55** 67, 74, 397, 406.
[4] M. Takahashi, T. Saito, M. Matsuo, Y. Udagawa, 2000 *Rev. Sci. Instrum.* **73** 2242.
[5] M. Yamazaki, M. Takahashi *et al.*, 2011 *Meas. Sci. Technol.* **22** 075602.
[6] M. Takahashi, 2009 *Bull. Chem. Soc. Jpn.* **82** 751.
[7] M. Takahashi *et al.*, 2005 *Phys. Rev. Lett.* **94** 213202.
[8] N. Watanabe, X.J. Chen, M. Takahashi, 2012 *Phys. Rev. Lett.* **108** 173201.
[9] N. Watanabe, M. Yamazaki, M. Takahashi, 2012 *J. Chem. Phys.* **137** 114301.
[10] M. Yamazaki, M. Takahashi *et al.*, 2013 *Rev. Sci. Instrum.* **84** 063105.
[11] M. Yamazaki, M. Takahashi *et al.*, 2015 *Phys. Rev. Lett.* **114** 103005.
[12] Research Highlights, 2015 *Nature* **59** 392.
[13] M. Yamazaki, M. Hosono, Y. Tang, M. Takahashi, 2017 *Rev. Sci. Instrum.* **88** 063103.

---

[1] E-mail: masahiko@tohoku.ac.jp

Ion momentum imaging study of the ion-molecule reactions of $Ar^+ + NO$ and $Ar^+ + N_2$

Shan Xi Tian*

Hefei National Laboratory for Physical Sciences at the Microscale, Department of Chemical Physics, University of Science and Technology of China, Hefei, 230026, China

Ion-molecule reactions are frequently observed in plasma, flame, atmosphere, and interstellar space. Although different physicochemical processes such as inelastic collision leading to the state excitations, fragmentation, and production of new chemical compounds can happen, the basics are only charge exchange or transfer and translational-to-internal energy transfer. These two fundamental features are strongly dependent on the quantum state properties of the colliding objects and the collision energy.

Here we report some new results by using our recently established ion velocity map imaging (VMI) apparatus for the low-energy (less than 20 eV) ion-molecule reaction dynamics study:

1. In the charge exchange reactions of $Ar^+ + NO \rightarrow Ar + NO^+$, a resonant charge transfer to form NO^+ ($a^3\Sigma^+$) plays a predominant role through whole collision energy range (2.09-3.71 eV) investigated here, while to the higher states $b^3\Pi$ and $w^3\Delta$ of NO^+ only at the lower collision energies. This abnormal translational-to-internal energy transfer trend is due to the easier formation of $(Ar\text{-}NO)^+$ in the slower collisions [1].
2. In the charge exchange reactions of $Ar^+ + N_2 \rightarrow Ar + N_2^+$, $X^2\Sigma_g^+$ and $B^2\Sigma_u^+$ states of N_2^+ can be accessed directly, while $A^2\Pi_u$ state is populated by the nonadiabatic couplings between X and A states and between A and B states. These two couplings are out of Franck-Condon region of the $N_2 \rightarrow N_2^+$ vertical transitions, and cannot be observed in the photoionizations. This work (see Fig. 1) is the first example about such nonadiabatic processes in the ion-molecule reaction [2].

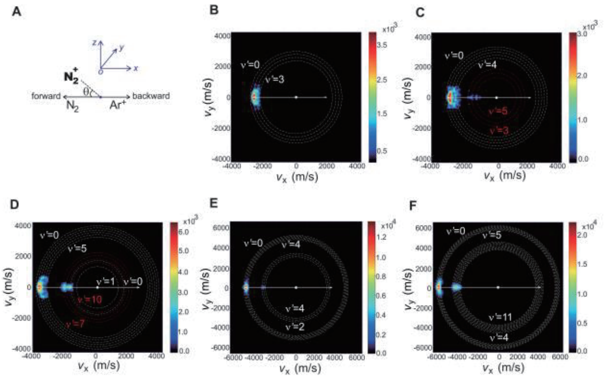

Fig. 1. (A) Experimental arrangement of the ion-molecule reactions of $Ar^+ + N_2 \rightarrow Ar + N_2^+$. Time-sliced images of N_2^+ ion velocity distributions at the relative collision energies of 1.98 eV (B), 2.47 eV (C), 3.73 eV (D), 6.37 eV(E), and 9.21 eV (F). Each image is obtained by rotating and weighting the measured three-dimensional velocity distribution of N_2^+ ions. Reactant velocities are indicated by white arrows (N_2 along the negative and Ar^+ along the positive x axis). Newton spheres plotted with broken white circles in the image correspond to the vibrational states v' of N_2^+ $X^2\Sigma_g^+$ (outer white circles), $A^2\Pi_u$ (inner red circles) and $B^2\Sigma_u^+$ (inner white circles).

The present study clarifies the previous long-standing arguments about above processes. The ion momentum images reported here are much clearer than those obtained in the other groups [3,4], which largely benefits from our unique design of a well-confined pulsed low-energy ion beam source [5].

References

[1] J. Hu, C.-X. Wu, Y. Ma, S. X. Tian, 2018 *J. Chem. Phys.* (submitted).
[2] J. Hu, *et al.*, (to be submitted).
[3] J. Mikosch, *et al.*, 2008 *Science* **319** 183.
[4] L. Pei, J. M. Farrar, 2012 *J. Chem. Phys.* **136** 204305.
[5] J. Hu, C.-X. Wu, S. X. Tian, 2018 *Rev. Sci. Instrum.* **89** 066104.

---

* E-mail: sxtian@ustc.edu.cn

Soft X-ray emissions from inner-shell excited Li-like ions in charge transfer collisions of meta-stable He-like ions with neutral gases

Hajime Tanuma[*, 1] **and Naoki Numadate**[* 2]

[*] Department of Physics, Tokyo Metropolitan University, Hachioji, Tokyo 192-0397, Japan

In Tokyo Metropolitan University, we have performed ion-beam collision experiments using a 14.25 GHz ECR (electron cyclotron resonance) ion source which produces a plasma of temperature about 10^6 K. Multiply charged ions produced with this ion source were extracted with an electric potential of 10–20 kV and the charge-state of the ions was selected by using a double-focusing dipole magnet.

The ion beam with a single charge state was introduced into a collision cell filled with a target gas, and photon emissions from the collision cell in an an EUV (extreme ultra-violet) region were observed with a compact grazing-incident spectrometer equipped with a gold-plated cylindrical mirror for light condensing and a variable-line-spacing (ca. 1200 lines/mm) grating. A CCD (charge coupled device) camera with a Peltier cooling system was installed in the spectrometer.

In this work, we have observed photon emissions in soft X-ray regions in collisions of helium-like C, N, and O ions with neutral gas targets. If the incident helium-like ions are in their ground state $1s^2\ {}^1S_0$, the photon emissions from lithium-like ions might be smaller than the ionization energies of $1s^22s$ ions, namely 64.49, 97.89, and 138.12 eV, respectively, because single-electron captures are the most dominant in collisions of multiply charge ions with neutral gases in low energy collisions, and the initial states of emissions might be $1s^2n\ell$. However, we observed emissions around 300, 400, and 600 eV in collisions of C^{4+}, N^{5+}, and O^{6+}, respectively.

Therefore, we consider that the emissions from $1s2sn\ell$ states produced in charge transfer collisions of helium-like ions in the meta-stable triplet states, $1s2s\ {}^3S_1$, were observed in our experiments. As it is well-known that the helium-like ion beam produced with an ECR ion source is a mixture of the ground state and the long-lived excited state and has few percents of the meta-stable state, the formation of $1s2sn\ell$ states might be possible. However, the most probable decay process of the inner-shell excited state is usually Auger electron emission, and the radiative emission is not strongly expectable.

We have looked for the previous similar studies in the literature, and found a series of experiments in Grenoble, France [1, 2, 3]. In these experiments, the results with He and H_2 target gases were reported. But, our new results show difference from the previous ones in the emission spectra. Furthermore, we measured spectra with other target gases, namely Ne, Ar, Kr, Xe, N_2, O_2, and CO_2, and observed strong target dependence in some cases.

Fig. 1 is shown a typical emission spectrum observed in collisions of C^{4+} with He at collision energy of 60 keV. These peaks correspond to the transitions from $1s2s({}^3S)3p\ {}^2P$, $1s2s({}^{1,3}S)2p\ {}^2P$, and $1s2s2p\ {}^4P$ states to the ground state of lithum-like C^{3+} ions ($1s^22s\ {}^2S$). The identification of transitions was performed with the theoretical calculations [4].

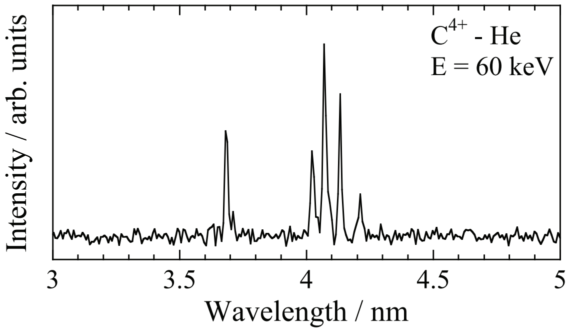

Fig. 1. EUV emission spectrum in collisions of C^{4+} with He at ion energy of 60 keV.

References

[1] M. G. Suraud *et al.*, 1988 *J. Phys. B* **21** 1219.

[2] L. Guillemot *et al.*, 1990 *J. Phys. B* **23** 3353.

[3] S. Bliman *et al.*, 1992 *J. Phys. B* **25** 2065.

[4] F. F. Goryaev *et al.*, 2017 *At. Data Nucl. Data Tables* **113** 117.

---

[1] E-mail: tanuma-hajime@tmu.ac.jp

[2] E-mail: numadate-naoki@ed.tmu.ac.jp

Triple-core hole states produced in the interaction of solid-state density plasmas with a relativistic femtosecond optical laser

Jiaolong Zeng, Cheng Gao, Yongjun Li, Pengfei Liu, and Xiaohui Fan

Department of Physics, College of Liberal Arts and Sciences, National University of Defense Technology, Changsha 410073, Hunan, P. R. China

Atoms with inner-shell vacancies such as single- and double-core hole (SCH/DCH) states have been produced and observed by different methods such as collisions with highly charged ions and electron beams [1], interaction with synchrotron radiation [2] and laser beams such as ultra-intense ultrafast x-ray free electron laser (XFEL) and intense optical lasers. These exotic atomic states contain rich information of the surrounding environment and can be helpful in many research fields such as chemical analysis, x-ray atomic laser and warm and hot dense matter.

Extremely exotic dense matter states can be produced in the interaction of a relativistic femtosecond optical laser with a solid density matter. Here we theoretically investigate triple-core hole (TCH) states produced by an intense polychromatic x-ray field formed by hot electrons in the interaction of a relativistic femtosecond optical laser with a thin silver foil. X-ray emission spectra of solid-state density silver plasmas show unambiguously the production of TCH states at an electron temperature of a few hundreds of eV and radiative temperature of 1-3 keV of the polychromatic x-ray field. Practical calculations show that the emissivity originating from the TCH states exceeds that from the single- and double-core hole states in Ne-like Ag^{37+} at electron temperature of ~500 eV and radiative temperature of ~1500 eV. For the neighbouring ionization stages of Ag^{36+} and Ag^{38+}, TCH emissivity is roughly equivalent or comparable to that from the single- and double-core hole states (see Fig. 1). Present work deepens insight into investigation of the properties of extremely exotic states, which is important in high energy density physics, astrophysics and laser physics.

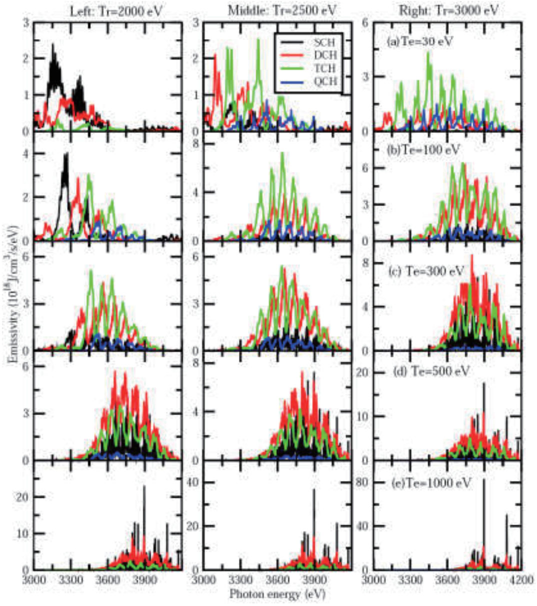

Fig. 1. Emissivity of single and multiple core hole states of the Ag plasmas at radiative temperature of Tr=2000 eV (left), 2500 eV (middle) and 3000 eV (right). The electron temperature is set to be 30 eV, 100 eV, 300 eV, 500 eV and 1000 eV, respectively, from top to bottom.

References

[1] J. P. Briand, S. Thuriez,, G. Giardino, G. Borsoni, M. Froment, M. Eddrief, & M. Sébenne, Observation of hollow atoms or ions above insulator and metal surfaces. Phys. Rev. Lett. **77**, 1452-1455 (1996).

[2] Y. Hikosaka, P. Lablanquie, F. Penent, T. Kaneyasu, E. Shigemasa, J.H.D. Eland, T. Aoto, and K. Ito, Double photoionization into double core-hole states in Xe. Phys. Rev. Lett. 98, 183002 (2007).

---

[1] E-mail: zlzeng@nudt.edu.cn

Statistical properties of atomic structures of r-process elements

Daiji Kato*,**,[1], **Gediminas Gaigalas**†, **Masaomi Tanaka**$,$$

*National Institute for Fusion Science, Toki, Gifu 509-5292,Japan
**Dept. of Advanced Energy Engineering Science, Kyushu University, Fukuoka 816-8580, Japan
†Institute of Theoretical Physics and Astronomy, Vilnius University, LT-10257 Vilnius, Lithuania
$Astronomical Institute, Tohoku University, Sendai, Miyagi 980-8578, Japan
$$National Astronomical Observatory of Japan, Osawa, Mitaka, Tokyo 181-8588, Japan

Gravitational waves by a binary neutron star merger have been detected on 2017 August 17 (GW170817 [1]) for the first time. Ejecta from the neutron star merger are expected to contain heavy elements created by the r-process, the rapid neutron-capture process that makes half of all elements heavier than iron [2]. Electromagnetic emission, so called as kilonova, powered by radioactive decays of the synthesized r-process nuclei in the ejecta has also been observed [3]. While properties of the emission are largely affected by opacities in the ejected material, available atomic data for r-process elements are still limited.

In this talk, we present new calculations of atomic structure for r-process elements: Se (Z = 34), Ru (Z = 44), Te (Z = 52), Ba (Z = 56), Nd (Z = 60), and Er (Z = 68) [4]. Due to extremely complicated energy level structure and huge number of transitions, applications of statistical analysis assuming stochasticity of the atomic structures are introduced.

For the atomic structure calculations, we use two different codes, HULLAC [5] and GRASP2K [6]. The HULLAC code, which employs a parametric potential method, is used to provide atomic data for many elements while the GRASP2K code, which enables more ab initio calculations based on the multiconfiguration Dirac-Hartree-Fock (MCDHF) method, is used to provide benchmark calculations for a few elements. Such benchmark calculations are important because systematic improvement of the accuracies is not always obtained with the HULLAC code especially when little data are available in the NIST Atomic Spectra Database (ASD; [7]). By using these two codes, we also study the influence of the accuracies of atomic calculations on the opacities.

Due to extremely complicated atomic structures and quasi continuum spectra, knowledge of its statistical properties is useful for analysis. Statistical weight distribution of each electronic configuration is well approximated by the skewed normal distribution [8]. The distribution is uniquely parametrized by a set of statistics, i.e. mean, standard deviation, and skewness. The atomic structures of the r-process elements calculated by HULLAC and GRASP2K are analyzed in terms of these statistics. Differences in statistical distributions of oscillator strengths calculated by the two codes are evaluated by Kolmogorov-Smirnov statistical test. We will also discuss perspectives on the statistical methods for atomic structures of heavy elements.

References

[1] B.P. Abbott et al.: Phys. Rev. Lett. 119 (2017) 161101.
[2] S. Wanajo et al.: ApJ 789 (2014) L39.
[3] Y. Utsumi et al.: Publ. Astron. Soc. Japan (2017) psx118, https://doi.org/10.1093/pasj/psx118.
[4] M. Tanaka, D. Kato, G. Gaigalas et al.: ApJ 852 (2018) 109.
[5] A. Bar-Shalom, M. Klapisch, J. Oreg, JQSRT, 71 (2001) 169.
[6] P. Jönsson, G. Gaigalas, J. Bieroń, C.F. Fischer, I.P. Grant, CoPhC, 184 (2013) 2197.
[7] A. Kramida, Y. Ralchenko, J. Reader, NIST ASD Team 2015, NIST Atomic Spectra Database (ver. 5.3) (Gaithersburg, MD: National Institute of Standards and Technology) http://physics.nist.gov/asd.
[8] R.D. Cowan, The theory of atomic structure and spectra, Univ. California Press, Berkeley,1981.

---

[1] E-mail: kato.daiji@nifs.ac.jp

Development of electron impact spectroscopy for directly observing the nuclear motions in molecular systems

Yuichi Tachibana [1], **Masakazu Yamazaki** [2], **Masahiko Takahashi** [3]

Institute of Multidisciplinary Research for Advanced Materials, Tohoku University, Sendai 980-8577, Japan

The importance of wave functions in quantum mechanics has been bringing many efforts to obtain more accurate wave functions both experimentally and theoretically. For instance, shapes of electron wave functions can now be experimentally observed by several methods such as electron momentum spectroscopy [1]. However, those for observing shapes of vibrational wave functions are still in infancy. Here we demonstrate that a new technique, called atomic momentum spectroscopy (AMS) [2], enables one to quantitatively measure momentum distributions of nuclei in a molecule or to observe molecular vibrational wave functions in momentum space.

AMS employs quasi-elastic electron backscattering at large momentum transfer $\boldsymbol{q}$. Within the framework of the impulse approximation, the scattering process is simply described by a billiard ball-type collision between the incident electron and a single nucleus in a molecule. Then, a recoil energy of the scattering nucleus with mass M is given by $E_{\mathrm{recoil}} = q^2/2M + \boldsymbol{q}\cdot\boldsymbol{p}/M$, where $\boldsymbol{p}$ is the momentum of the scattering nucleus before collision, and E_{recoil} can be measured by observing the energy loss of the incident electrons.

AMS experiments were conducted at an incident energy of 2.0 keV and at an energy resolution of c.a. 0.6 eV by using our multichannel spectrometer [3], which accepts quasi-elastically backscattered electrons from the target at a scattering angle of 135°±0.4° over an azimuthal angle ϕ range from -72.5° to 72.5° and from 107.5° to 252.5°.We have obtained an instrumental response function from experiments on heavy rare gas atoms, and subsequently employed it to generate theoretical AMS spectra to be compared with experiments on several diatomic molecules.

Figure 1 shows experimental AMS spectra of H_2 and N_2. Also included in this figure is associated theoretical AMS spectra (solid curves) generated by folding quantum-chemistry-predicted nuclear momentum distributions (chained curves) with the instrumental response function. It is evident that the experimental and associated theoretical spectra are in satisfactory agreement with each other, that is, nuclear motions due to molecular vibration can be directly probed by this technique.

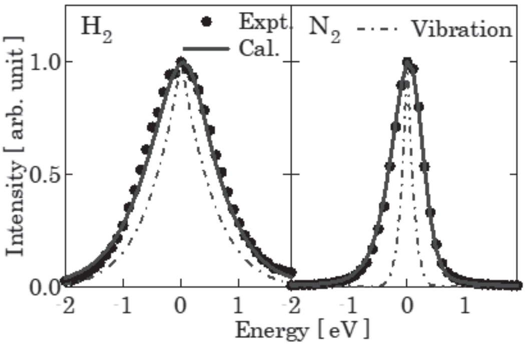

Fig. 1. Electron energy loss spectra of H_2 and N_2.

We believe the present work would be an important step towards development of time-resolved AMS that provides a completely new, momentum space approach to studying chemical reaction dynamics.

This work was partially supported by Hatano Foundation.

References

[1] M. Takahashi, 2009 *Bull. Chem. Soc. Jpn.* **82**, 751.
[2] M. Vos and M. Went, 2009 *J. Phys. B: At. Mol. Opt. Phys.* **42**, 065204.
[3] M. Yamazaki, M. Hosono, Y. Tang and M. Takahashi, 2017 *Rev. Sci. Instrum.* **88**, 063103.

---

[1] E-mail: yuuichi.tachibana.s7@dc.tohoku.ac.jp
[2] E-mail: masakazu@tohoku.ac.jp
[3] E-mail: masahiko@tohoku.ac.jp

Ab initio simulation of the energy loss experiment for alpha particles moving in discharged H plasmas

Yan-Ning Zhang[1, 2], Yong-Tao Zhao[1], Chun-Lei Liu[2], and Bin He[2*]

[1] Xi'an Jiaotong University, Xia'an, 710049, China

[2] Institute of Applied Physics and Computational Mathematics, Beijing 100088,P.R. China

The energy loss ΔE of ions moving in discharged H plasmas has been measured for more than 20 years [1-3]. The first relevant experiment [1] confirmed the theoretical stopping power predictions close to the expected maximum in fully ionized plasmas, which is much higher than that in neutral gas. Later similar results were found by Golubev *et al.* [2] with 3 MeV protons as the projectile. In recent years a series of such experiments were made in the Institute of Modern Physics in China [3] with the projectile energy E_p equal to 100keV/u. Two years ago Zhao reported their results of ΔE evolution for alpha particles in partially ionized H plasmas, where the effective charge state of the alpha particles Z_{eff} was found close to 1.75 according to Bethe equation in atomic units $-\frac{dE}{dx} = \frac{4\pi Z_{eff}^2}{v_p^2}\left\{ n_{be} Log \frac{2V_p^2}{I} + n_{fe} Log \frac{2V_p^2}{\omega_p} \right\}$.

Here v_p, n_{be}, n_{bf}, I and ω_p are the projectile velocity, bound and free electron density, mean ionization energy of H, and the plasma frequency, respectively. How to explain the experiment is the aim of the present work. In order to do this a lots of *ab initio* calculations have been made and the above equation is also revised since v_p (=2) is not much higher than Bohr velocity. Some details of our simulation are listed in the following.

First the fraction evolution for the possible states of the projectiles in the plasmas including He^{2+}, $He^+(1s)$, $He^+(2l)$, $He^+(2l)$, $He(1s^2)$ and $He(1s2l)$, are obtained according to the rate equations of the states [4]. In the simulation the main processes which have strong influences on the projectile states are considered, which include charge transfer, ionization and excitation by electron, proton and H(1s), radiation de-excitation, recombination, etc. Besides this all the relevant cross sections and transition rates are obtained by non-perturbative methods and FAC code. The data for n_{be} and n_{bf} evolution are determined by initial energy loss at gas and Ref. [5].

Next the respective stopping powers due to He^{2+}, He^+, and $He(1s^2)$ in H gas are found by classical trajectory Monte Carlo [6] with total stopping power and the fraction of the projectile states in good agreement with the recommended [7] and experimental data [8], respectively. The corresponding stopping powers in electron plasmas are obtained with the influence of bound electrons included. Based on these the evolution for ΔE is found and shown in Fig. 1, which indicates that our final results agree well with the experiments. The results will be bad if de-excitation is ignored or projectiles are in ground states. More details will be given in the meeting.

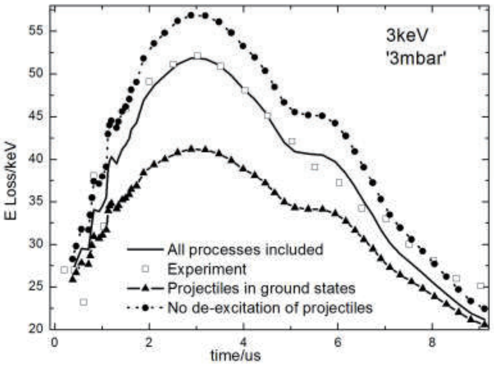

References

[1] J. Jacoby *et al.* 1995 Phys. Rev. Lett. 74, 1550.

[2] A. Golubev *et al.* 1998, Phys. Rev. E 57 3363.

[3] R. Cheng *et al.* 2018 *Laser & Particle Beams.* **36**

[4] T. Peter and J. Meyer-ter-Vehn 1998 Phys. Rev. A 43, 2015

[5] A.P. Kuznetsov, *et.al.* Plasma Phys. Rep. 39, 248 (2013)98

[6] R.E. Olson and A. Salop 1977, Phys. Rev. A 16, 531

[7] J.F. Ziegler 1977 ***Helium*** *Stopping powers and Ranges in All Elemental Matter*

[8] S.K. Allison 1958 *Rev. Mod. Phys.* **30,** 1137

---

[1] E-mail: Hebin-rc@163.com

[2] E-mail: Zhaoyongtao@xjtu.edu

Optical emission spectroscopy and collisional radiative modeling for Ar plasma

Duck-Hee Kwon*,[1], Kil-Byoung Chai*, and Min Park†

* Nuclear Data Center, † Fusion Engineering Center, Korea Atomic Energy Research Institute, Yuseong-gu, Daejeon
305-353, Korea

Optical plasma diagnostic methods such as optical absorption and emission, laser-induced fluorescence, Raman and Thomson scattering have been extensively used to measure electron/ion temperature and density, species concentrations in plasmas. Optical emission spectroscopy (OES) is comparatively simple, versatile, non-intrusive, and has been widely used in diagnostics for various plasmas such as magnetically confined fusion plasma, gas discharge low-temperature capacitively coupled plasma (CCP), and inductively coupled plasma (ICP). OES determines plasma parameters such as electron temperature and density by a combination with population kinetics modeling.

We have carried out OES and collisional-radiative modeling (CRM) taking into account all viable collisional and radiative processes of atoms and ions in plasma [1] for CCP and ICP systems. A sketch of the experiment setup is shown in Fig. 1.

In present CRM, populations (n_i) of the i levels are obtained by solving the stationary rate balance equations:

$$\sum_{j\neq i} n_e n_j \alpha_{ji}^{ex} + \sum_{j>i} \eta_{ji} A_{ji} = \sum_{j\neq i} n_e n_i \alpha_{ij}^{ex} + \sum_{j<i} \eta_{ij} A_{ij} + n_e n_i \alpha_i^{iz} + n_i \nu_i^{d},$$

where n_e is the volume averaged electron density, α_{ij}^{ex} is the electron impact excitation/deexcitation rate coefficient from ith level to jth level, α_i^{iz} is the electron impact ionization rate coefficient for ith level, A_{ij} and η_{ij} are transition probabilities (Einstein's A coefficient) and escape factor for optical transition, from ν_i^d is the quenching probability per unit time by diffusion to chamber walls.

Fig. 2 shows the CRM results for our measured spectra in the CCP. When T_e and n_e by the probe measurement is used in the CRM with the effective plasma length R_{eff} assumed as the chamber radius, the modeled spectra shows large discrepancy with the measured spectra shown in Fig. 2 (a) and (c). When reduced R_{eff} is used in the CRM, the agreement between the measured and the modeled spectra is improved as shown in Fig. 2 (a) and (d).

Some discrepancies for specific transition lines between modeling and measurement may come from the detailed atomic data underlying in the CRM and the sensitivity of line intensity to the atomic data has been investigated. Effect of electron energy probability function (EEPF) and radiation trapping on the CRM has been also discussed.

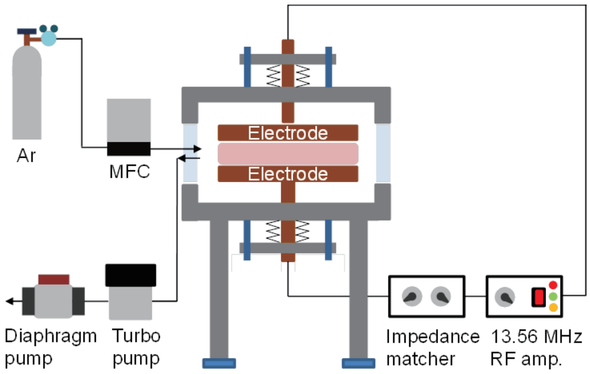

Fig. 1. Sketch of the experimental setup.

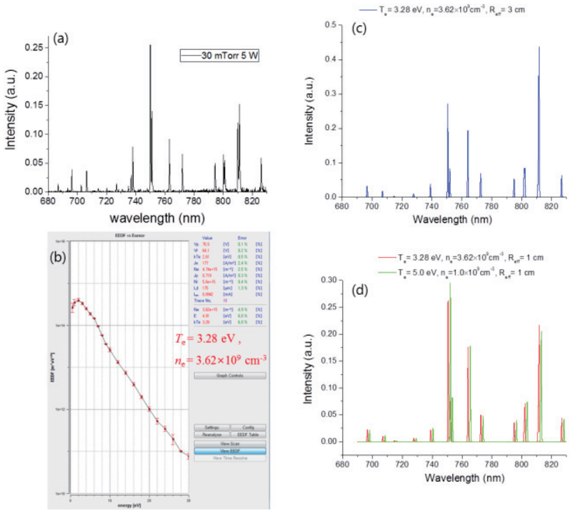

Fig. 2. (a) Measured spectra and (b) electron temperature and density from our CCP. (c) Our CRM spectra for T_e=3.28 eV and n_e=3.62×10^9 cm^{-3} determined from probe measurement for effective plasma length R_{eff} assumed as chamber radius R=3.0 cm. (d) Our CRM spectra for T_e=3.28 eV, n_e=3.62×10^9 cm^{-3} (red line) and T_e=5.0 eV, n_e=1.0×10^9 cm^{-3} (green line) with R_{eff}=1.0 cm.

References

[1] S. Iordanova, I. Koleva, 2007 *Spectrochimica Acta Part B* **62** 344.

---

[1] E-mail: hkwon@kaeri.re.kr

Estimation of photon emission coefficients in tungsten UTA transitions using LHD plasmas

Shigeru MORITA*,†,1, Yang LIU†,2, Izumi MURAKAMI*,†,3, Tetsutaro OISHI*,†,4
and Motoshi GOTO*,†,5

* National Institute for Fusion Science, Toki 509-5292, Gifu, Japan
† Department of Fusion Science, School of Physical Sciences, The Graduate University for Advanced Studies
(SOKENDAI), Toki 509-5292, Gifu, Japan

Tungsten pseudo-continuum spectra called unresolved transition array (UTA) emitted in 15-70Å have been quantitatively analyzed by observing the radial profile in neutral-beam heated plasmas of Large Helical Device (LHD). In our previous result [1], it has been found that the UTA line at wavelength intervals of 32.16-33.32, 30.69-31.71 and 29.47-30.47 Å is composed of only a single ionization stage of W^{24+}, W^{25+} and W^{26+}, respectively. Based on the previous result, the ion density of W^{24+}, W^{25+} and W^{26+} is evaluated by observing the radial profile of UTA lines at the specified wavelength intervals [2].

A photon emission coefficient (PEC) for the W^{24+}, W^{25+} and W^{26+} ions is necessary for the density evaluation. At first, the PEC is calculated using a collisional-radiative (CR) model which has been developed by Murakami [3]. In the CR model, principal quantum number up to n = 7 and 11753, 13772 and 7515 J-resolved fine-structure levels are taken into account for W^{24+}, W^{25+} and W^{26+} ions, respectively, and 19-27 electron configurations are considered for one ion. Effects of inner-shell excitation and configuration interaction are also considered in addition to general atomic processes. The photo emission coefficient at each wavelength interval then includes 100 thousands line emissions at each wavelength interval. The tungsten density profile of W^{24+}, W^{25+} and W^{26+} ions is thus obtained from the local emissivity profile and the photon emission coefficient in addition to the temperature and density profiles.

A total tungsten ion density, n_W, near $\rho = 0.7$ where the W^{24+} ion locates is also estimated from the W^{24+} ion density with the fractional abundance in ionization equilibrium calculated with ADAS code [4]. The value of n_W evaluated from the present CR model seems to be large, when it is compared with n_W estimated from the number of tungsten particles injected by the pellet. Discussions are made with the n_W evaluated from the photon emission coefficient in CL version of ADAS code.

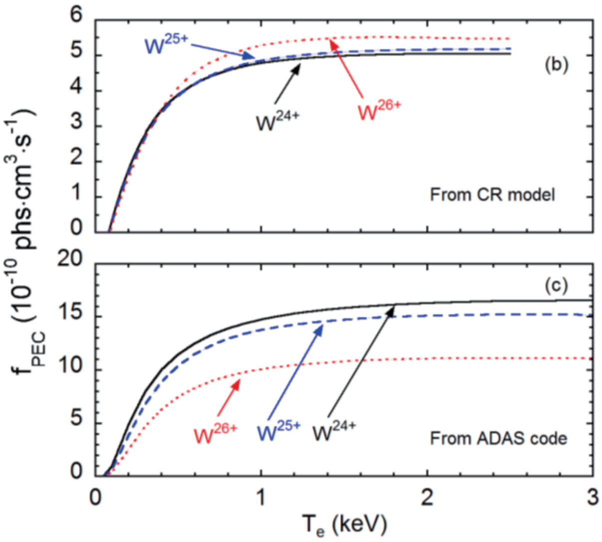

Fig. 1. Photo emission coefficients from (a) CR model [3] and ADAS (CL version) [4].

References

[1] Y. Liu, S. Morita, X.L. Huang, T. Oishi, M. Goto and H.M. Zhang, 2017 *J. Appl. Phys.* **122** 233301.
[2] Y. Liu, S. Morita, I. Murakami, T. Oishi, M. Goto and X.L. Huang, submitted to *Jpn. J. Appl. Phys.*
[3] I. Murakami, H.A. Sakaue, C. Suzuki, et al., 2015 *Nucl. Fusion* **55** 093016.
[4] H.P. Summers, The ADAS User Manual, version 2.6 http://www.adas.ac.uk (2004).

---

[1] E-mail: morita@nifs.ac.jp
[2] E-mail: liu.yang@nifs.ac.jp
[3] E-mail: murakami.izumi@nifs.ac.jp
[4] E-mail: oishi@nifs.ac.jp
[5] E-mail: goto@nifs.ac.jp

Experimental evaluation of fractional abundance data for $W^{23+} - W^{28+}$

Keisuke Fujii^{*,1}

*Department of Mechanical Engineering and Science, Graduate School of Engineering, Kyoto University,
Kyoto 615-8540, Japan

The tungsten (W) density in plasmas has been estimated from the line emission intensity from a certain charge state (q) ions and the fractional abundance for this charge state $\xi_q(T_e)$. Although $\xi_q(T_e)$ is an essential quantity to the tungsten density measurement in plasmas, its values reported by sevral groups have been significantly different from each other, as shown in Fig. 1.

In this work, we observed T_e dependence of near-ultraviolet emission line intensities for highly charged tungsten ions for several plasma experiments in Large Helical Device (LHD) [1]. From the spatially resolved emission intensity distribution measured with multi-line-of-sight spectrometer and with the Bayesian statistics technique, we quantitatively evaluated the fractional abundance profiles for $W^{23+}W^{28+}$.

Although the absolute values of the fractional abundance are still inaccessible in our method, relative profiles against T_e values were evaluated, as shown in the bottom row in Fig. 1. The T_e values at the profile peak for $q = 23$, 24, 25, 26, 27 and 28 states tungsten abundance were evaluated as 0.53, 0.58, 0.65, 0.78, 0.93, and 1.14 keV, respectively (indicated by the vertical arrows in Fig. 1). These results were ≈20% smaller than those reported by Pütterich et al [3], which are the theoretical calculations adjusted to match the quasi-continuum emission by $q = 24$-35 tungsten ions measured in the extreme ultraviolet region, and ≈60% larger than the pure theoretical calculation by Sasaki et al [2].

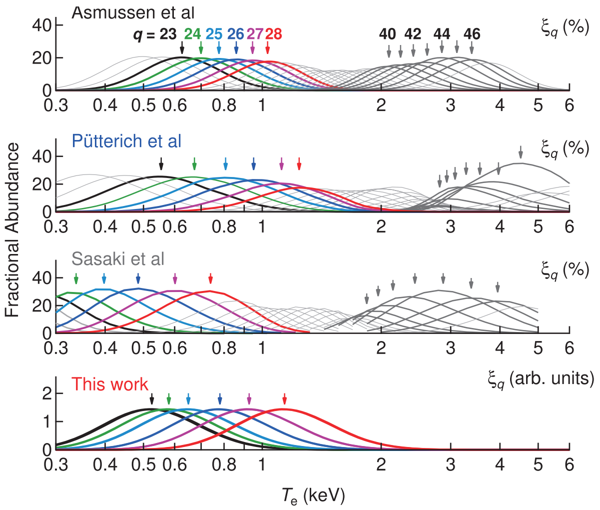

Fig. 1. Fractional abundance data xq for highly charged tungsten ions. The four panels from the top show the data sets proposed by Asmussen et al [4], Pütterich et al [3], Sasaki et al [2], and evaluated results in this work, respectively.

References

[1] K. Fujii, D. Kato et al., 2017. *J. Phys. B: At. Mol. Opt. Phys* **50**, 055004

[2] A. Sasaki and I. Murakami, 2013. *J. Phys. B: At. Mol. Opt. Phys* **46**, 175701

[3] T. Ptterich, R. Neu et al., 2008.*Plasma Phys. Control. Fusion* **50**, 085016

[4] K. Asmussen, K. Fournier, et al., 1998. *Nucl. Fusion* **38**, 967

---

[1] E-mail: fujii@me.kyoto-u.ac.jp

Estimating the emission spectra of W^{23+}- W^{30+} by the numerical decomposition of multiple spectra observed from LHD plasmas

Takehiko Esaka[*,1], **Izumi Murakami**[†,2], **Shigeru Morita**[†,3], **Hasuo Masahiro**[*,4], **Keisuke Fujii**[*,5]

[*] Graduate School of Engineering Kyoto University, Kyoto Nishikyo-ku, Kyoto, 615-8246, Japan
[†] National Institute for Fusion Science, Toki, Gifu 509-5292, Japan

1. Introduction

Tungsten (W) was decided to be used as a divertor material of ITER. To monitor W transport in high temperature plasmas, spectroscopic observation has been conducted. Figure 1 shows two W spectra y_m measured for LHD plasmas in different two conditions. m is an index along wavelength direction. Each spectrum is modeled as follows.

$$y_m = \sum_q n_q \phi_{q,m} + \varepsilon \qquad (1)$$

where n_q is the density of W^{q+}, $\phi_{q,m}$ is its emission spectrum and ε is the noise of the measurement. If the exact profiles $\phi_{q,m}$ are known, the evaluation of n_q is possible. Blue curves in Fig. 2 (a) show three results $\phi_{q,m}^{\mathrm{ref}}$ (q = 26, 27 and 28) from one atomic structure model [1, 2]. n_q has been estimated to optimize the following equation.

$$\mathrm{argmin}_{n_q} \sum_m D\left(y_m \middle| \sum_q n_q \phi_{q,m}^{\mathrm{ref}}\right) \qquad (2)$$

where $D(a|b)$ is a distance measure between a and b. The squared distance $(a-b)^2$ has been frequently used. Blue curves in Fig. 2 (b) shows the reconstructed result $\sum_q n_q \phi_{q,m}^{\mathrm{ref}}$ with the best n_q, where W^{q+} (q = 23-30) is assumed to be included in plasmas. As shown in the figure, it is still difficult to reconstruct the experimental data exact enough.

In this work, we evaluate both $\phi_{q,m}$ and n_q by decomposing the observed spectra based on its profile variation, considering theoretically predicted spectra.

2. Method

We use multiple spectra $y_{\mathrm{m}}^{(k)}$ observed with various experimental conditions, where k = (1, 2, …, 4580) is the experimental data index. We estimate both $\phi_{q,m}$ and $n_q^{(k)}$ from the following optimization problem

$$\mathrm{argmin}_{n_q^{(k)},\phi_{q,m}} \left\{ \sum_k D\left(y_m^{(k)} \middle| \sum_q n_q^{(k)} \phi_{q,m}\right) + \alpha \sum_{q,m} D\left(\phi_{q,m}^{\mathrm{ref}} \middle| \phi_{q,m}\right) \right\} \qquad (3)$$

The first term represents the goodness of reconstruction, while the second term represents the closeness between $\phi_{q,m}$ to be estimated and $\phi_{q,m}^{\mathrm{ref}}$. α controls the relative importance of the second term. We use 250 for α. In this work, we use Kullback-Leibler divergence for D. Since Eq. 3 has the same form to the non-negative matrix factorization (NMF) problem, it is optimized efficiently [3].

3. Results and Discussion

Figure 2 (a) shows three of the decomposed results of $\phi_{q,m}$ (q = 26, 27 and 28, red curves). Although the overall shapes of $\phi_{q,m}$ and $\phi_{q,m}^{\mathrm{ref}}$ are similar to each other, their detailed shapes are different. In Fig. 2 (b), our reconstructed result $\sum_q n_q^{(k)} \phi_{q,m}$ is also shown (red curve). It is suggested that the use of $\phi_{q,m}$ instead of $\phi_{q,m}^{\mathrm{ref}}$ increases the accuracy of the density estimation.

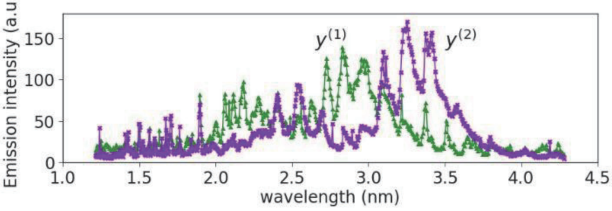

Fig. 1 Two examples of the observed W spectra.

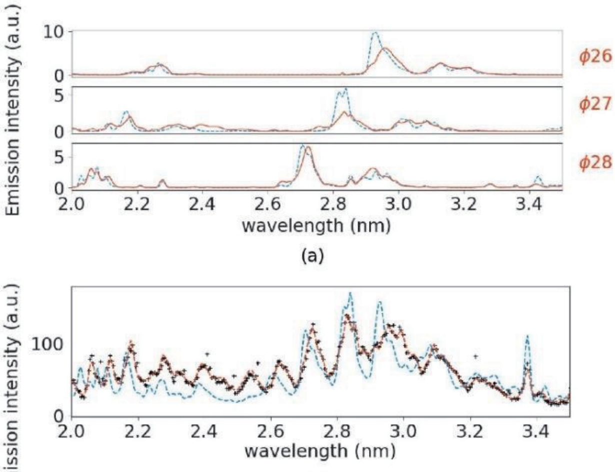

(a)

(b)

Fig. 2 (a) Three examples of $\phi_{q,m}^{\mathrm{ref}}$ (blue curve) and decomposed $\phi_{q,m}$ (red curve) for q = 26, 27, and 28. (b) One example of the observed spectrum ${y_m}^{(k)}$ (markers), reconstruction from the atomic structure calculation $\phi_{q,m}^{\mathrm{ref}}$ (blue curve) and that from our decomposition (red curve).

References

[1] I. Murakami, et al. , 2015, *Nucl. Fusion*, vol. 55, 093016.

[2] A. Bar-Shalom, et al. ,2001, *J. Quant. Spectrosc. Radiat. Transfer*, vol. 71, pp. 169-188.

[3] D. Lee and H. Seung, 2000, *Neural Information Processing Systems (NIPS)*, pp. 556-562.

---

[1] E-mail: esaka.takehiko.86a@st.kyoto-u.ac.jp

[2] E-mail: mizumi@nifs.ac.jp

[3] E-mail: morita@nifs.ac.jp

[4] E-mail: hasuo.masahiro.6u@kues.kyoto-u.ac.jp

[5] E-mail: fujii@me.kyoto-u.ac.jp

Estimation of density profiles of W^{43+}-W^{45+} in EAST H-mode plasma

Ling. Zhang[*,1], **Shigeru Morita**[†‡,2], **Zhenwei Wu**[*,3], **Zong Xu**[§,4], **Xiuda Yang**[*], **Qing Zang**[*], **Haiqing Liu**[*], **Xianzu Gong**[*], **Liqun Hu**[*]

[*] Key laboratory of Atomic and Molecular Physics & Functional Materials of Gansu Province, College of Physics and Electronic Engineering, Northwest Normal University, Lanzhou, 730070, China

[*]Institute of Plasma Physics Chinese Academy of Sciences, Hefei 230026, Anhui, China
[†]National Institute for Fusion Science, Toki 509-5292, Gifu, Japan
[‡]Department of Fusion Science, Graduate University for Advanced Studies, Toki 509-5292, Gifu, Japan
[§]Advanced Energy Research Center, Shenzhen University, Shenzhen 518060, China

EAST tokamak has been equipped with upper tungsten divertor since 2014 to improve the heat exhaust capability and to examine the ITER-like divertor configuration [1]. In order to study the tungsten behavior in EAST discharges, tungsten spectra has been measured in EUV wavelength range using fast-time-response EUV spectrometers working in wavelength ranges of 20-500Å [2] and 10-130 Å with time resolution of 5ms. Recently, a space-resolved EUV spectrometer working at 30-500Å has been developed to measure radial profiles of the tungsten line emission in long-pulse H-mode discharges with high heating power.

Radial profiles of tungsten emissions from 4p-4s and 4p-4p transitions in W^{42+} – W^{45+} ions are successfully obtained at 45-70 Å and 120-140 Å in high-temperature discharges ($T_e \geq 2.5$keV), e.g. W^{43+} at 61.334Å, W^{44+} at 60.93Å, W^{45+} at 62.336 Å, W^{42+} at 129.41Å, W^{43+} at 126.29 Å and W^{45+} at 126.998Å. The radial density profiles of W^{43+} – W^{45+} are therefore attempted with measured T_e and n_e profiles and photon emissivity coefficient (PEC) from ADAS database when the radial emission profile is converted into flux surface function with Abel inversion technique.

Fig.1. shows radial profiles of chord-integrated line intensity of W^{45+} at 62.336Å, W^{44+} at 60.93Å and W^{43+} at 61.334 Å in steady-state H-mode plasma with T_{e0}=3.3keV (Shot #67682). Fig.2. shows the calculated radial profiles of W^{45+} and W^{44+} ion density in steady-state H-mode phase in Shot #67682.

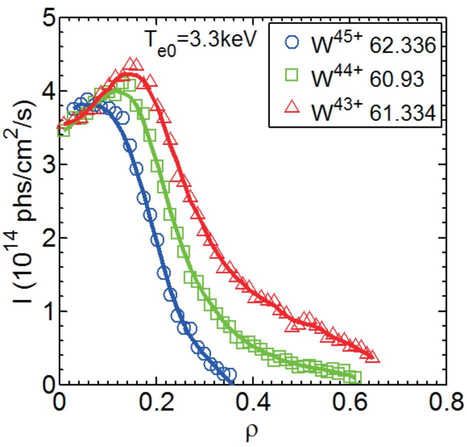

Fig. 1. Vertical profile of W line intensity.

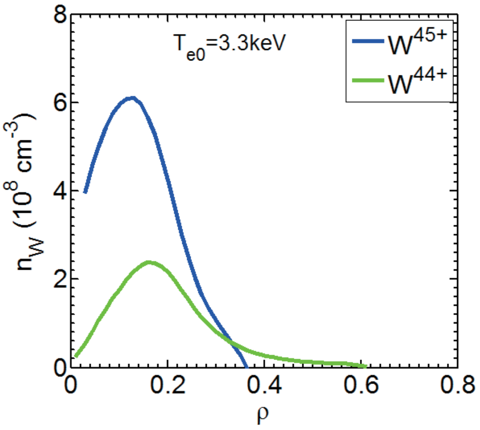

Fig. 2. Radial profile of W ion density.

References

[1] D. Yao, G. Luo, S. Du et al., 2015 *Fusion Eng. Des.* **98-99** 1692.
[2] L. Zhang, S. Morita, Z. Xu et al., 2015 *Rev. Sci. Instrum.* **86** 123509.

---

[1] E-mail: zhangling@ipp.ac.cn [3] E-mail: zwwu@ipp.ac.cn

[2] E-mail: morita@nifs.ac.jp [4] E-mail: xuzong@ipp.ac.cn

Radiation Hydrodynamic Characteristics of Highly Charged Ions in Laser-Produced Plasmas

Maogen Su*[,1], Qi Min*, Shiquan Cao*, Duixiong Sun*, G. O'Sullivan†, Chenzhong Dong*

[*] Key laboratory of Atomic and Molecular Physics & Functional Materials of Gansu Province, College of Physics and Electronic Engineering, Northwest Normal University, Lanzhou, 730070, China
†School of Physics, University College Dublin, Belfield, Dublin 4, Ireland

A laser-produced plasma (LPP) ablated by nanosecond laser pulse is neither homogeneous nor static in the expanding and cooling process in vacuum, where electron densities can vary from 10^{17} to 10^{22} cm^{-3} and electron temperature from 1 eV to 100 eV. In such plasmas, there are many competing atomic processes which depend on electron temperature and electron density. Electrons, ions and photons take part in these processes and interact with each other. The experimental measurements and theoretical analysis of LPP spectra can reveal abundant information on the plasmas, such as electron temperature, electron/ion density, particle and energy transport, and the evolution of these parameters. In recent decades the LPP has gained universal acceptance as a standard laboratory ion source[1] and pulsed short wavelength light source[2].

Due to the limitation of measurement accuracy, spectral structure and plasma model, there are few reports on the radiation and dynamics of highly-charged ions in the EUV region of mid- and high-Z elements, the dynamics behaviors in the plasma is not yet clear. Our group built a high precision spatio-temporally resolved spectral measuring device, developed a set of real-time measurement control and spectral analysis software. And based on the radiative-hydrodynamics model, we developed a dynamic simulation code to investigate the complicated spectral features of highly-charged ions from LPP. The evolution diagnosis of electron density, plasma temperature, ion velocity, radiation loss and other parameters in the process of laser plasma expansion are obtained, and the transient evolution images of the plasma are reconstructed. The results are helpful for a detailed understanding of the spectral features and hydrodynamics evolution for highly charged ions of the mid- and high-Z elements. More importantly, it will be of use to groups working on ion and light source development.

This work was supported by National Key Research and Development Program of China (2017YFA0402300); National Natural Science Foundation of China (NSFC) (11274254, U1332206, 11364037, 11064012, 11564037).

References

[1] N. J. Peacock, and R. S. Pease, 1969 *J. Phys. D: Appl. Phys.* 2 1705.
[2] D. T. Attwood, Soft X-Rays and Extreme Ultraviolet Radiation (Cambridge University Press, Cambridge, 2000)

---

[1] E-mail: **nwnu_sumg@163.com**

Ultrafast nonequilibrium electron dynamics in a solid-density aluminium interacting with an ultra-intense ultrafast x-ray pulse

Cheng Gao*,[1], Jiaolong Zeng*, and Jianmin Yuan*#

* Department of Physics, College of Liberal Arts and Sciences, National University of Defense Technology, Changsha 410073, Hunan, P. R. China
# Graduate School, China Academy of Engineering Physics, Building 9, ZPark II, No. 10 Xiebeiwang Road, Beijing 100193, P. R. China

The investigation of light-matter interaction is expanding from long wavelength into short wavelength with applications of x-ray free electron laser (XFEL)[1-2]. Followed by the pioneering experiment of an ultra-intense XFEL pulse interacting with a neon atom gas [3], many researches are performed to investigate the interaction of XFEL and complex systems [4-5].

Ultrafast nonequilibrium dynamics of free electrons in a solid-density aluminium produced by an ultra-intense ultrafast x-ray pulse is investigated by solving Fokker-Planck equation. Electron energy distribution function (EEDF) contains two parts: a lower energy part at nearly equilibrium and a higher energy part at evident nonequilibrium. The former part accounts for the most population of the total electron number. X-ray transmission and bound-bound emissivity show little difference between the results with EEDF obtained by solving Fokker-Planck equation and by Maxwellian distribution assumption. Yet the bremsstrahlung emissivity shows great difference.

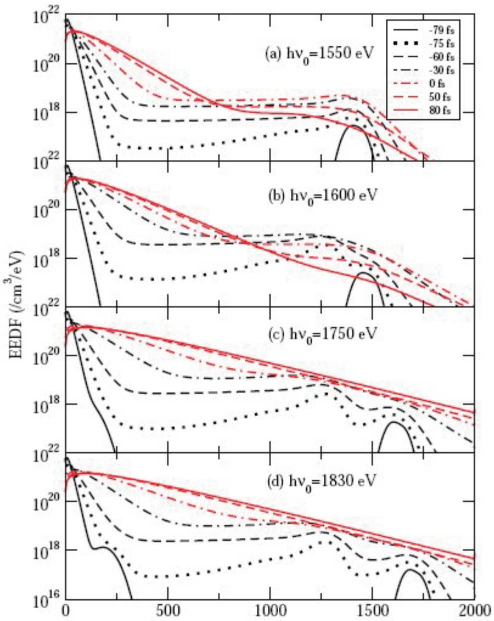

Fig. 1. Time evolution of EEDF at the center of the laser spot on the front of aluminium sample (x=0 um). X-ray photon energy is (a) 1550, (b) 1600, (c) 1750 and (d) 1830 eV, respectively.

The x-ray pulse has a peak intensity of $1.24 \times 10^{17} W/cm^2$ with HWHM duration of 40 fs and a bandwidth of 0.5%. The x-ray beam has a circle spot with radial of 1.3 um.

References

[1] P. Emma et al., *Nat. Photon.* 4, 641 (2010).
[2] C. Bostedt et al., *Rev. Mod. Phys*. 88, 015007 (2016).
[3] L. Young et al., *Nature (London)* 466, 56 (2010).
[4] S.M. Vinko et al, *Nature (London)* 482, 59 (2012).
[5] H. Yoneda et al., *Nat. Commun.* 5, 5080 (2014).

---

[1] E-mail: gaocheng@nudt.edu.cn

Temporal space localization of electrons ejected from continuum atomic processes in hot dense plasma

Pengfei Liu[1], Cheng Gao[1], Yong Hou[1], Jiaolong Zeng*[1], and Jianmin Yuan†[1,2]

[1]Department of Physics, National University of Defense Technology, Changsha Hunan 410073, China
[2]Graduate school of China Academy of engineering Physics, Beijing 100193, China

Continuum atomic processes initiated by photons and electrons occurring in a plasma are fundamental in plasma physics, playing a key role in the determination of ionization balance, equation of state, and opacity. Here we propose the notion of a temporal space localization of electrons produced during the ionization of atoms immersed in a hot dense plasma, which can significantly modify the fundamental properties of ionization processes. A theoretical formalism is developed to study the wavefunctions of the continuum electrons that takes into consideration the quantum de-coherence caused by coupling with the plasma environment. The method is applied to the photoionization of Fe^{16+} embedded in hot dense plasmas. We find that the cross section is considerably enhanced compared with the predictions of the existing free-atom model, and thereby partly explains the big difference between the measured opacity of Fe plasma [1] and the existing standard models for short wavelengths.

Striking changes induced by localization may further be seen in the total photoionization cross sections of the ground and excited levels of Fe^{16+} (Fig.1). In panel (a), both contributions from the direct ionization of 2p and 2s electrons and indirect ionization from the resonant processes have been included to give a more complete picture. The cross section of the free ion features a series of resonances $2s \rightarrow np$ ($n \geq 6$) superimposed on the continuum background. The cross section of free ion is in satisfactory agreement with a recent large-scale R-matrix calculation[2]. For the embedded ion, however, resonances of higher np disappear for the principal quantum number n larger than 10, 7, and 6 at densities of 4.0×10^{21}, 4.0×10^{22}, and $2.0 \times 10^{23} cm^{-3}$,respectively. However, additional resonances of $2s \rightarrow 5p$ and $2s \rightarrow 4p$ successively show up at the density of 4.0×10^{22} and $2.0 \times 10^{23} cm^{-3}$. This shows that the bound states belonging to the configurations of $1s^2 2s2p^6 5p$ and $1s^2 2s2p^6 4p$ in the free ion Fe^{16+} have become autoionized states because of plasma screening.

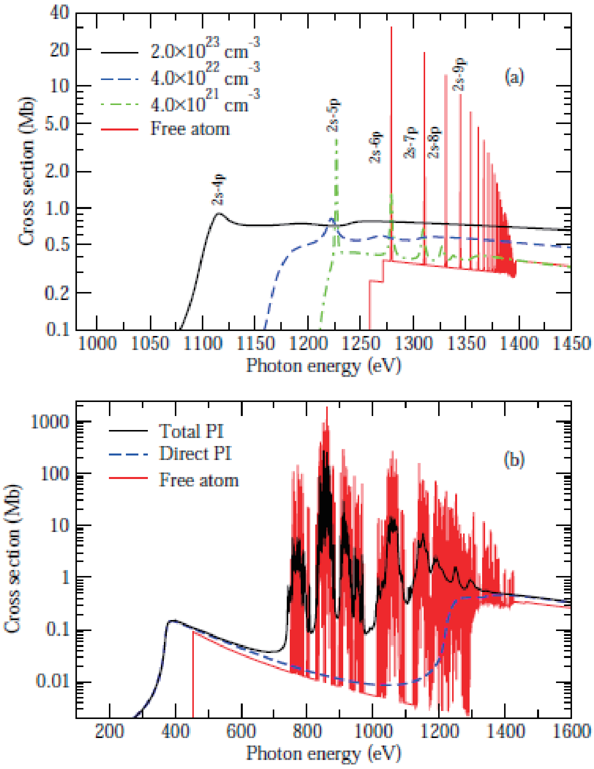

Fig. 1. Total photoionization cross sections.(a) For the ground level $1s^2 2s^2 2p^6\ ^1S$ of Fe^{16+} including both direct ionization of 2p and 2s electrons and indirect resonant processes at 180.0 eV.(b) For the excited state $1s^2 2s^2 2p^5 3d\ ^1P^o$ of Fe^{16+}, which is assumed to be embedded in an iron plasma at an electron density of $3.0 \times 10^{22} cm^{-3}$ and a temperature of 180.0 eV.

References

[1]J. E. Bailey *et al.*, A higher-than-predicted measurement of iron opacity at solar interior temperatures. Nature (London) **517**, 56 (2015).

[2]S. N. Nahar and A. K. Pradhan, Large enhancement in high-energy photoionization of Fe XVII and missing continuum plasma opacity. Phys. Rev.Lett.**116**,235003(2016)

---

* E-mail: jlzeng@nudt.edu.cn
† E-mail: jmyuan@gscaep.ac.cn

A consideration on the accuracy of GRASP calculations

Fumihiro Koike,

Faculty of Science and Technology, Sophia University

Accurate and reliable calculations of atomic structures and transition properties are indispensable for understandings of fusion and other plasmas. As for the theoretical methods based on the variational principle, a number of atomic codes such as FAC, HULLAC, Cowans code, GRASP family of codes, and others are available for this purpose. Among them the GRASP family of codes provides us with a non-empirical relativistic method and is believed that the code gives most reliable result if treated properly. In recent years, an elaborate large scale calculation has become feasible using the pararrell processing technology and has become a large amount of numerical values that are usable for plasma analysis.

However, we must note that the theoretical method that is employed by GRASP family of codes has its intrinsic difficulties. The method is based on a variational principle with a positive indefinite Hamiltonian, we cannot avoid the possibility of variational collapse in the procedure of self-consistent iteration. And, furthermore, in case of excited state calculations, similar collapse may occur. The orbital wavefunctions are restricted to the L2 normalizable functions, which cause the introduction of correlation functions in the MCDF calculations. We must be careful to treat the correlation functions if we want to calculate the atomic excited states.

We want to discuss these difficulties by showing several examples that may cause some errors in MCDF calculations.

Email: koikef@sophia.ac.jp

Visible spectra of multiply charged heavy ions obtained with a comapct electron beam ion trap

NAKAMURA Nobuyuki[*, 1],

[*] Inst. for Laser Science, The Univ. of Electro-Communications, Tokyo 182-8585, Japan

Visible transitions in multiply charged heavy ions are of interest for many applications. For example, transitions in multiply charged W ions are in strong demand for the stable operation of the large scale fusion reactor ITER under construction. Since W is the material of the plasma facing wall of ITER, sputtered W ions are considered to be the main impurity in the ITER plasma [1]. Thus it is important to diagnose and control the W influx and charge evolution through spectroscopic diagnostics of W ions. Although all the wavelength ranges, including short wavelength ranges such as EUV and x-rays, are important for the diagnostics, transitions in the visible range are especially important due to the advantage that a variety of common optical components, such as mirrors, lenses, and fiber optics, can be applied.

As another example, optical transitions in multiply charged ions have been proposed for a new type of an optical clock that has a significantly enhanced sensitivity to the fine-structure constant variation due to the strong relativistic effects [2]. The variation of fundamental constants arises in many theories beyond the Standard Model of particle physics and is hinted by the astrophysical observations. Recently, it was suggested that dark matter may lead to oscillations of fundamental constants or transient effects that may be potentially detectable with such clocks [3]. It is also an advantage that the wavefunction of the electron tightly bound in a highly charged ion is less sensitive to the perturbation such as external fields.

In this contribution, we present visible spectra of multiply charged ions relevant to such applications obtained with a compact electron beam ion trap, called CoBIT [4]. CoBIT consists of an electron gun, a drift tube (DT), an electron collector, and a high-critical-temperature superconducting magnet. The DT is composed of three successive cylindrical electrodes that act as an ion trap by applying a positive trapping potential at both ends with respect to the middle electrode. The electron beam emitted from the electron gun is accelerated towards the DT while it is compressed by the axial magnetic field produced by the magnet surrounding the DT. The space charge potential of the compressed high-density electron beam acts as a radial trap in combination with the axial magnetic field. Multiply charged ions are produced through the successive ionization of the trapped ions. A commercial Czerny-Turner type of visible spectrometer is used for observing Visible emission from the trapped ions. The charge state of the ion assigned to the observed lines can be determined experimentally by studying the electron energy dependence of the line intensity. Recent results for tungsten [5] and lanthanide ions [6] and comparisons with theoretical calculations are presented.

References

[1] C. H. Skinner, 2008 *Can. J. Phys.* **86** 285.

[2] J. C. Berengut, V. A. Dzuba, and V. V. Flambaum, 2010 *Phys. Rev. Lett.* **105** 120801.

[3] A. Derevianko and M. Pospelov, 2014 *Nature Phys.* **10** 933.

[4] N. Nakamura, H. Kikuchi, H. A. Sakaue, T. Watanabe, 2008 *Rev. Sci. Instrum.* **79** 063104.

[5] M. Mita, H. A. Sakaue, D. Kato, I. Murakami, N. Nakamura, 2017 *Atoms* **5** 13.

[6] S. Murata, T. Nakajima, M. S. Safronova, U. I. Safronova, N. Nakamura, 2017 *Phys. Rev. A* **96** 062506.

---

[1] E-mail: n_nakamu@ils.uec.ac.jp

Experimental studies on the atomic processes related ICF plasmas at Shanghai-EBIT

Gang Xiong*, †, [1], Zhimin Hu*, [2], Ke Yao†, Jun Xiao†, Yang Yang†, Bo Qing*, Chengwu Huang*, Jiyan Zhang*, Yamin Zou†, Jiamin Yang*

* Laser Fusion Research Center, China Academy of Engineering Physics, Mianyang 621900, China
† Shanghai EBIT Laboratory, Institute of Modern Physics, Fudan University, and the Key Laboratory of Applied Ion Beam Physics, Chinese Ministry of Education, Shanghai 200433, China

Atomic process is crucial for laboratory plasma physics (Inertial confinement fusion (ICF), Tokomak, Z-pinch, etc.) and astrophysics. Accurate understanding of the atomic processes is important to validate the theoretical models and promote the accuracy of the plasma diagnostics. In recent years, we resumed experimental measurements at the updated Shanghai-EBIT facility focusing on the important atomic processes related to ICF plasmas. The measurements include the open-*L* shell dielectronic recombination of argon ions, the open-*M* shell electron impact excitation and dielectronic recombination of xenon ions. In this talk, we are going to report the details of these measurements and present the preliminary results of theoretical analysis.

References

[1] G. Xiong, J. M. Yang, J. Y. Zhang et al., 2016 *The Astrophysical Journal* **816**, 36.
[2] G. Xiong, J. Y. Zhang, Z. M. Hu et al., 2013 *Phys. Rev. A*, **88**, 42704
[3] Z. M. Hu, X. Y. Han, Y. M. Li et al., 2012 *Phys. Rev. Lett.* **108**, 73002

---

[1] E-mail: gangxiong@caep.cn

[2] E-mail: Zhimin.Hu@yahoo.com

State-Selective Quantum Interference Studied in the Photo-Recombination of Ar^{17+}

Kun Ma[*, 1], **Lu-You Xie**[†],**Xiao-Bin Ding**[†],**Chen-Zhong Dong**[†], **Hai-Jiang Lv**[*], **Feng-Jian Jiang**[*],**and Zheng Jiao**[*]

[*] School of Information Engineering, Huangshan University, Huangshan 245041, China
[†] College of Physics and Electronic Engineering, Northwest Normal University, Lanzhou 730070, China

Photo-recombination (PR) is a important atomic process in many high temperature plasmas. It not only helps to probe quantum electrodynamics in the strong fields of the ions from the energy positions and shapes of the observed resonance structure, but also reveals the relativistic corrections to the electron-electron interaction from the intensities of the PR cross section. Apart from its fundamental importance, PR process has practical implications in many high temperature plasmas, PR generates characteristic x-ray lines observed in many high temperature plasmas, such as solar flares, tokamaks] and inertial confinement fusion plasmas, accurate PR cross sections are essential for plasma diagnostics and for modeling of astrophysical and laboratory plasmas. Recently experimental measurements and theoretical calculation of PR cross sections for few-electron highly charged ions have been performed.

In the present work, the total and partial cross sections of the state-selective photo-recombination from the ground state $1s$ ($^1S_0$) of H-like Ar^{17+} ion to the $1s^2$ ($^1S_0$), $1s2s$ ($^1S_0$,$^3S_1$) and $1s2p$ ($^3P_{0,1,2}$,$^1P_1$) states of He-like Ar^{16+} ion were calculated in detail by using the Dirac atomic R-matrxi code based on a fully relativistic R-matrix method. The KLL photo-recombination resonance group are determined and identified according to the calculated transition energies and probabilities with multi-configuration Dirac Fock method (MCDF). In the calculations, the quantum interference of direct recombination and resonant recombination process are well considered. The results indicate that interference effects strongly influence the intensity and shape of the photo-recombination cross sections, especially for the $2s2p$ ($^1P_1$) and $2p^2$ ($^1D_2$) resonant region. The KLL dielectron recombination cross sections of H-like Ar^{17+} ion also calculated with MCDF method, results compare with the present photo-recombination cross section and the experimental dielectron recombination (DR) cross section, good agreement is found between available experimental DR cross section and the present DR calculate results with FWHM=19eV. Meanwhile, it is found photo-recombination results are different with DR which derived from interference between DR and PC process.

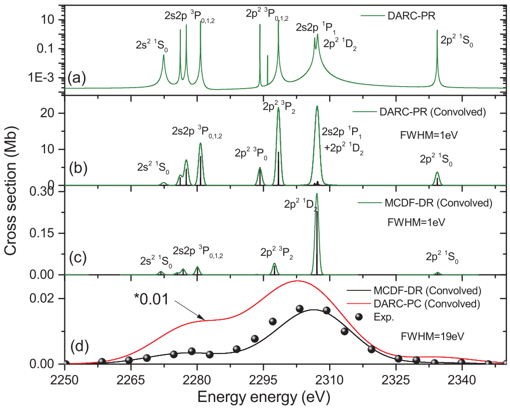

Fig. 1. (a) The total PC cross section of Ar^{18+} ion calculated by R-matrix approach; (b) Convoluted the data of (a) with FWHM =1 eV (c) Convoluted the DR cross section of Ar^{18+} ion calculated by M-CDF approach with FWHM =1 eV; (d) Convoluted the data of (a) with FWHM =19 eV and compare to the experimental results[1].

This work was supported by the Natural Science Foundation of Anhui Province (Grant No. 1808085QA22), by the Key Project for Young Talents in College of Anhui Province (Grant No. gxyqZD2016301), by Natural Science Foundation of the Higher Education Institutions of Anhui Province (Grant No. KJHS2015B01), and by the Natural Science Research Project of Huangshan University (Grant No. 2016xskq003).

References

[1] D. R. DeWitt, D. Schneider, M. W. Clark, M. H. Chen, D. Church, 1991 *Rhy. Rev. A* 44 7185.

---

[1] E-mail: makun0602@163.com

Effect of Breit interaction on linear polarization of radiation lines following electron-impact excitation of Ca^{14+}, Xe^{49+}, and W^{69+}

C. Ren, Z. W. Wu[1], J. Jiang, L. Y. Xie, D. H. Zhang, and C. Z. Dong[2]

Key laboratory of Atomic and Molecular Physics & Functional Materials of Gansu Province, College of Physics and Electronic Engineering, Northwest Normal University, Lanzhou, 730070, China

Recently, Jörg *et al.* [1] measured the linear polarization of x-rays produced by dielectronic recombination of highly charged Xe^{49+} ions, they found that the Breit interaction have no effects on it. In order to test the effects of the Breit interaction on the same x-ray lines transitions but formed from the electron-impact excitation (EIE) process, the linear polarization of the 2p→1s and 2p→2s emission lines of highly charged Ca^{15+}, Xe^{49+} and W^{69+} ions are investigated by using a fully relativistic distorted-wave program REIE06 [2]. In the present work, we found that the Breit interaction makes the emission lines corresponding to the 2p→2s transition depolarized, while it makes the ones corresponding to the 2p→1s transition more polarized. The higher atomic number is, the more evident this characteristics become. These characteristics are different from the results obtained by Jörg *et al* [1]. Admittedly, Such a difference is caused by different population mechanisms of the excited states, as well discussed in Ref. [3].

Figure 1 shows the degree of linear polarization of the emission line 2p→1s of highly charged boronlike Ca^{15+}, Xe^{49+}, and W^{69+} ions. N+N denotes that both the target wave functions and impact matrix elements are calculated without the Breit interaction included; B+N denotes the former are calculated with an inclusion of the Breit interaction while the latter without the Breit interaction included; B+B denotes both of them are calculated with the Breit interaction included. As seen clearly from the Fig.1, the effect of the Breit interaction on the wavefunctions of target ions hardly influences the degrees of linear polarization at all of the situations. That is, the contribution of the Breit interaction to the degrees of linear polarization comes dominantly from the effect of the Breit interaction on the EIE matrix elements.

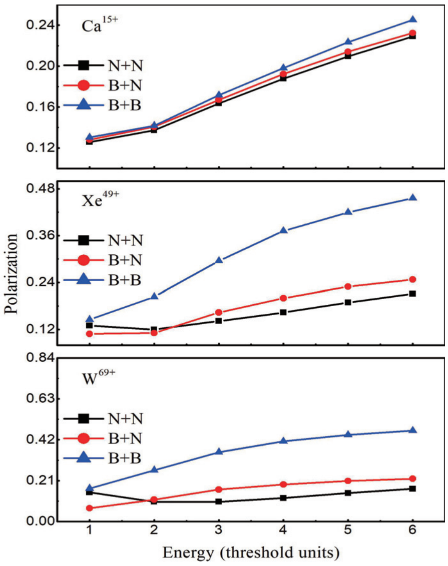

Fig. 1. The degree of linear polarization of the transition line 2p→1s for highly charged boronlike Ca^{15+}, Xe^{49+}, and W^{69+} ions.

Acknowledgment

This work has been supported by the National Key Research and Development Program of China (2017YFA0402300). Z. W. Wu acknowledges the support of the Scientic Research Program of the HigherEducation Institutions of Gansu Province, China (Grant No. 2018A-002).

References

[1] H. Jörg *et. al.* 2015 *Phys. Rev. A* **91** 042705.
[2] J. Jiang *et. al.* 2008 *Phys. Rev. A* **78** 022709.
[3] Z. W. Wu *et. al.* 2012 *Phys. Rev. A* **86** 022712.

---

[1] E-mail: zhongwen.wu@nwnu.edu.cn

[2] E-mail: dongcz@nwnu.edu.cn

The investigation of the anomalous asymptotic behavior of electron elastic scattering of helium

Ya-Wei Liu[1], **Lin-Fan Zhu**[2]

Hefei National Laboratory for Physical Sciences at Microscale and Department of Modern Physics, University of Science and Technology of China, Hefei, Anhui 230026, People's Republic of China
Synergetic Innovation Center of Quantum Information and Quantum Physics, University of Science and Technology of China, Hefei, Anhui 230026, People's Republic of China

For the inelastic electron scattering of atoms and molecules, a consensus has been reached that the first Born approximation (FBA) is easily approached with decreasing the momentum transfer at the same impact electron energy or increasing the impact electron energies at the same momentum transfer. This consensus can also be applied to the elastic electron scattering except that for helium, where the measured elastic differential cross sections deviate the FBA more severely with decreasing the squared momentum transfer at the same impact energy. Since the anomalous phenomenon is found at 40 years ago, it has not been explained explicitly.

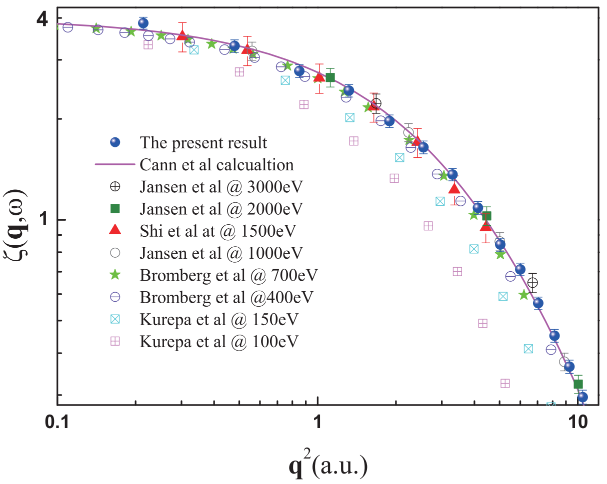

Fig. 1. The ESFFs $\zeta(\mathbf{q})$ of helium.

In the present work, the pure electronic structure of helium is determined directly for the first time by the high-resolution inelastic X-ray scattering at the Taiwan Beamline BL12XU of SPring-8 with an incident photon energy of about 10 keV and an energy resolution of about 70 meV. The present elastic squared form factors (ESFFs) $\zeta(\mathbf{q})$ of helium are shown in Fig. 1 along with the previous electron-scattering results [1-4] and the theoretical calculation [5].

By comparison, it is found that the discrepancies still exist for the electron elastic DCSs, even at the impact energy of 1500 eV. Because the scattering amplitude between the incident electron and the nuclei almost offsets the first Born scattering amplitude between the incident electrons and the target electrons, the DCSs of the electron scattering are almost from the contributions beyond the FBA, and the contributions are enlarged to a large extent in inverse proportion to the fourth power of the momentum transfer. This disagreements between the Born DCS and the DCS of the electron scattering can judge sensitively the validity condition of the FBA, especially in the small momentum transfer. The ESFF is only from the scattering of the target electrons in the high-resolution X-ray scattering, so it strictly test the wavefunctions in the inner region, nearby nucleus in the position space.

References

[1] J.P. Bromberg, 1974 *J. Chem. Phys.* **61** 963.

[2] R.H.J. Jansen, F.J. de Heer et. al., 1976 *J. Phys. B: At. Mol. Opt. Phys.* **9** 185.

[3] Q.C. Shi, R.F. Feng et. al., 1997 *J. Phys. B: At. Mol. Opt. Phys.* **30** 5479.

[4] M.V. Kurepa, and L. Vuskovic, 1975 *J. Phys. B: At. Mol. Opt. Phys.* **8** 2067.

[5] N.M. Cann and A.J. Thakkar, 2002 *J. Electron. Relat. Phenom.* **123** 143.

---

[1] E-mail: liuyawei@ustc.edu.cn

[2] E-mail: lfzhu@ustc.edu.cn

DR and TR rate coefficients of Be-like Ca

S. X. Wang[*], **X. Xu**[*], **Z. K. Huang**[†], **W. Q. Wen**[†], **H. B. Wang**[†], **S. Mahmood**[†], **N. Khan**[†], **L. J. Dou**[†], **S. P. Preval**[‡], **N. R. Badnell**[⋆], **S. Schippers**[♯], **X. Ma**[†],[1] **and L. F. Zhu**[*][2]

[*] Department of Modern Physics, University of Science and Technology of China, Heifei, 230026, P. R. China
[†] Institute of Modern Physics, Chinese Academy of Sciences, 730000, Lanzhou, P. R. China
[‡] Department of Physics and Astronomy, University of Leicester, University Road, Leicester, LE1 7RH, UK
[⋆] Department of Physics, University of Strathclyde, Glasgow G4 0NG, UK
[♯] I. Physikalisches Institut, Justus-Liebig-Universität Gießen, 35392 Giessen, Germany

Plasma is considering to be the most abundant form of the visible matter in the universe. Thus, accurate electron-ion recombination rate coefficients are crucial for astrophysicists to interpret the observed X-ray spectrum originating from various types of cosmic objects by plasma modeling. Storage ring equipped with an electron cooler is proved to be an ideal platforms for electron-ion recombination experiments.

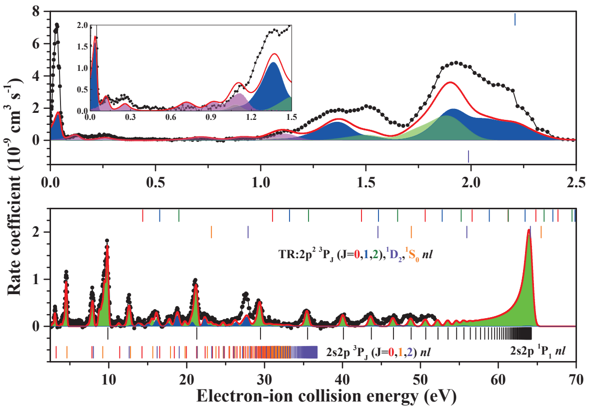

Fig. 1. Present experimental rate coefficients (filled-connected circles) and the calculated DR and TR rate coefficients (green shaded and blue shaded curve). The pink shaded curve denotes the rate coefficients for the 5% parent ions at the meta-stable level.

Calcium is one of the most abundant element in the solar system as well as in the universe. Here we present the measured electron-ion recombination rate coefficients of Be-like Ca at the CSRm at the Institute of Modern Physics by means of merged-beam technique as well as the theoretical calculation with AUTOSTRUCTURE code (see Fig. 1). The experiment was carried out subsequently to the successful electron-ion recombination experiments with Li- and Be-like Ar at the CSRm [1, 2]. The measurement covers the energy range of 0-51.88 eV including the dielectronic recombination (DR) and trielectronic recombination (TR) resonances associated with the core excitations of $2s^2\ ^1S_0 \rightarrow 2s2p\ ^3P_{0,1,2},^1P_1$ and $2p^2\ ^3P_{0,1,2},^1D_2,^1S_0$. Fractions of 5% ions at the $2s2p\ ^3P_0$ meta-stable level and 95% ions at the ground-level were considered in the calculation.

For the application in plasma modeling, plasma recombination rate coefficients for Be-like Ca were derived from the measured electron-ion recombination rate coefficients and compared with the calculated results (see Fig. 2). An agreement of better than 25% is achieved between the experiment and the theoretical calculation at the collisionally ionized temperature range.

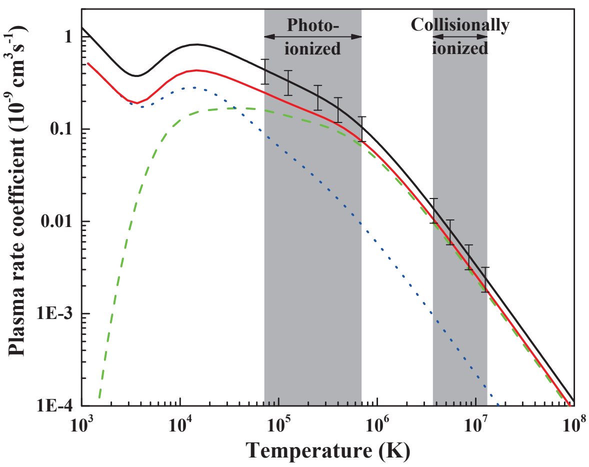

Fig. 2. The derived plasma rate coefficients from the experimental result (black line) and the AUTOSTRUCTURE calculation (red line). The green dashed and blue dotted line denote the calculated DR and TR rate coefficients, respectively. The error bars denote a 30% of experimental uncertainty.

References

[1] Z. K. Huang, W. Q. Wen, H. B. Wang et. al., 2015 *Physica Scripta* **T166** 014023

[2] Z. K. Huang, W. Q. Wen, X. Xu et. al., 2018 *Astrophys. J. Suppl. Ser.* **235** :2.

---

[1] E-mail: x.ma@impcas.ac.cn

[2] E-mail: lfzhu@ustc.edu.cn

Statistical Analysis of Hydrogen Recycling in the Peripheral Region of LHD

Takuya Osugi*,[1], **Masahiro Hasuo***,[2], **Keisuke Fujii***,[3]

[*] Graduate School of Engineering, Kyoto University, Kyoto Nishikyo-ku, Kyoto 615-8246, Japan

1. Introduction

In magnetic confined fusion plasmas, it is one of important studies to control particle recycling at the plasma facing components for the improvement of core plasma properties. For this purpose, it is necessary to understand the behavior of the peripheral plasma. Although simulation technique by EMC3-EIRENE code [1] has been developed, it is still difficult to quantify relationship between measured data because of high computational cost and many inaccessible plasma parameters in real experiments.

In this study, we fit a statistical model to experimental data of Large Helical Device (LHD), and quantified the relationship among multiple measurement data. We discussed hydrogen recycling near the divertor plate based on the result.

2. Statistical Modeling

Let $\mathit{\Gamma}_\mathrm{i}$ be the ion particle outflux from plasma to the divertor plate and $\mathit{\Gamma}_\mathrm{H}$ be the neutral atom influx to the plasma. If most of neutral atoms are generated by the recombination on the divertor plate, $\mathit{\Gamma}_\mathrm{H}$ is expected to be proportional to $\mathit{\Gamma}_\mathrm{i}$. We approximate this relation by the following form,

$$\delta\mathit{\Gamma}_\mathrm{H} = \delta\mathit{\Gamma}_\mathrm{i} + \varepsilon \tag{1}$$

where $\delta\mathit{\Gamma}_\mathrm{H}$ and $\delta\mathit{\Gamma}_\mathrm{i}$ are temporal changes in $\mathit{\Gamma}_\mathrm{H}$ and $\mathit{\Gamma}_\mathrm{i}$ during small time interval δt, respectively, while ε approximates the remaining cause of the atom generation, e.g. thermal desorption of atoms from the plate. We further approximate $\delta\mathit{\Gamma}_\mathrm{i}$ and ε follow independent Gaussian distribution,

$$\delta\mathit{\Gamma}_\mathrm{i} \sim \mathcal{N}\left(0, \sigma_\mathrm{i}^2\right) \tag{2}$$

$$\varepsilon \sim \mathcal{N}\left(0, \sigma_\varepsilon^2\right) \tag{3}$$

where σ_i^2 and σ_ε^2 are variance of $\delta\mathit{\Gamma}_\mathrm{i}$ and ε, respectively. With this assumption, $\delta\mathit{\Gamma}_\mathrm{H}$ and $\delta\mathit{\Gamma}_\mathrm{i}$ jointly follow a multivariate Gaussian distribution,

$$p\left(\begin{bmatrix}\delta\mathit{\Gamma}_\mathrm{i}\\ \delta\mathit{\Gamma}_\mathrm{H}\end{bmatrix}\right) = \mathcal{N}\left(\begin{bmatrix}0\\0\end{bmatrix}, \begin{bmatrix}\sigma_\mathrm{i}^2 & \sigma_\mathrm{i}^2\\ \sigma_\mathrm{i}^2 & \sigma_\mathrm{i}^2+\sigma_\varepsilon^2\end{bmatrix}\right) \tag{4}$$

The correlation coefficient r between $\delta\mathit{\Gamma}_\mathrm{H}$ and $\delta\mathit{\Gamma}_\mathrm{i}$ is

$$r = \sqrt{\frac{\sigma_\mathrm{i}^2}{\sigma_\mathrm{i}^2+\sigma_\varepsilon^2}} \tag{5}$$

In this work, we used measurement data of the ion saturation current i_is on the divertor plate and the Balmer-α emission intensity I_H for LHD plasmas. The sampling frequency for both measurements is 100 Hz. We assume i_is and I_H are proportional to $\mathit{\Gamma}_\mathrm{i}$ and $\mathit{\Gamma}_\mathrm{H}$, respectively, and estimated $\delta\mathit{\Gamma}_\mathrm{i}$ and $\delta\mathit{\Gamma}_\mathrm{H}$ from the AC components (with the frequency larger than 15 Hz) of measured signals.

3. Discussion

Figure 1(a) shows temporal evolution of i_is and I_H measured for the plasma. Fig. 1(b) and (c) show relations between the AC components of i_is and I_H measured at $t = 3.85 \sim 4.15$s and $t = 4.75 \sim 5.05$s, respectively. The value of the correlation coefficient r in Fig. 1(b) is larger than that in Fig. 1(c).

This difference suggests the different generation paths of the neutral hydrogen between these two timings. At the former timing, since σ_ε^2 in Eq. (5) is smaller than σ_i^2, $\delta\mathit{\Gamma}_\mathrm{i}$ in Eq. (1) becomes dominant compared with ε. It indicates that neutral atoms are mainly generated from the direct recombination of ions on the divertor plate. On the other hand, σ_ε^2 is larger than σ_i^2 in the latter case, suggesting neutral atoms are dominantly generated by another effect which has little correlation with $\mathit{\Gamma}_\mathrm{i}$.

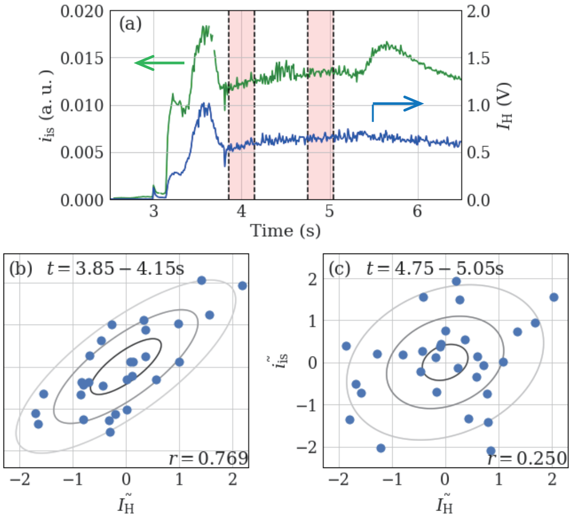

Fig. 1. (a) Measurement data of i_is (green line) and I_H (blue line) in shot number 137141. (b) and (c) are scatter diagrams of the AC components of i_is and I_H. Each variable is normalized to mean 0 and standard deviation 1.

References

[1] Y. Feng et .al, *Contrib. Plasma Phys* **44**, 57 (2004)

---

[1] E-mail: osugi.takuya.85u@st.kyoto-u.ac.jp

[2] E-mail: hasuo@kues.kyoto-u.ac.jp

[3] E-mail: fujii@me.kyoto-u.ac.jp

Three-body fragmentation dynamics of CF_4^{2+} induced by 1 keV electron collision

Lei Chen*, Zhenjie Shen*, Enliang Wang†, Xi Zhao*, Xu Shan*, Xiangjun Chen*[1]

* Hefei National Laboratory of Physical Sciences at the Microscale and Department of Modern Physics, University of Science and Technology of China, Hefei, 230026, China.
† Max Plank Institute for Nuclear Physics, 69117 Heidelberg, Germany.

Investigation on dissociative ionization of molecules is of intensive interest in physics, chemistry as well as biology. One of the major challenges in this area is to comprehend the molecular bond cleavage selectivity. The past few decades have witnessed tremendous progresses in the development of coincidence momentum imaging techniques [1, 2], which makes it feasible to reveal multi-body fragmentation dynamics for small molecules.

The CF_4 molecule, in its ground states, has a tetrahedral structure with high symmetry. It is an important gas in plasma processing and also a potent greenhouse gas. Although CF_4 has been extensively studied by plenty of experimental methods, reports on the breakup mechanics are still scarce. In this work, the three-body fragmentation dynamics of CF_4^{2+} is studied. The precursor ions, CF_4^{2+}, are created by 1000 eV electron collision and the two fragment ions are detected in coincidence by a momentum imaging system [3]. It is worthwhile to mention that the fragment channels of CF_4^{q+} ($q \geq 3$) have not been observed in present experiment.

According to the principle of momentum conservation, the momentum of the neutral fragment F is equal but opposite to the momentum summation of F^+ and CF_2^+. As a result, the kinetic energy of F can be deduced. By analyzing the Dalitz plot together with corresponding Newton diagram, two concerted fragmentation processes and one sequential fragmentation channel are identified:

$$CF_4^{2+} \longrightarrow F^+ + CF_2^+ + F, \qquad (1)$$

$$CF_4^{2+} \longrightarrow F + CF_3^+ \longrightarrow F^+ + CF_2^+ + F. \qquad (2)$$

In Fig. 1(a), Dalitz plot of three-body dissociation of CF_4^{2+} is demonstrated, which is not a typical “X” structure. The most intense area labeled by region I in Fig. 1(a) indicates the existence of a bending fragmentation channel (channel (1)). The Newton diagram for this channel is shown in Fig. 1(b), where the relative momentum vector of F^+ is fixed on the x axis while those of F and CF_2^+ are plotted in the lower and upper half-plane, relative to F^+. The correlation angle between the momentum vector of F^+ and CF_2^+ is about 163°, and that of F^+ and F is around 100°. This can be explained by the bending of CF_4 dication in a concerted dissociation process. On the left side of Dalitz plot, a less intense area labeled by region II, can be observed. From the related Newton diagram shown in Fig. 1(c), which exhibits a circular structure, a sequential fragmentation channel (channel (2)) can be clearly identified. The bottom area labeled by region III in the Dalitz plot corresponds to the Newton diagram in Fig. 1(d), which suggests CF_2^+-F bond and CF_2^+-F^+ bond break up simultaneously (channel (1)), but the geometries of the precursor CF_4^{2+} ions here are quite different with those in Fig. 1(b).

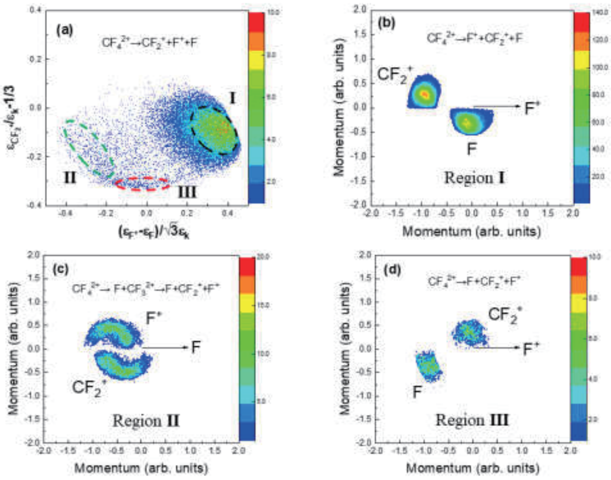

Fig. 1. (a) Dalitz plot of CF_4^{2+} dissociation into $F^+ + CF_2^+ + F$; (b) Newton diagram of bending concerted fragmentation; (c) Newton diagram of sequential fragmentation; (d) Newton diagram of simultaneous fragmentation.

References

[1] R. Dörner, et al. 2000 *Phys. Rep.* 330, 95.
[2] J. Ullrich, et al. 2003 *Rep. Prog. Phys.* 66, 1463.
[3] E.L. Wang, et al. 2013 *Rev. Sci. Instrum.* 84. 123110.

---

[1] E-mail: xjun@ustc.edu.cn

Delayed dissociation of metastable N_2O^{2+} induced by 56 keV/u Ne^{8+} ion collision

Xi Zhao*, Xu Shan*,[1], Xiaolong Zhu†, Wentian Feng†, Lei Chen*, Zhenjie Shen*, Enliang Wang*, Dalong Guo†, Yong Gao†, Ruitian Zhang†, Shuncheng Yan†, Shenyue Xu†, Bang Hai†, Hanbing Wang†, Zhongkui Huang†, Xinwen Ma†, Xiangjun Chen*

* Hefei National Laboratory for Physical Sciences at the Microscale and Department of Modern Physics, University of Science and Technology of China, Hefei, 230026, China
†Institute of Modern Physics, Chinese Academy of Science, Lanzhou, 730000, China

Dissociative ionizations of molecules induced by ion, electron and photon collision are of considerable interests to physics and chemistry as well as biology. In recent decades, the development of multiple coincidence methods based on time- and position-sensitive detection made it feasible to study the fragmentation dynamics of charged molecules.

In this article, we studied the ionization and fragmentation of N_2O in 56 keV/u Ne^{8+} collision. According to the ion-ion time of flight (TOF) correlation spectrum, as shown in Fig.1, two kinds of N_2O^{2+} dissociation channels were clearly identified. In addition, a long tail which extends from the NO^++N^+ coincidence trace was also observed. This structure might come from the delayed dissociation of metastable N_2O^{2+} during its motion along the axis of TOF system. Such phenomenon has also been observed in the study of N_2O under impact of fast electrons [1] and vacuum ultraviolet photons [2], but none of them obtained the kinetic energy released (KER) distributions of this channel to identify the metastable states of N_2O^{2+}. Here, we report a way to obtain the KER distributions of this channel and the life time of the metastable state. When the dissociation direction of N_2O^{2+} is perpendicular to the TOF axis, the distance between the positions that two ionic products hit the detector will be farthest. We can catch these events and determine their momentum vectors because their momenta along the TOF axis are zero. So it is easy for us to get the kinetic energy information of the products from these events.

We find that two peaks of the KER distributions are assigned at about 8.3 and 9.7 eV. Such values give a fairly good match with the calculated results of Taylor at al. [3], confirming that the metastable N_2O^{2+} is formed in $1^3\Pi$ and $2^3\Pi$ states. And we also estimated the metastable lifetime to be about 560±20 ns, which well agrees with the study of Field an Eland [4].

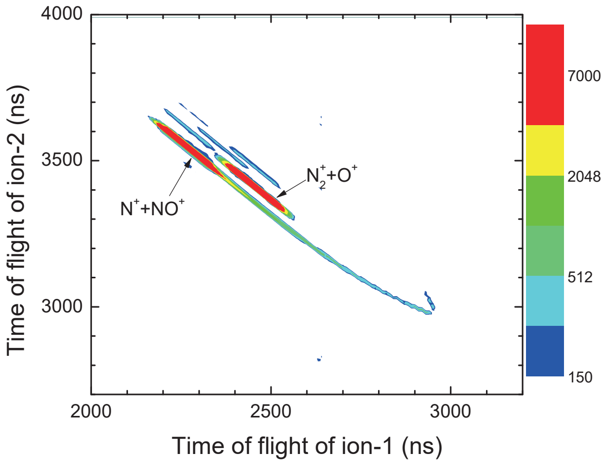

Fig.1. The ion-ion TOF correlation spectrum of the ionic fragments of N_2O^{2+} dissociation.

References

[1] A. Khan and D. Misra, 2016 *J. Phys. B* 49 055201

[2] M. Alagia, P. Candori, S. Falcinelli, M. Lavollée, F. Pirani, R. Richter, S. Stranges and F. Vecchiocattivi, 2006 *Chem. Phys. Lett.* 432 398

[3] Taylor S, Eland J H D and Hochlaf M 2006 *J. Chem. Phys.* 124 204319

[4] Field T A and Eland J H 1993 *Chem. Phys. Lett.* 211 436-42

---

[1] Email: xshan@ustc.edu.cn

The study of interference effects in NF_3 by electron momentum spectroscopy

Zhaohui Liu, Yaguo Tang, Shanshan Niu, Xu Shan, Xiangjun Chen[1]

Hefei National Laboratory for Physical Sciences at the Microscale and Department of Modern Physics, University of Science and Technology of China, Hefei, Anhui 230026, China

Electron momentum spectroscopy (EMS) has developed into a unique technique for investigating the electron structure of atoms and molecules, which can directly measure the orbital electron binding energy and electron density distribution in momentum space. According to the Dirac-Fourier transform, molecular orbital wave function in position space can be transformed into that in momentum space, and the electron momentum distribution can then be modulated by an oscillation function which is closely related to the molecular configuration. This oscillation structure of electron momentum distributions is called bond oscillation, which is the result of interference effect. Recently, the study of interference effects has become one of hot topics in EMS[1-4]. Through the interference pattern observed by EMS experiments, the particular bond lengths of CF_4 and CO_2 were derived with sub-angstrom precision[4].

In this work, the interference effect of NF_3 molecule has been studied by our high sensitivity electronic momentum spectrometer. Some orbitals like $1a_2$, 4e and 3e of NF_3 are mainly composed by F2p lone pairs, and the interference effect can be clearly observed through the ratio of those orbitals. With different interatomic distance of F-F and N-F, the theoretical momentum profile ratios (solid lines) compared with the experimental ones are shown in the figure (a) and (b). In order to have a precision view of bond distances, the χ^2 values have been introduced which is defined as the sum of squared differences between experimental and theoretical momentum profile ratios. An obvious minimum circle is shown in figure (c), and the bond lengths can then be derive in the present work to be R_{FF}=3.95a.u. and R_{NF}=2.54a.u., which is consistent with the value reported by electron diffraction[5].

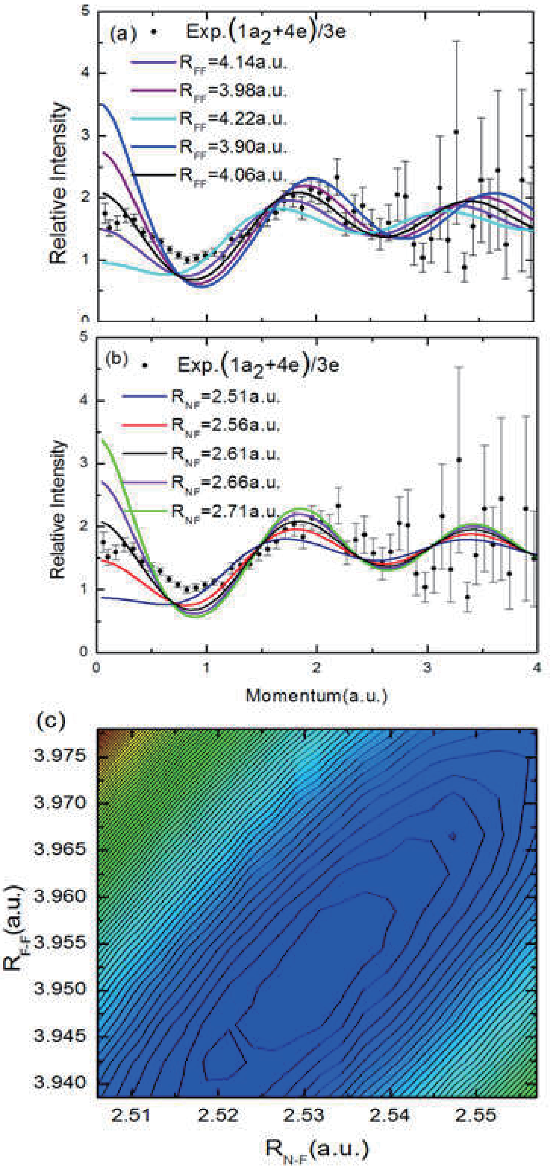

Figure (a) the ratio of experiment momentum profiles of $1a_2$+4e and 3e as well as the theoretical ones with different interatomic distance of F-F. Figure (b) the same as figure (a), but for different interatomic distance of N-F. Figure (c) is the χ^2 values.

References

[1] N. Watanabe, *et al*, *Phys. Rev. Lett.* 2015, 108, 173201
[2] Z. Zhang, *et al, Phys. Rev. Lett.* 2014,**112**, 023204
[3] M. Yamazaki, *et al, Phys. Rev. A* 2014, **90**, 052711
[4] E. L. Wang, *et al*, *Sci. Rep.* 2016, 6, 39351
[5] P. W. Allen, L. E. Sutton, *Acta Cryst.* 1950, 3, 46

---

[1] Email: xjun@ustc.edu.cn

Resonance contribution to electron-impact excitation rate coefficients of helium-like S^{14+} ions

C. Ren, Z. W. Wu[1], J. Jiang[2], and C. Z. Dong[3]

Key laboratory of Atomic and Molecular Physics & Functional Materials of Gansu Province, College of Physics and Electronic Engineering, Northwest Normal University, Lanzhou, 730070, China

Electron-impact excitation of positive ions is an important atomic process in high-temperature plasmas, it can proceed through direct excitation (DE) channels or indirect channels involving autoionizing resonances that are termed as resonance excitation (RE) [1, 2]. Due to its abundance in most of astrophysical plasmas, the structure and collision dynamics of sulfur have been widely studied in the last years. The parametric studies on the atomic process of sulfur and its ions are not only beneficial to plasma diagnosis, but also can provide effective data support for astrophysical and laboratory plasma modeling.

In the present work, electron-impact excitation rate coefficients of S^{14+} ions have been studied by using a relativistic flexible atomic code (FAC) that can account systematically for configuration interactions. Moreover, we also considered the resonance excitation contributions to the rate coefficients.

In table1,we list the excitation energies (in units of KeV) for the 1s excitations to the 2*s*, 2*p*, and 3*s* subshells of S^{14+} ions at the collision electron energies 2.4~3.0 KeV.

Table 1. Excitation energies (in units of KeV) of S^{14+} ions.

S^{14+} He-like			
Final state	**Excitation energy**	**Final state**	**Excitation energy**
$(1s_{1/2}2s_{1/2})_1$	2.4292	$(1s_{1/2}3p_{1/2})_0$	2.8789
$(1s_{1/2}2s_{1/2})_0$	2.4477	$(1s_{1/2}3p_{1/2})_1$	2.8790
$(1s_{1/2}2p_{1/2})_0$	2.4458	$(1s_{1/2}3p_{3/2})_2$	2.8795
$(1s_{1/2}2p_{1/2})_1$	2.4462	$(1s_{1/2}3p_{3/2})_1$	2.8829
$(1s_{1/2}2p_{3/2})_2$	2.4478	$(1s_{1/2}3d_{3/2})_1$	2.8819
$(1s_{1/2}2p_{3/2})_1$	2.4603	$(1s_{1/2}3d_{3/2})_2$	2.8819
$(1s_{1/2}3s_{1/2})_1$	2.8744	$(1s_{1/2}3d_{5/2})_3$	2.8821
$(1s_{1/2}3s_{1/2})_0$	2.8792	$(1s_{1/2}3d_{5/2})_2$	2.8823

Fig. 1 shows the electron impact excitation rate coefficients of S^{14+} ions in the energy range of 2.4-3.0 KeV. The solid blue line represents the result of the direct excitation, while the solid red line denotes the results with the resonance excitation included. The configurations $1s3l3l$ (l=*s, p, d*) and $1s3l4l'$ (l'=*s, p, d, f*) correspond to the resonance excitation processes.

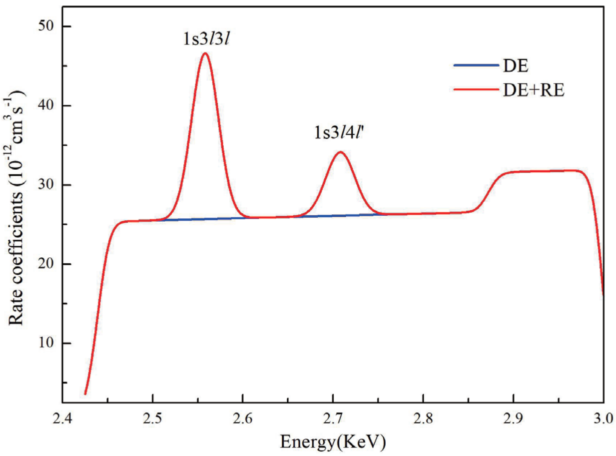

Fig. 1. A synthesized electron-impact excitation rate coefficients theoretical of S^{14+} ions with the DE and RE channels included.

Acknowledgment

This work has been supported by the National Key Research and Development Program of China (2017YFA0402300). Z. W. Wu acknowledges the support of the Scientic Research Program of the HigherEducation Institutions of Gansu Province, China (Grant No. 2018A-002).

References

[1] Chen-Zhong Dong, Jian-Guo Wang , and Yi-Zhi Qu, 1998 Chin. Phys. Soc. 7 4.

[2] Jun Jiang, Chen-Zhong Dong, Lu-You Xie, and Jian-Guo Wang, 2008 Phys. Rev. A **78** 022709.

---

[1] E-mail: zhongwen.wu@nwnu.edu.cn

[2] E-mail: phyjiang@yeah.net

[3] E-mail: dongcz@nwnu.edu.cn

Angular distribution and polarization of x-ray radiation in highly charged He-like ions: hyperfine-induced transition

Zhan-Bin Chen[1,2,3], **Chen-Zhong Dong**[2] [1]

[1] School of Science, Hunan University of Technology, Zhuzhou 412007, China
[2] Key laboratory of Atomic and Molecular Physics & Functional Materials of Gansu Province, College of Physics and Electronic Engineering, Northwest Normal University, Lanzhou, 730070, China
[3] College of Science, National University of Defense Technology, Changsha 410073, China

Precise polarization studies not only enhance people's understanding to the e-e interaction in strong Coulomb fields, but also help to deeper elucidate the population mechanism during the impact dynamics. While most theoretical studies regarding the polarization in the past had just dealt with ions with nuclear spin $I = 0$, fewer literatures had reported the effect of the hyperfine interaction and how the nuclear spin affected the polarization of x-ray radiation. Some kinds of ions have a nuclear spin $I \neq 0$. Owing to the hyperfine coupling, new decay channel will be open, namely, hyperfine-induced transition.

In this study, we present a systematically theoretical investigation on the polarization and angular distribution of x-ray photoemission during the hyperfine-induced transition using a fully RDW method [1]. The calculations are performed for the $1s2p_{3/2}\ {}^3P_2\ F_i{=}3/2 \rightarrow 1s^2\ {}^1S_0\ F_f{=}1/2$ component of the $K\alpha_1$ decay of highly charged He-like ${}^{119}\mathrm{Sn}^{48+}$ and ${}^{207}\mathrm{Tl}^{79+}$ ions with nuclear spin $I{=}1/2$ following the impact excitation processes by the incident electron beams of un-polarized and completely longitudinally-polarized, respectively. Two effects, Breit interaction(BI)and $E1$-$M2$ interference, on the polarization of the emitted radiation are discussed [2]. Our results show that both these effects may significantly affect the polarization and angular emission pattern of the transition line. For the circular polarization, the BI leads to a decrease by about 20% for ${}^{119}\mathrm{Sn}^{48+}$ ion and a decrease by about 50% for ${}^{207}\mathrm{Tl}^{79+}$ ion at 1.4X, respectively. The $E1$-$M2$ mixing results in a increase by about 41% for ${}^{119}\mathrm{Sn}^{48+}$ ion and in a reduction by about 97% for ${}^{207}\mathrm{Tl}^{79+}$ ion at 1.4X, respectively. For the linear polarization, the BI leads to a increase by 15% and 21% for ${}^{207}\mathrm{Tl}^{79+}$ ion at 1.2X and 1.6X, respectively. The $E1$-$M2$ mixing reduces the linear polarization by 36% and 21% for ${}^{119}\mathrm{Sn}^{48+}$ and ${}^{207}\mathrm{Tl}^{79+}$ ions at 1.2X, respectively. We hope that the present results would be useful in resolving some disagreement between the theories and experiments related to the polarization properties of the x-ray radiation.

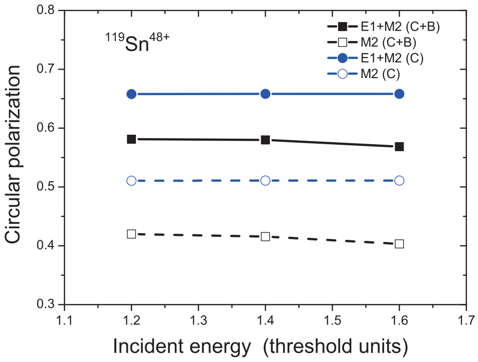

Fig. 1. The circular polarization of the $1s2p_{3/2}{}^3P_2F_i{=}3/2 \rightarrow 1s^2\ {}^1S_0F_f{=}1/2$ hyperfine-induced transition for He-like ${}^{119}\mathrm{Sn}^{48+}$ ion following longitudinally polarized EIE process as a function of the incident energy in threshold units. Here, C represents the values with inclusion of only the Coulomb interaction, and C+B represents the ones with the BI included; M2 represents inclusion of the magnetic-quadrupole approximation only, E1+M2 represents values with inclusion of *E1-M2* interference.

This work was supported by the National Natural Science Foundation of China (Grant Nos.11504421, U1332206, and 11274254) and International Scientific and Technological Cooperative Project of Gansu Province, China (Grant No.1104WCGA186).

References

[1] Z. B. Chen, C. Z. Dong, and J. Jiang, 2014 *Phys. Rev. A* **90** 022715.

[2] Z. B. Chen and C. Z. Dong, 2018 *Eur. Phys. J. D* (in press)

---

[1] E-mail: dongcz@nwnu.edu.cn

Dynamics and density distribution of laser-produced Al plasmas using optical interferometry

S. Q. Cao, M. G. Su[1], Q. Min, D. X. Sun, P. P. Ma, K. P. Wang, B. Wang, S. Q. He, L. Wu, H. D. Lu, and C. Z. Dong[2]

Key laboratory of Atomic and Molecular Physics & Functional Materials of Gansu Province, College of Physics and Electronic Engineering, Northwest Normal University, Lanzhou, 730070, China

The dynamics and state parameter diagnostics of laser-produced plasmas (LPP) are very important in developing its application such as pulsed-laser deposition, extreme ultraviolet and soft X-ray light sources, laser ion source and laser fusion. Some techniques have been employed for related research. Laser interferometry is widely established in studying the dynamic evolution and spatio-temporally resolved density profiles of LPP, particularly because of the highly accurate spatial and temporal resolutions.

In this work, dynamic evolution and spatio-temporally resolved density profiles of laser-produced Al plasmas in air atmosphere are investigated using optical interferometry. A series of interferograms are obtained with a pulse energy of 35 mJ and delay times from 200 *ns* to 6.9 *μ*s are showed in Fig. 1. From Fig. 1, the expansion profiles of the shock wave of Al plasmas are closed to semicircle all time, which is different from the situation of air plasmas in our previous work [1]. The phase shift and refractive index are calculated using a two-dimensional fast Fourier transformation and Abel transformation. The electron densities of Al plasmas are obtained from the refractive index have been showed in Fig. 2. ,which give the 2D expond dimensions and electron densities distribution of Al plasmas. This work provide a further understanding of expansion and dynamic evolution of the laser-produced Al plasmas and shock wave and the spatio-temporal evolution of the density of plasma in air atmosphere.

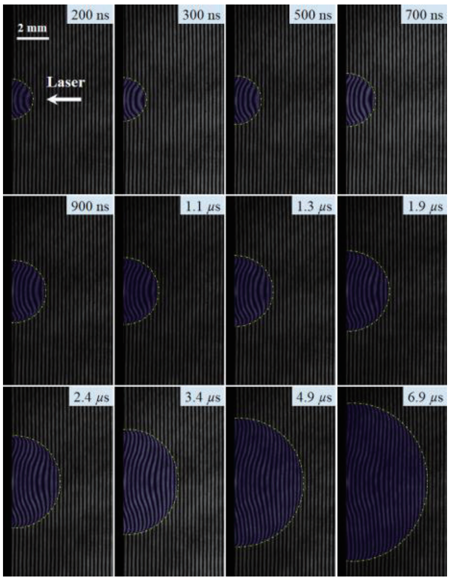

Fig. 1. Time evolution of optical interferograms of laser-produced Al plasmas (yellow dotted line and blue shaded area identify regions of shift in interference fringes).

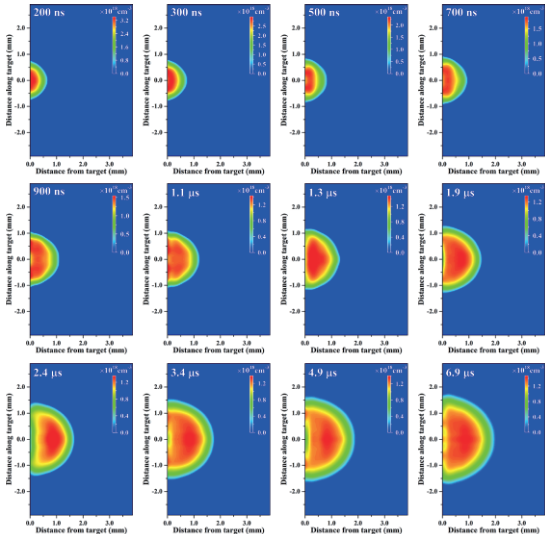

Fig. 2. 2D electron densities distribution of laser-produced Al plasmas at different delay times.

The work is supported by the National Key Research and Development Program of China (2017YFA0402300), the Natural Science Foundation of China (11364037,11274254, U1332206,11564037).

References

[1] S. Q. Cao, M. G. Su, C. Z. Dong et.al, 2018 *Phys. Plasmas* 25 063302

---

[1] E-mail: nwnu_sumg@163.com

[2] E-mail:dongcz@nwnu.edu.cn

Theoretical study of the dielectronic recombination process of Li-like W^{71+} ions

L. J. Dou[*, ξ, †] **, L. Y. Xie**[†,1]**, Z. K. Huang**[*]**, W. Q. Wen**[*]**, C. Z. Dong**[†]**, and X. W. Ma**[*, 2]

[*] Institute of Modern Physics, Chinese Academy of Sciences, Lanzhou, 730000, China
[ξ]University of Chinese Academy of Sciences, Beijing 100049, China
[†] College of Physics and Electronic Engineering, NWNU, Lanzhou, 730070, China

Dielectronic recombination (DR) and radiative recombination (RR) spectra of highly charged Tungsten ions are important for modeling and diagnosing magnetic fusion plasmas[1,2]. We studied the $\Delta n = 0$ DR process of Li-like $W^{71+}(2s)$ ions using the flexible atomic code (FAC) based on the relativistic configuration interaction (RCI) method[3]. The detailed resonance energies, widths and strengths were calculated systematically for the dominated doubly excited states $(2p_{1/2}nl_j)$ $(n=19\sim29)$ and $(2p_{3/2}n'l_j)$ $(n=7\sim29)$ of Be-like W^{70+} ions, and the contributions from the higher Rydberg states with $n \geq 30$, are obtained by extrapolation based on the quantum defect theory (QDT)[4].The electron-ion recombination spectra (DR+RR), covering the center-of-mass energy range 0-1700 eV, are presented by considering the temperature (120 meV/k_B transverse and 0.1 meV/k_B) for purpose of future storage ring experiments. The present results would be provide help for investigating the storage ring DR experiments and diagnosing of ITER plasmas.

Figures 1 and 2 plotted the total rate coefficients (DR+RR) (black line) for the lowest-energy resonance manifolds $(2p_{1/2}19l_j)_J$ of 2s-2p$_{1/2}$ transitions and $(2p_{3/2}7l_j)_J$ of $2s$-$2p_{3/2}$ transitions, respectively, where the red dashed line indicate the RR background. The blue vertical lines give the strengths for each of the individual resonance with the right blue axis, and the resonance positions are identified by the black vertical bars on the top of the figure.

This work is partly supported by the National Key R&D Program of China under grant No. 2017YFA0402300, the National Natural Science Foundation of China through Nos. 11320101003, 11611530684, U153014,11464042 and the Strategic Priority Research Program of the Chinese Academy of Sciences, grant No. XDB21030300 and the Key Research Program of Frontier Sciences, CAS, grant No.QYZDY-SSW-SLH006. And the Young Teachers Scientific Research Ability Promotion Plan of Northwest Normal University (No.NWNU-LKQN-15-3).

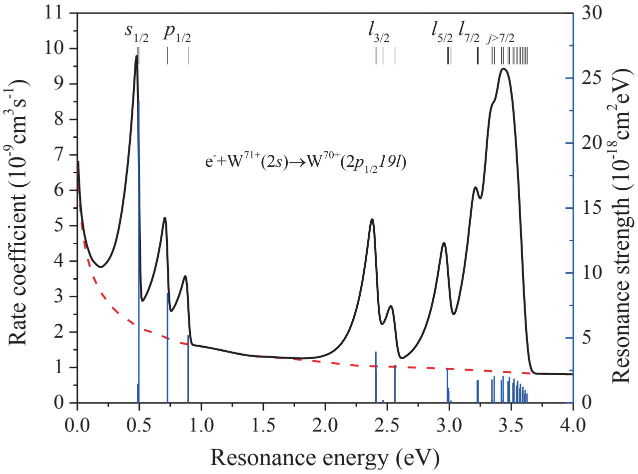

Fig. 1. The detailed rate coefficients for the lowest-energy DR resonance manifold $(2p_{1/2}19l_j)_J$ of W^{71+} ions.

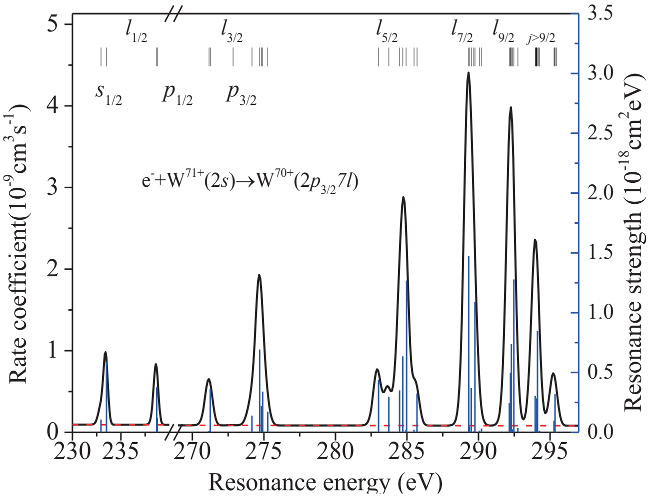

Fig. 2. Same as figure 1 but for the DR resonance manifold $(2p_{3/2}7l_j)_J$ of W^{71+} ions.

References

[1] Preval, 2016 *Phys. rev A* **93** 042703
[2] Trzhaskovskaya, 2014 *At. Data Nucl. Data Tables* **100** 986
[3] M. F. Gu, 2008 *Can. J. Phys* **86** 675
[4] Y. Hahn, 1985 *Adv. At. Mol. Phys* **21** 123

---

[1]E-mail: xiely@nwnu.edu
[2]E-mail: x.ma@impcas.ac.cn

Low energy range dielectronic recombination of Fluorine-like Fe^{17+} at the CSRm

Nadir Khan[1,2], Zhong-Kui Huang[1], Wei-Qiang Wen[1†], Li-Jun Dou[1,2], Shu-Xing Wang[3], Xin Xu[3], Han-Bing Wang[1], Sultan Mahmood[1], Chong-Yang Chen [4], Xiao-Ya Chuai[1,2], Xiao-Long Zhu[1], Dong-Mei Zhao[1], Li-Jun Mao[1], Jie Li [1], Da-yu Yin [1], Jian-Cheng Yang[1], You-Jin Yuan[1], Lin-Fan Zhu [3] and Xin-Wen Ma[1‡]

[1]Institute of Modern Physics, Chinese Academy of Sciences, Lanzhou 730000, China
[2]University of Chinese Academy of Sciences, Beijing 100049, China.
[3] Hefei National Laboratory for Physical Sciences at Micro scale, Department of Modern Physics, University of Science and Technology of China, Hefei 230026, China
[4]Institute of Modern Physics, Fudan University, 200433, Shanghai, China

Dielectronic recombination is one of the most important electron ion recombination process in astrophysical and men made plasma. The absolute dielectronic recombination rate coefficient of F-like Fe^{17+} ions has been measured at the main cooler storage ring (CSRm), at Institute of Modern Physics Lanzhou, China [1]. The measured electron-ion collision energy range 0-6 eV covered the first Rydberg series of $\Delta n = 0$ core excitations from $2s^22p^5(^2P_{3/2})\,nl$ to $2s^22p^5(^2P_{1/2})\,nl$ from n=18 up to n = 24.

The FAC code has been used to calculate DR rate coefficient and compared with experimental results [2]. Plasma rate coefficient were deduced from measured and calculated DR rate coefficient. Overall a reasonable agreement was found between the experimental results and theoretical results from FAC. Our results also compared with previously calculated MCBP, MCDF and measured experimental results of test storage ring (TSR) as shown in figure.1. [3,4]. We will present the DR rate coefficient as well as the obtained plasma rate coefficient of Fluorine-like Fe^{17+} ions at the conference.

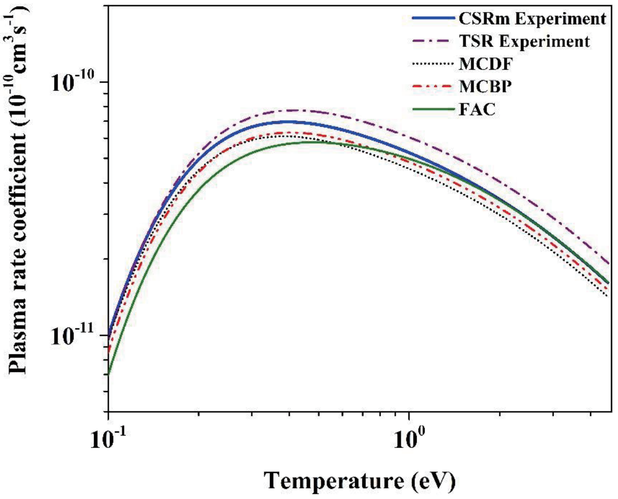

Fig. 1. Comparison of plasma rate coefficients derived from the experimental result with the calculated results from FAC code and also the existed plasma rates coefficients from literature. The thick solid blue line denote experimental results from CSRm and thin solid green line represents FAC calculation. The experimental result from TSR is displayed by Purple dash-dot line and corresponding calculations by MCBP and MCDF are shown by red dashed curve and black dotted curve, respectively.

References

[1] Z. K. Huang et al, 2018 *Astrophys. J. suppl. S.*, **235** 2.

[2] Nadir Khan et al, 2018 *Chinese Phys. C* **42** 064001.

[3] O. Zatsarinny et al, 2006 *Astron. Astrophys,* **447** 379.

[4] D. W. Savin et al, 1999 *Astrophys. J. suppl. S.*, **123** 687.

[†] Corresponding author. E-mail: wenweiqiang@impcas.ac.cn
[‡]Corresponding author. E-mail: x.ma@impcas.ac.cn

Dielectronic recombination of Be-like ions: astrophysical plasma applications and precision spectroscopy

W. Q. Wen *,[1], Z. K. Huang*, S. X. Wang†, X. Xu†, H. B. Wang*, L. J. Dou*, N. Khan*, X. L. Zhu*, D. M. Zhao*, L. J. Mao*, X. M. Ma*, J. Li*, M. T. Tang*, D. Y. Yin*, R. S. Mao*, Y. J. Yuan*, J. C. Yang*, L. F. Zhu† and X. Ma *,[2]

* Institute of Modern Physics, Chinese Academy of Sciences, 730000, Lanzhou, China
† Hefei National Laboratory for Physical Sciences at Microscale, Department of Modern Physics, University of Science and Technology of China, 230026, Hefei, China

Dielectronic recombination (DR) experiments of highly charged ions at the storage rings have been developed as a precision spectroscopic tool to investigate the topics from the atomic structure to nuclear properties. DR also plays a crucial role for accurate plasma modeling and spectral analysis in astrophysics and also man-made plasmas. The atomic levels and decay modes of Be-like ions is show in Fig. 1. DR of Be-like ions at heavy ion storage rings has been emphazised on different physical topics, such as first observation of trielectronic recombination (TR) for Be-like Cl^{13+}[1], first measurement of hyperfine induced transition rate of Be-like Ti^{18+} [2] and precision QED test [3]. In addition, DR of Be-like ions have been investigated for applications in astrophysical plasma [4].

Recently, electron-ion recombination of Be-like $^{40}Ar^{14+}$ and $^{40}Ca^{16+}$ have been measured by employing the electron-ion merged-beams method at the cooler storage ring CSRm [5, 6]. The DR resonances associated with $2s^2 \rightarrow 2s2p$ core transitions were identified by the Rydberg formula from the measured sprectra. In addition, strong TR resonances associated with $2s^2 \rightarrow 2p^2$ core transitions were observed. The plasma rate coefficients for DR+TR were deduced from the measured electron-ion recombination rate coefficients to compare with the previously recommended atomic data from the literature. The present results constitute a set of bench-mark data for use in astrophysical modeling.

In addition, we are preparing to perform DR experiments of highly charged Be-like ions at the CSRe, the investigation topics including hyperfine induced transition rate measurement with different nuclear spin, two-photon E1M1 ($2s2p\ ^3P_0 \rightarrow 2s^2\ ^1S_0$) decay rate measurement for nuclear spin I=0 and also measurement of the precision spectroscopy with ions heavier than Xe. These experiments will open a door for precision investigation of QED effects, electron-electron correlation and also relativity effects. We will present a poster on this workshop to show the detailed precision spectroscopy of DR experiments of Be-like ions at the heavy ion storage ring CSRe and HIAF [7].

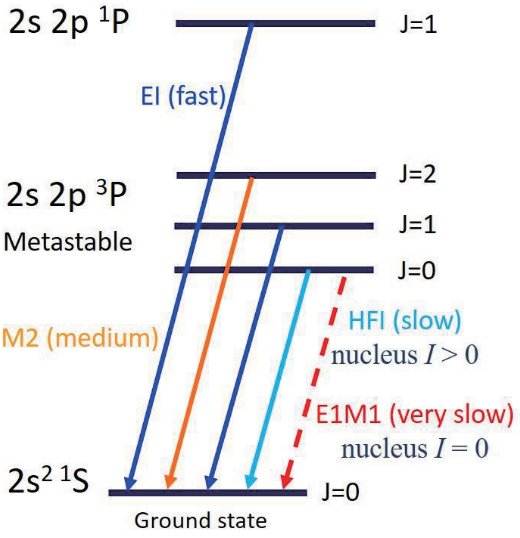

Fig. 1. Level scheme and decay modes of Be-like ion [2].

References

[1] M. Schnell et al. 2003 PRL **91**, 043001
[2] Schippers, et al. 2007 PRL **98,** 033001
[3] D. Bernhardt, et al. 2015 J. Phys. B **48**, 144008
[4] D. Savin, et al. 2006, APJ **642**, 1275
[5] Z.K. Huang, et al. 2018 APJS **235**, 2
[6] S.X. Wang, et al. 2018 APJ in press
[7] X. Ma, et al. 2017 Nucl. Instr. Meth. B **408,** 16

---

[1] E-mail: wenweiqiang@impcas.ac.cn

[2] E-mail: x.ma@impcas.ac.cn

The simulation of ultrcold neutral plasmas in initial spatial ordered distribution

Zhu Yu-hao*, Wu Yong*,[1], Zhou Fu-yang*, Yang Jie†

* Institute of Applied Physics and Computational Mathematics, Beijing, 100000, China
† Institute of Modern Physics, Chinese Academy of Sciences, Lanzhou, 730000, China

Ultrcold neutral plasmas (UNPs) is a strongly coupled plasma, in which the charged particles have very low temperature and the potential energy among the charged particles is larger than its kinetic energy. Disordered-inducing heating is a leading limitation of coupling strength. We employed the Debye one-component-plasma model[1] molecular dynamic to simulate the evolution of UNPs and investigate the influence of ordered initial distribution to disordered-inducing heating.

First of all, we compared the recent experiment[2] results with our simulation in order to verify the accuracy of our simulation model. The fig.1 shows the agreement is good. It is found in fig.1 that the agreement of process of disordered- inducing heating is excellent. However, the equilibrium temperature in simulation is lower than the condition of experiment. This is due to the expansion resulting from coulomb potential during the creation of UNPs. And we also simulated the evolution of coupling strength which is larger than 1 when it reaches equilibrium.

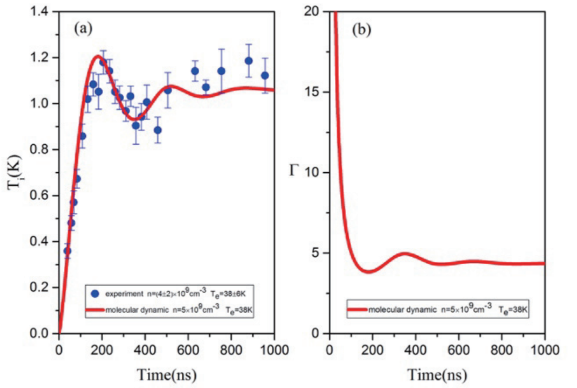

Fig.1. The evolution of ion temperature and ion coupling strength. (The blue dot is experiment result, the red line is simulation result.)

Under the periodic boundary, we studied the evolution of UNPs in the initial spatial ordered distribution. In the Fig.2, we found that the spatial ordered distribution of ions could dramatically decrease coupling strength, which agree with the latest simulation[3].

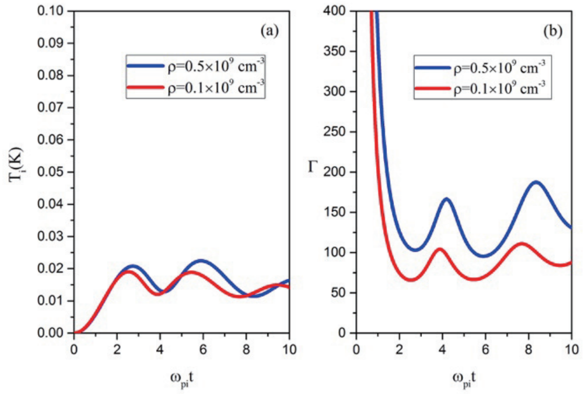

Fig.2. The evolution of ion temperature and ion coupling strength in ordered distribution with no expansion.

In addition, we consider the expansion in the creation of UNPs and Fig.3 shows expansion is able to induce the disordered-inducing heating, leading to the reduction of coupling strength.

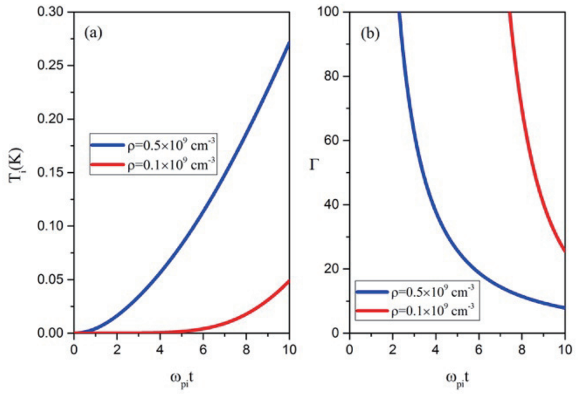

Fig.3. The evolution of ion temperature and ion coupling strength in ordered distribution with expansion.

References

[1] T.K. Langin, T.C. Killian et.al, 2016 *Phys. Rev. E.* 93 023201
[2] Y.C. Chen, T.C. Killian et.al, 2004 *Phys. Rev. Lett.* 92 143001
[3] D. Murphy and B.M. Sparkes et.al, 2016 *Phys. Rev. E.* 94 021201(R)

---

[1] E-mail: wu_yong@iapcm.ac.cn

Resonant multiple Auger decay of core-excited $2p^{-1}_{3/2}4s$ in argon

Yulong Ma*, Zhenqi Liu*, Fuyang Zhou† and Yizhi Qu*,[1]

* College of Material Sciences and Optoelectronic Technology, University of Chinese Academy of Sciences, Beijing 100049, China
† Data Center for High Energy Density Physics, Institute of Applied Physics and Computational Mathematics, Beijing 100088, China

Resonant Auger decay of a core-excited state produced by exciting an inner-shell electron to a Rydberg orbital, may emit one, two, and even more Auger electrons. Multiple Auger (MA) decay is one of the relax processes for an inner-shell excited atom upon radiationless decays, which results from many-electron Coulomb interaction. Therefore, investigations of such processes could give important information on electron correlation effects and many-body problems in atomic processes [1].

Generally, the emission of electrons in the MA decay can be simultaneous, or it can proceed in a stepwise manner through the creation and decay of an intermediate autoionizing state, which are referred to as the direct and cascade processes, respectively.

Based on multistep approaches, i.e., cascade, knockout and shakeoff mechanisms derived from many-body perturbation theory (MBPT) [2], we present a detailed theoretical study of the resonant single (SA), double (DA), triple (TA), and quadruple Auger (QA) for the Ar atom with a $2p_{3/2}$ hole following the resonant $2p_{3/2} \rightarrow 4s$ photoexcitation.

Resonant Auger decay can be clarified in terms of spectator, participator and shake processes, according to the behavior of the Rydberg electrons, however, a detailed theoretical investigations of which for MA decays is still missing at present. Therefore, the important one of aim in this work is to explore the contributions of spectator, participator and shake processes forming the final sates in SA, DA, TA and QA decays.

The direct TA Auger electron spectra are shown in Fig. 1, in where our theoretical results reproduce well the experimental measure [3]. The predicted branching ratios of different ions formed by the SA and MA decays including the contributions of the cascade and direct processes are given in Table 1, which show a good agreement with the experimental data [3, 4].

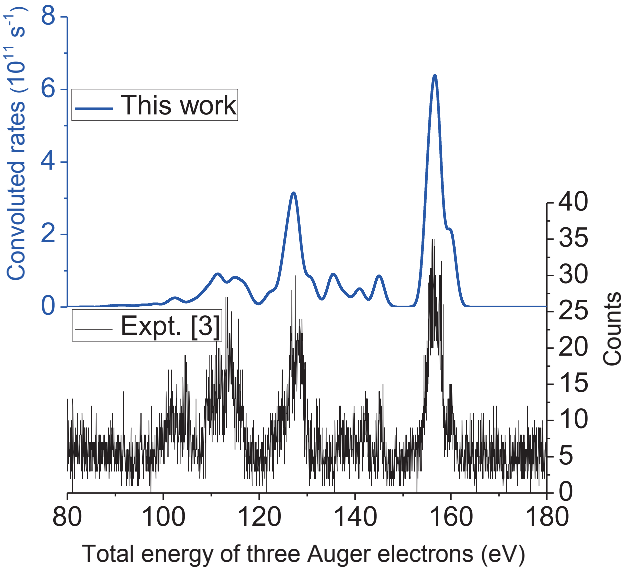

Fig. 1. Theoretical and experimental resonant direct triple Auger electron spectra of Ar $2p^{-1}_{3/2}4s$.

Table 1. Branching ratios (in percentages) of ions produced by single, double, triple and quadruple Auger decays of Ar $2p^{-1}_{3/2}4s$.

Ion	This work			Expt.	
	Cascade	Direct	Total	Ref. [3]	Ref. [4]
Ar^{+}	-	-	65.41	69	66
Ar^{2+}	21.52	9.83	31.35	28	30
Ar^{3+}	1.08	2.16	3.24	3	4
Ar^{4+}	0.01	0.08	0.09	0.03	0.2

References

[1] F. Penent, J. Palaudoux, P. Lablanquie, et al., 2005 *Phys. Rev. Lett.* 95 083002.
[2] M. Y. Amusia, I. S. Lee, and V. A. Kilin, 1992 *Phys. Rev. A* 45 4576.
[3] Y. Hikosaka, P. Lablanquie, F. Penent, et al., 2014 *Phys. Rev. A* 89 023410.
[4] J. A. R. Samson, W. C. Stolte, Z. X. He, et al., 1996 *Phys. Rev. A* 54 2099.

---

[1] E-mail: yzqu@ucas.edu.cn

Contribution of Strong Higher-order Resonant to X-ray Polarization of Dielectronic recombination of Si^{9+} Ions

S.M. Lu, L.Y. Xie[1], J. Jiang, D. H. Zhang, Z.W. Wu, C. Z. Dong

[1] Key laboratory of Atomic and Molecular Physics & Functional Materials of Gansu Province, College of Physics and Electronic Engineering, Northwest Normal University, Lanzhou, 730070, China

Recent investigations have shown that higher-order correlations with the active excitation of more than one electron may contribute considerably to recombination of highly charged ions and affect plasma parameters noticeably [1]. The strong contribution of higher-order processes have been found in highly charged silicon ions [2].Collisions of energetic electrons with highly charged ions, abundant in hot plasmas, may lead to emission of anisotropic and polarized characteristic x-rays. Study of polarization of x-ray lines can provide the information of orientation of the magnetic-field lines in both hot astrophysical and laboratory plasmas [3]. Polarization measurements can provide valuable and often unique insights into physical conditions of the plasma anisotropy [4].

In present work, we evaluate energy levels, radiative and auger rates, resonance energy and strength, x-ray polarization of dielectronic recombination of B-like Si^{9+} using the Flexible Atomic Code (FAC)[5] based on the relativistic configuration interaction approach.

Table 1. Comparison of the line polarization (P) of the x-rays from the ground state 2p $^2P_{1/2}$ and the metastable state 2p $^2P_{3/2}$ of Si^{9+} ions.

Process		Resonant state	P	
Ground	Metastable		Ground	Metastable
DR	DR	$[1s2s^22p_{1/2}2p^2]_3$	0.008	0.002
DR	DR	$[1s2s^22p_{1/2}2p^2]_2$	0.021	-0.012
DR	DR	$[1s2s^22p_{1/2}2p^2]_1$	0.016	-0.011
DR	DR	$[1s2s^22p_{1/2}2p^2]_1$	-0.001	0.004
TR	DR	$[1s2s^22p^3_{3/2}]_2$	-0.017	0.015
DR	DR	$[1s2s^22p_{1/2}2p^2]_0$	0.000	0.000
DR	DR	$[1s2s^22p_{1/2}2p^2]_1$	0.001	-0.007
DR	DR	$[1s2s^22p_{1/2}2p^2]_2$	-0.052	-0.052
TR	DR	$[1s2s^22p^3_{3/2}]_1$	0.036	-0.021

The stronger contributions of higher-order dielectronic recombination process, such as trielectronic (TR) and quadruelectronic (QR) recombination to the total cross sections are revealed, and the bigger difference of the x-ray line polarizations for the same resonant states that formed from the ground state 2p $^2P_{1/2}$ and the metastable state 2p $^2P_{3/2}$ channels respectively are found. The superposition polarization is obtained that provides useful reference for EBIT measurements in the future.

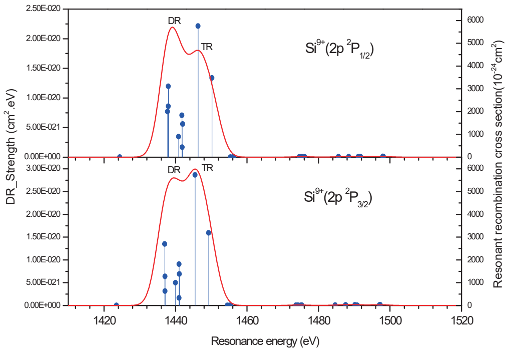

Fig. 1. Dielectronic recombination resonance strength (Blue vertical bar) and cross section (Red line) including DR and TR high-order processes from the ground state 2p $^2P_{1/2}$ (upper panel) and the metastable state 2p $^2P_{3/2}$ (lower panel) of Si^{9+} ions, respectively.

The work was supported by the National Key Research and Development Program of China (2017YFA0402300), the NSCF (Grant Nos:11564036, 11774292, U1530142, 11464042) and the Fund of NWNU (NWNU-LKQN-15-3).

References

[1]. C. Beilmann, Z. Harman, P. H. Mokler, 2013 *Phys. Rev. A* **88**, 062706.

[2].Thomas M. Baumann, Zoltán Harman, 2014 *Phy. Rev. A* **90**, 052704.

[3]. Chintan Shah, Holger Jörg, 2015 *Phy. Rev. A* **92**, 042702.

[4]. C HINTAN S HAH, DRAFT VERSION JANUARY **9**, 2018.

[5]. M. F. Gu, 2008 Can. *J. Phys.* **86**, 675.

---

[1] E-mail:xiely@nwnu.edu.cn

Measurement and analysis of EUV emission spectrum from laser produced Ni plasma

S. Q. He, M. G. Su[1], Q. Min, S. Q. Cao, L. Wu, H. D. Lu, D. X. Sun and C. Z. Dong

[*] Key laboratory of Atomic and Molecular Physics & Functional Materials of Gansu Province, College of Physics and Electronic Engineering, Northwest Normal University, Lanzhou, 730070, China

Highly charged ions of medium and high-Z elements exist widely in astrophysical, fusion plasmas and laboratory plasmas. Spectral structure analysis of highly-charged ions ablated by the high power density laser pulse can reveal abundant information on the plasmas, such as electron temperature, electron/ion density, particle and energy transport, and the evolution of these parameters. More recently, the observation and analysis of intense quasi-continuous emission features in the 7.5–14.5 nm spectral region of laser-produced plasmas of Pr have been reported.

In our work, we obtained the EUV spectrum of laser produced Ni plasma in the 7-14 nm wavelength range. Lines due to the resonant $3d$-$4f$ transition arrays of Ni^{6+} up to Ni^{10+} ions. We have calculated the resonance $3p^6(3d\text{-}4f)3d$ transitions of Ni^{8+} ions with the Hartree-Fock method by Cowan codes[1], and find that Gaussian profile is discontinuous and narrow. We added the $3p^5(3d\text{-}4f)3d^2$ transition so that its Gaussian profile is broad. The result is shown in Fig. 1.

Plasma parameters were estimated by comparing experimental and simulated spectra, based on the assumption of a normalized Boltzmann distribution among excited states and a steady-state collisional-radiative model[2]. The experimental spectrum, simulated spectra and ion fractions are shown in Fig. 2. The results provide further understanding of radiation properties of highly charged ions of middle- and high-Z elements.

The work is supported by the National Key Research and Development Program of China (2017YFA0402300), the Natural Science Foundation of China (11364037,11274254, U1332206,11564037).

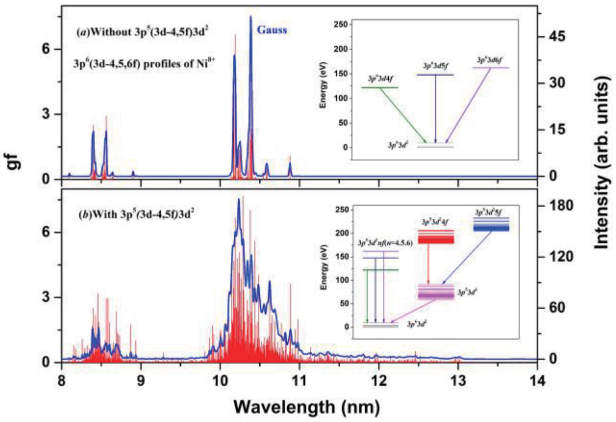

Fig. 1. 3d-4f transition arrays of Ni^{8+} and Energy level.

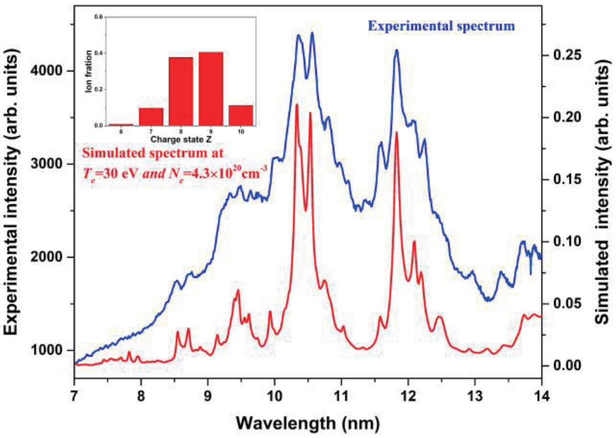

Fig. 2. Comparisons between the experimental spectrum and simulated spectra.

References

[1] Cowan R D 1991 *The Theory of Atomic Structure and Spectra*(Berkeley, CA: University of California Press).

[2] D. Colombant, G. F. Tonon, 1973 J. Appl. Phys 44 3524.

E-mail: nwnu_sumg @163.com

Two-electron one-photon transitions in He-like ions

M. X. Cao[*], **X. B. Ding**[*,1], **M. W. Zhang**[†], **D. Y. Yu**[†], **Y. L. Xue**[†], **C. Z. Dong**[*]

[*]Key laboratory of Atomic and Molecular Physics & Functional Materials of Gansu Province, College of Physics and Electronic Engineering, Northwest Normal University, Lanzhou, 730070, China

[†]Institute of Modern Physics, Chinese Academy of Sciences, Lanzhou 730000, China

The x-rays from the inner shell ionized few-electron systems provide valuable information on the temperature, density, and ionization state of the plasma and hence are useful in the theoretical modeling of plasmas. Precise transition properties can act as reference data for the charge state distribution and average charge of plasma. The doubly excited states of 2s2p configuration in He-like ions can decay to the $1s^2$ ground configuration through two electron one-photon (TEOP) transition. The TEOP transition is a good example for investigation on the electron correlation effects. The present calculations are carried out by using GRASP2K code which based on the multiconfiguration Dirac-Fock (MCDF) wave functions with the inclusion of Breit interaction, self-energy, and vacuum polarization.

The construction of the atomic state functions using systematic expansion of the orbitals in the active space. However, the TEOP transitions is sensitive to the correlation, the enhanced effects of correlation are systematically considered by expanding the active space from {1s, 2s, 2p} to the set that consisted of all orbitals with n = 1 to 6 and $l = 0$ to 3 so as to ensure the correlation, stability, and convergence of the observables. We first consider the necessary configurations and generated Dirac-Fock wavefunctions in extended optimal level (EOL) scheme for the initial doubly excited 2s2p and final $1s^2$ configurations. Then we consider single and double (SD) excitations of electrons and expand the active space by considering the first layer of the set with n = 3 and $l = 0$ to 2 virtual shells and optimized the orbital functions while 1s, 2s, and 2p orbitals were kept fixed. Continue the cycle until the system converges. The optimized orbitals thus generated were used in the evaluation of MCDF energies and rates.

The E1 transition energy (eV) and probabilities (s^{-1}) in the He-like Ar are given in Table 1. It can be seen from table that the results of calculated transition energy and rates becomes converged while the active space increase. The length and velocity gauges rates are in excellent agreement with each other for the various transitions to $^1S_0$ and $^3S_1$ states. The results show a good agreement between the present calculation and the previous work. Using the similar correlation model, the TEOP transition from 2s2p to $1s^2$ and OEOP transition from 2s2p to 1s2s were calculated for He-like Ne, Ar, Ca, Fe, Ni, Cu, Zn, Kr, Nb, and Ag ions. The electron correlation effects, Breit interaction on the transition energy and rate were analyzed. It will be helpful for the experimental investigation on the decay mechanism of inner shell doubly hole states.

Table1. Transition energies in eV, length gauge rates（B） and velocity gauge rates(C) in sec^{-1} of two-electron one-photon transitions from states of 2s2p configuration in He-like Ar. The numbers in the parentheses are powers of ten.

	$^3P_1$-.$^1S_0$			$^1P_1$-$^1S_0$		
Active set	Energy		Rate	Energy		Rate
DF	6395.485	C	8.493 (5)	6425.420	C	3.655(5)
		B	1.684 (8)		B	2.410(10)
{n3l2}	6395.395	C	2.953(8)	6425.142	C	4.747 (10)
		B	1.044(8)		B	1.781(10)
{n4l3}	6395.414	C	2.953(8)	6425.001	C	4.562(10)
		B	1.044 (8)		B	2.097 (10)
{n5l3}	6395.415	C	2.706 (8)	6424.645	C	4.445 (10)
		B	1.298(8)		B	2.239 (10)
{n6l3}	6395.374	C	2.785 (8)	6424.491	C	4.376(10)
		B	1.482 (8)		B	2.315 (10)
Ref	6396.059[1]		1.138(8)[1]	6424.385[1]		1.568(10)[1]
Theory				6399[2]		1.534(10)[2]
Expt.	6390[3]					

Acknowledgment

This work was supported by National Key Research and Development Program of China (2017YFA0402300).

References

[1] R. Kadrekar and L. Natarajan, Phys. Rev. A **84**, 062506(2011).

[2] T. K. Mukherjee, T. K. Ghosh, and P. K. Mukherjee, Z. Phys. D **33**, 7 (1995).

[3] H. Tawara and P. Richard, Can. J. Phys. **80**, 1579 (2002).

E-mail: *dingxb@nwnu.edu.cn*

Relativistic effects in 2p photoelectron spectra of sodium atoms from the initial state $2p^6 3p$

Xiaobin Liu^{*,1}, **Yinglong Shi**^{*2}

* Department of Physics, Tianshui Normal University, Tianshui, 741001, China

Photoionization is a fundamental atomic process in which an ion is formed as a result of the interaction of a photon with an atom. The need for accurate photoionization cross sections, as well as photoelectron spectra are shared by various research fields such as modeling of astrophysical objects and laboratory plasmas created using a high-energy laser pinch machine or tokamak. In addition, photoionization calculations together with detailed experimental measurements is a particularly sensitive tool for investigating atomic structure. On the other hand, quasi-one-electron systems are relatively simple systems which allow precise theoretical description within the framework of quantum theory. Then, as quasi-one-electron systems with a single electron outside the closed-shell core, alkali atoms are particularly suited for studies aiming for a comparison between theory and experiment.

Several investigations of the sub-valence 2p photoionization from the ground and excited states of sodium atoms have been performed both theoretically and experimentally in the past. By utilising the high resolution of electron spectrometers and the high brightness of third-generation synchrotron radiation sources, the fine structure of the photoelectron lines can be resolved. In this paper, we concentrate primarily on the photoelectron spectra of sodium atoms from the initial state $2p^6 3p$ and investigate the influence of relativistic effects using the multiconfiguration Dirac-Fock approximation (MCDF) method and the corresponding package Grasp92 [1]. For the relatively light sodium atom, the present MCDF results agree well or at least reasonable with experimental measurement [2, 3], and we clearly observe the manifestation of relativistic effects. One such effect is a spin-orbit splitting of the 2p photoionization process of sodium atoms. In the nonrelativistic limit, as generally expected, the present calculations indicate that the two relativistic channels can be reduced to the single photoionization process.

Our present work builds upon the experimental measurement of the 2p photoelectron fine-structure spectra from excited sodium atoms [2, 3]. Usually, the MCDF theory can provide clear and intuitive physical information from which the dynamics of the photoionization process can be interpreted. The present investigation demonstrates the information that may be obtained regarding the relativistic effects in subvalence photoionization processes, but the conclusions are by no means limited to excited sodium atoms.

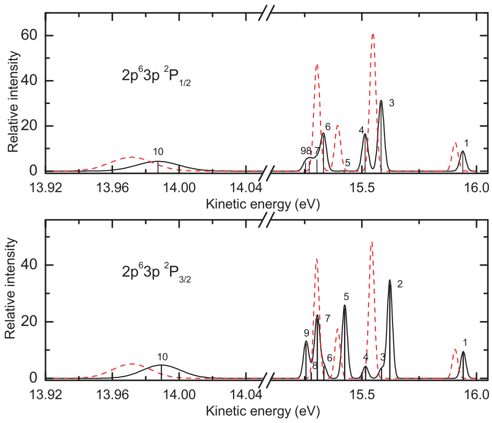

Fig. 1. The calculated $2p^5 3p$ photoelectron spectra of sodium atoms from the initial states $2p^6 3p$ at a photon energy of $h\nu$=54 eV; the assignments of photoelectron peaks are given in terms of the final ionic states. The results in the upper panel are the spectra for the initial state $2p^6 3p(^2P_{1/2})$, and those in the lower panel are for $2p^6 3p(^2P_{3/2})$. The solid lines are the relativistic calculated spectra, and the (red) dashed lines are the nonrelativistic spectra.

References

[1] K.G. Dyall, I.P. Grant, C.T. Johnson et. al., 1989 *Comput. Phys. Commun.* **55** 425

[2] A.N. Grum-Grzhimailo, E.V. Gryzlova, D. Cubaynes et. al., 2009 *J. Phys. B: At. Mol. Opt. Phys.* **42** 171002

[3] D. Cubaynes, S. Guilbaud, F.J. Wuilleumier et. al., 2009 *Phys. Rev.* A **80** 023410

---

[1] E-mail: liuxb@tsnu.edu.cn

[2] E-mail: shiyl@tsnc.edu.cn

Electron Impact Excitation of the 4 $^1S_0$-4 $^1P_1$ State of Zinc Atom

X. S. Cheng, L. Y. Xie[1], J. Jiang, D. H. Zhang, Z. W. Wu, and C. Z. Dong

Key laboratory of Atomic and Molecular Physics & Functional Materials of Gansu Province, College of Physics and Electronic Engineering, Northwest Normal University, Lanzhou, 730070, China

Electron impact experiments have played a crucial role in the study of atomic and molecular structure and in providing the cross sections needed for modelling of different types of plasma.There has been a growing interest in studies of electron impact excitation of Zn atoms due to possible application in discharge lamps and a need for modeling of Zn plasma systems. By studying of the Stokes parameters, one can explore detail information of shape and orientation of the charge cloud for the excited atoms. Many attentions have been focused on the electron impact excitation of zinc atoms both experimentally and theoretically [1-3].

In this work, we used relativistic distorted-wave methods to study the electron impact excitation of the zinc 4^1P_1 state from the ground 4^1S_0 state. In the calculations, to well incorporating complex electron correlations and exploring its effects on total and differential cross sections, and Stokes parameters, three correlation models are considered. In Mod1, the single-configuration calculation has been performed to obtain the relativistic wave functions for the ground state 4^1S_0 and the excited state 4^1P_1 using GRASP2K code based on Multi-configuration Dirac–Fock (MCDF) method [5]. In Mod2, the relativistic wave functions have been obtained with considering the valence-valence correlation configurations ($4s^2$, 4s5s, 4p5p, $4p^2$, $5s^2$, $5p^2$) $_{J=0}$ and (4s4p, 4s5p, 4p5s, 5s5p) $_{J=1}$ for the 4^1S_0 and 4^1P_1 states respectively. In Mod3, the core-valence correlations are included based on Mod2, adding $3d^94s^24p$, $4s^25p$, $4s4p^2$, 4s4p5s, 4s4p5p, 4s5s5p, $4s5p^2$, $4p^25s$, 4p5s5p, $4p5s^2$, $5s^25p$, $5s5p^2$, $3d^84s^24p5s$ excited configurations. In Fig.1 (a) and (b) the differential cross section and Stokes parameters (P_1, P_2 and P_3) are shown for zinc atom with considering incident electron energy 60eV as an example, respectively. It is found that there are very important influence of electronic correlation effects on the differential cross section, and Stokes parameters.

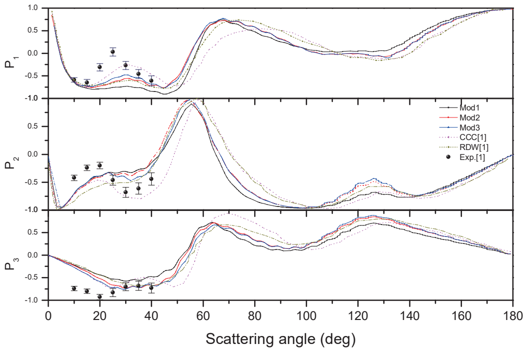

Fig.1. Stokes parameters (P_1, P_2 and P_3) for Zn 4^1P_1 state excitation from the ground state with incident electron energy 40eV.

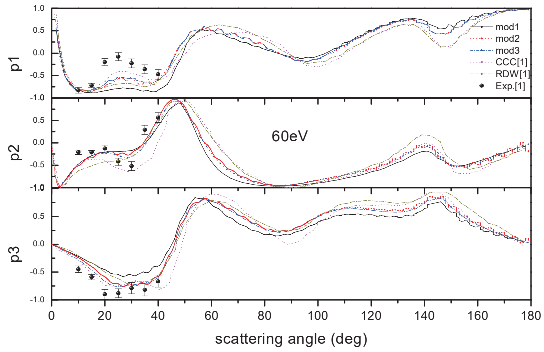

Fig.2. Stokes parameters (P_1, P_2 and P_3) for Zn 4^1P_1 state excitation from the ground state with incident electron energy 60eV.

The work was supported by the National Key Research and Development Program of China (No. 2017YFA0402300), the Natural Science Foundation of China (Nos.U1530142, 11564036, 11774292, 11464042) and the Foundation of NWNU (NWNU-LKQN-15-3)

References

[1] Piwiński, Mariusz, et al. 2018 ***J. Phys. B*** **51** 085002.
[2] Das T, Srivastava R,2014 ***Phys. Lett. A*** **378** 641.
[3] Fursa D V, Bray I, Panajotović R, 2005 **Phys. Rev. A** **72**, 012706.
[4] Kaur S, Srivastava R, 1997 **J. Phys. B** **30**, 1027
[5]Jönsson P, He X, Fischer C. F, and Grant I P, 2007 **Comput. Phys. Commun**. **177** **7**

---

[1] E-mail: *xiely@nwnu.edu.cn*

Investigation of the expansion dynamics of silicon plasmas generated by double nanosecond laser pulses

Qi Min, Maogen Su*[1], Duixiong Sun, Shiquan Cao, Chenzhong Dong*[2]

* Key laboratory of Atomic and Molecular Physics & Functional Materials of Gansu Province, College of Physics and Electronic Engineering, Northwest Normal University, Lanzhou, 730070, China

Up to now, there have been numerous experimental and theoretical studies on the plasma generated by a single pulse (SP). However, the interaction of two plasmas generated by the double pulse (DP) configuration and the physical mechanisms involved in this process constitute a research area that has not been sufficiently explored, though the first experiments were performed in the early 1970s [1].

A systematic investigation of the expansion dynamics of plasma plumes generated by two Q-switched Nd:YAG lasers at 1064 nm wavelength operating on a silicon target was undertaken for the inter-pulse delay times of 0, 100, 200, and 400 ns using a technique involving fast-gated intensified charge-coupled device imaging [2].

The ICCD images of the expanding plume at different acquisition delay times are given in Figs. 1(a)–1(f) for the different pulse schemes. Here, the real dimensions of each image in the series are 36.67 × 36.67 mm. The pulse energy of each beam for the DP scheme is fixed as 300 mJ. The inter-pulse delay time (Δt) is defined as the time difference between the arrival of the two laser pulses. The acquisition delay time (t_a) is the time difference between the arrival of second laser pulse and the time that the ICCD begins to acquire data. Our results indicate that the plasmas exhibit free expansion in a vacuum environment at an inter-pulse delay time of 0 ns. With increasing inter-pulse delay time, the plasma front becomes sharpened and an interaction boundary is formed.

We can offer a brief explanation on the formation and evolution mechanism of DP plasma for the inter-pulse delay time is more than 50 ns: (1) When Laser I first interacts with the target surface, the generated plasma experiences free expansion in vacuum. (2) When Laser II pulse arrives at a later time, the second plasma generated thereby expands in a rarefied high-temperature plasma environment. The ambient plasma has no influence on the second plasma propagation during the initial acquisition delay time because the pressure of the second plasma is much higher than that of the ambient plasma pressure. (3) The second plasma expands rapidly until its driving pressure has decreased considerably, then an interaction boundary is formed between the second plasma and ambient plasma.

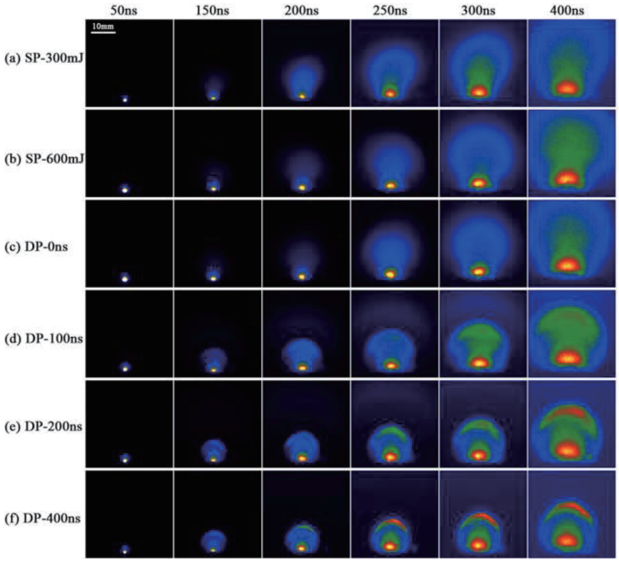

Fig. 1. Spatio-temporal Si emission images of plasma expansion for a single pulse with a pulse energy of (a) 300 and (b) 600 mJ, and for a double pulse with a laser delay between pulses (Δt) of (c) 0, (d) 100, (e) 200 and (f) 400 ns. The ICCD acquisition delay time (t_a) is noted at the top of each image column.

This work was supported by National Key Research and Development Program of China (2017YFA0402300); National Natural Science Foundation of China (NSFC) (11274254, U1332206, 11364037, 11064012, 11564037).

References

[1] P. T. Rumsby, J. W. M. Paul and M. M. Masoud, 1974 *Phys. Control. Fusion* 16 969.
[2] Q. Min, M. G. Su, B. Wang, et al., 2018 *Physics of Plasmas*, accepted.

---

[1] E-mail: **nwnu_sumg@163.com**

[2] E-mail: **dongcz@nwnu.edu.cn**

Investigation of EUV spectra from laser-produced Cr plasmas

Lei Wu, Maogen Su*^,1^, Qi Min, Shiquan Cao, Duixiong Sun, Chenzhong Dong*^,2^

* Key laboratory of Atomic and Molecular Physics & Functional Materials of Gansu Province, College of Physics and Electronic Engineering, Northwest Normal University, Lanzhou, 730070, China

Spectral data of laser-produced plasmas (LPPs) of middle- and high-Z elements are of great importance for diagnostic studies about fusion plasmas, astrophysical and laboratory plasmas, as well as for interpretation of spectral structures, conversion efficiencies, and radiative transport in plasmas [1,2].

In this work, EUV spectra of laser-produced Cr plasma in the 6.5-15 nm wavelength range were studied experimentally and theoretically, where the 3p-4d, 5d, and 3s-4p transitions dominate the observed emission. The experiment was performed using a Q-switched Nd:YAG laser with 10 ns FWHM pulse durations at a wavelength of 1064 nm. The peak power density was 2.0×10^{11} W/cm^2.

Theoretical values for wavelengths and weighted radiation probabilities for 3p-4d, 5d, and 3s-4p transitions were calculated using the Hartree-Fock method by Cowan codes and the flexible atomic code (FAC), respectively. Fig.1 shows the comparison between the experimental and simulated spectra. A simulated with T_e=38.4 eV and $N_e = 5 \times 10^{21}$ cm^{-3} is plotted to illustrate spectral features, the dominant fractional contributions arising from Cr^{5+}-Cr^{10+} are 5%, 15%, 30%, 30%, 16% and 4%.

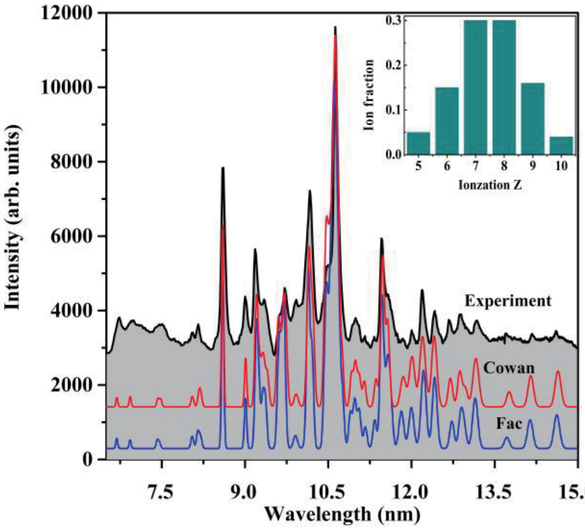

Fig. 1. Comparisons between the experimental and simulated spectra.

Reference

[1] M. J. May, K. B. Fournier, et.al, 2003 *Phys. Rev. E* 68 036402.

[2] H. P_epin, B. Grek, F. Rheault, and D. J. Nagel, 1977 *J. Appl. Phys* 48 3312

---

[1] E-mail: **nwnu_sumg@163.com**

[2] E-mail: **dongcz@nwnu.edu.cn**

Dielectric recombination of highly charged tungsten ions

M. J. Li*, Y. B. Fu*, X. B. Ding*, C. Z. Dong*, [1], F. Koike†

* Key laboratory of Atomic and Molecular Physics & Functional Materials of Gansu Province, College of Physics and Electronic Engineering, Northwest Normal University, Lanzhou, 730070, China
† National Institute for Fusion Science, Toki, Gifu 509-5292, Japan

Tungsten will be used as a plasma-facing material within the divertor region of the International Thermonuclear Experimental Reactor (ITER), and the modeling of tungsten impurity transport and radiative power loss is vital in ITER. Accurate date of dielectronic recombineation (DR) on the ionization balance of tungsten ions is very significant for divertor plasma modeling and radiative cooling studies. We calculated the DR rate coefficients of Ge-, As-, Br-, Kr- and Rb-like tungsten ions using the Flexible Atomic Code (FAC) [1].

Figure 1 shows DR rate coefficients for 4*l* shell excitation are dominant at low temperature and DR rate coefficients for 4*s* subshell excitation are larger than 4*p* subshell excitation for Ge-like tungsten ions. However, with the increase of charge state, the contribution from 4*p* subshell excitation gradually increases and becomes dominant in the whole temperature range. For Rb-like tungsten, 4*p* subshell excitation dominates in the same region. It is larger than 4*d* subshell excitation by near one order of magnitude.

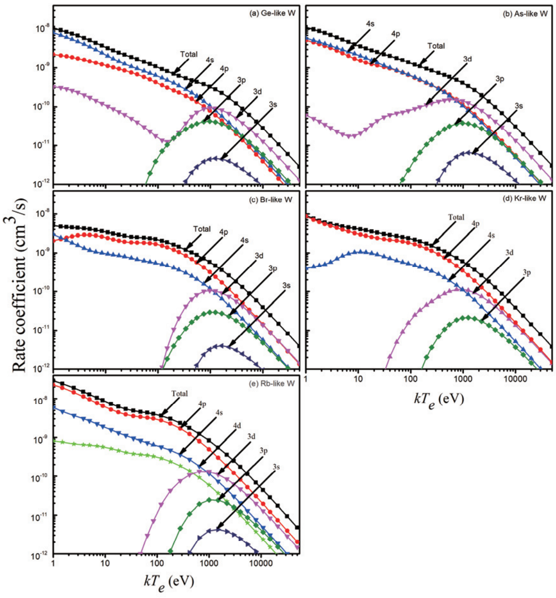

Figure. 1.The calculated DR rate coefficients of inner-shell electron excitation from Ge-, As-, Br-, Kr- and Rb-like tungsten ions as functions of plasma electron temperature. Each curve illustrates the patial DR rate for excitations from specific inner-shell orbitals as indicated in the figure.

For 3*l* shell excitation, the contribution from 3*d* subshell excitation plays an addition nally important role in the total DR rate Rb-like tungsten, 4*p* subshell excitation dominates in the same region. It is larger than 4*d* subshell excitation by near one order of magnitude. For 3*l* shell excitation, the contribution coefficients of Ge-, As-, Br-, Kr- and Rb-like tungsten ions at intermediate and high temperature.

In order to reproduce the present results conveniently, the total DR rate coefficients of Ge-, As-, Br-, Kr- and Rb-like tungsten ions were fitted to the following empirical formula (in units of cm^3/s) [2]:
where both c_i and E_i are fitting parameters. Using the parameters are listed in Table 1.The

$$\alpha_{DR}(\kappa Te) = (\kappa Te)^{-3/2} \sum_{i=1}^{6} c_i \exp(-\frac{E_i}{\kappa Te})$$

present calculated total DR rate coefficients of Ge-, As-, Br-, Kr- and Rb-like tungsten ions can be reproduced within 1.6% for $\kappa Te > 5$ eV.

Table1 Fit parameters for the total DR rate coefficient formula in equation. Notation A[B] denotes A×10^B.

Fit	Ge-like	As-like	Br-like	Kr-like	Rb-like
c_1	1.6944[-6]	1.6014[-7]	6.0746[-7]	1.9070[-7]	3.9007[-7]
E_1	1.1615[2]	5.0613[0]	3.3713[1]	6.5731[0]	5.1508[0]
c_2	4.4742[-6]	4.8517[-6]	1.7700[-7]	7.7977[-7]	1.2141[-6]
E_2	3.4936[2]	3.3090[2]	6.9936[0]	3.2360[1]	3.5521[1]
c_3	6.2817[-7]	1.6915[-6]	5.7629[-6]	2.9429[-6]	5.0545[-6]
E_3	4.0746[1]	1.0235[2]	2.2787[2]	1.0602[2]	1.0896[2]
c_4	1.7999[-5]	1.2484[-5]	2.9373[-6]	6.7028[-6]	1.0545[-5]
E_4	2.1950[3]	9.1731[2]	9.8938[1]	2.5447[2]	2.4496[2]
c_5	1.7095[-7]	1.4246[-5]	2.2508[-5]	1.2033[-5]	1.5455[-5]
E_5	5.6003[0]	1.9728[3]	1.7514[3]	6.7877[2]	6.4479[2]
c_6	1.4323[-5]	5.2788[-7]	1.1814[-5]	1.9456[-5]	2.1248[5]
E_6	1.0829[3]	3.1933[1]	6.5898[2]	1.7055[3]	1.6974[3]

References

[1] M. F. Gu, 2003 *Astrophys. J.* **590** 113 [1]
[2] Meng F C,Chen C Y,Shi X H,et al.2007,*J.Phys.B: At. Mol.Opt.Phys.*,40:4269

---

[1] 1.E-mail: dongcz@nwnu.edu.cn

Participant List

	Name	Title	Affiliation	Email
1	Tachibana Yuichi	Master Student	IMRAM, Tohoku University	yuichi@mail.tagen.tohoku.ac.jp
2	Takahashi Masahiko	Prof.	IMRAM, Tohoku University	masahiko@tohoku.ac.jp
3	Esaka Takehiko	Master Student	Kyoto University	esaka.takehiko.86a@st.kyoto-u.ac.jp
4	Fujii Keisuke	Assis. Prof.	Kyoto University	fujii@me.kyoto-u.ac.jp
5	Osugi Takuya	Master Student	Kyoto University	t.4.103.tkynt@gmail.com
6	Kato Daiji	Assoc. Prof.	National Institute for Fusion Science	kato.daiji@nifs.ac.jp
7	Morita Shigeru	Prof.	National Institute for Fusion Science	morita@nifs.ac.jp
8	Koike Fumihiro	Prof.	Sophia University	koikef@sophia.ac.jp
9	Tanuma Hajime	Prof.	Tokyo Metropolitan University	tanuma-hajime@tmu.ac.jp
10	Nakamura Nobuyuki	Assoc. Prof.	University of The Electro-Communications	n_nakamu@ils.uec.ac.jp
11	Kwon Duck Hee	Prof.	Korea Atomic Energy Research Institute	hkwon@kaeri.re.kr
12	Pan Congyuan	Assoc. Prof.	Anhui Universtiy	cypan@ahu.edu.cn
13	Yuan Jianmin	Prof.	China Academy of Engineering Physics	jmyuan@nudt.edu.cn
14	Ding Hongbin	Prof.	Dalian University of technology	hding@dlut.edu.cn
15	Zhao Yuxiang	Assoc. Prof.	Department of Physics, Tianshui Normal University	158381077@qq.com
16	Li Shuang	Dr.	Fujian Agriculture and Forestry University	lishuangwuli@126.com
17	Yang Yang	Assoc. Prof.	Fundan University	yangyang@fudan.edu.cn
18	Lu Qifeng	Master Student	Fudan University	16210200006@fudan.edu.cn
19	Ma Kun	Assoc. Prof.	Huangshan University	makun0602@163.com
20	Chen Zhan-Bin	Dr.	Hunan University of Technology	253072513@qq.com
21	He Bin	Prof.	Institute of Applied Physics and Computational Mathematics	hebin-rc@163.com
22	Wu Yong	Prof.	Institute of Applied Physics and Computational Mathematics	wu_yong@iapcm.ac.cn
23	Yuan Xiang	Master Student	Institute of Applied Physics and Computational Mathematics	yuanxiangjlu@163.com
24	Zhu Yuhao	Phd Student	Institute of Applied Physics and Computational Mathematics	zhu_yuhao@foxmail.com

25	Shao Caojie	Prof.	Institute of Modern Physics	c.shao@impcas.ac.cn
26	Dou Lijun	Phd Student	Institute of Modern Physics, CAS	doulijun@impcas.ac.cn
27	Khan Nadir	Phd Student	Institute of Modern Physics, CAS	nadirkhan@impcas.ac.cn
28	Song Zhangyong	Dr.	Institute of Modern Physics, CAS	songzhy@impcas.ac.cn
29	Wang Wei	Dr.	Institute of Modern Physics, CAS	wangwei@impcas.ac.cn
30	Wen Weiqiang	Dr.	Institute of Modern Physics, CAS	wenweiqiang@impcas.ac.cn
31	Yang Bian	Dr.	Institute of Modern Physics, CAS	yangbian@impcas.ac.cn
32	Zhang Mingwu	Dr.	Institute of Modern Physics, CAS	zhangmingwu@impcas.ac.cn
33	Yu Yanmei	Dr.	Institute of Physics, CAS	ymyu@aphy.iphy.ac.cn
34	Yang YuJun	Assoc. Prof.	Jilin University	yangyj@jlu.edu.cn
35	Yuan Haiying	Master Student	Jilin University	1871952041@qq.com
36	Li Bowen	Assoc. Prof.	Lanzhou University	libw@lzu.edu.cn
37	Hu Zhimin	Prof.	Laser Fusion Research Center, China Academy of Engineering Physics	zhimin.hu@caep.cn
38	Xiong Gang	Dr.	Laser Fusion Research Center, China Academy of Engineering Physics	gxiong16@fudan.edu.cn
39	Gao Cheng	Assis. Prof.	National University of Defense Technology	gaocheng@nudt.edu.cn
40	Liu Pengfei	Phd Student	National University of Defense Technology	feipeng1050@163.com
41	Zeng Jialong	Prof.	National University of Defense Technology	jlzeng@nudt.edu.cn
42	Bakhiet Mohammed	Phd Student	Northwest Normal University	mohanaz777@gmail.com
43	Cao Shi-Quan	Phd Student	Northwest Normal University	cao_sq@163.com
44	He Si-Qi	Master Student	Northwest Normal University	hsq908@126.com
45	Lu Hai-Dong	Master Student	Northwest Normal University	luhd_1@163.com
46	Min Qi	Phd Student	Northwest Normal University	mq_lpps@163.com
47	Tang Zhi-Ming	Master Student	Northwest Normal University	tangzhimingphys@126.com
48	Wu Lei	Master Student	Northwest Normal University	568128709@qq.com
49	Cao Ming-Xin	Master Student	Nothwest Normal University	763481251@qq.com

50	Cheng Xiao-Shu	Master Student	Nothwest Normal University	2561129023@qq.com
51	Ding Xiaobin	Assoc. Prof.	Nothwest Normal University	dingxb@nwnu.edu.cn
52	Dong Chenzhong	Prof.	Nothwest Normal University	dongcz@nwnu.edu.cn
53	Jiang Jun	Assoc. Prof.	Nothwest Normal University	jiangjun@nwnu.edu.cn
54	Li Maijuan	Phd Student	Nothwest Normal University	620773990@qq.com
55	Lu Si-Mei	Master Student	Nothwest Normal University	1120804082@qq.com
56	Ma Peng-Peng	Master Student	Nothwest Normal University	ma_pp08@126.com
57	Ren Cheng	Master Student	Nothwest Normal University	18893700913@163.com
58	Su Maogen	Prof.	Nothwest Normal University	sumg@nwnu.edu.cn
59	Sun Duixiong	Assoc. Prof.	Nothwest Normal University	sundx@nwnu.edu.cn
60	Wang Kai-Ping	Master Student	Nothwest Normal University	wang-kp1993@163.com
61	Xie Luyou	Assoc. Prof.	Nothwest Normal University	xiely@nwnu.edu.cn
62	Zhang Feng-Ling	Master Student	Nothwest Normal University	1072023560@qq.com
63	Zhang Denghong	Assoc. Prof.	Nothwest Normal University	zhangdh@nwnu.edu.cn
64	Yu Jin	Prof.	Shanghai Jiao Tong University	jin.yu@sjtu.edu.cn
65	Xiaobin Liu	Assoc. Prof.	Tianshui Normal University	liuxb@tsnu.edu.cn
66	Yinglong Shi	Assoc. Prof.	Tianshui Normal University	shiyl@tsnu.edu.cn
67	Ma Yulong	Phd Student	University of Chinese Academy of Sciences	mylphy@Hotmail.com
68	Qu Yizhi	Prof.	University of Chinese Academy of Sciences	yzqu@ucas.edu.cn
69	Chen Lei	Phd Student	University of Science and Technology of China	leichen@mail.ustc.edu.cn
70	Chen Xiangjun	Prof.	University of Science and Technology of China	xjun@ustc.edu.cn
71	Liu Zhaohui	Phd Student	University of Science and Technology of China	chinalzh@mail.ustc.edu.cn
72	Liu Yawei	Assoc. Prof.	University of Science and Technology of China	liuyawei@ustc.edu.cn
73	Shan Xu	Assoc. Prof.	University of Science and Technology of China	xshan@ustc.edu.cn
74	Tian Shanxi	Prof.	University of Science and Technology of China	sxtian@ustc.edu.cn
75	Wang Shuxing	Phd Student	University of Science and Technology of China	wsx0417@mail.ustc.edu.cn

76	Wang Qiuping	Prof.	University of Science and Technology of China	qiuping@ustc.edu.cn
77	Zhao Xi	Phd Student	University of Science and Technology of China	zx0214@mail.ustc.edu.cn
78	Zhu Lin-Fan	Prof.	University of Science and Technology of China	lfzhu@ustc.edu.cn
79	Zhao Yongtao	Prof.	Xian Jiaotong University	zhaoyongtao@xjtu.edu.cn
80	Li Yao Zong	Prof.	Xianyang Normal University	1095036037@qq.com
81	Liang Chang Hui	Prof.	Xianyang Normal University	1758858011@qq.com
82	Wang Yi Jun	Prof.	Xianyang Normal University	806605363@qq.com
83	Wang Baonian	Prof.	Institute of Plasma Physics, CAS	bnwang@ipp.ac.cn
84	Dong Shaohua	Head of Foreign Affairs Office	Institute of Plasma Physics, CAS	shdong@ipp.ac.cn
85	Hu Liqun	Prof.	Institute of Plasma Physics, CAS	lqhu@ipp.ac.cn
86	Wu Zhenwei	Prof.	Institute of Plasma Physics, CAS	zwwu@ipp.ac.cn
87	Wang Liang	Prof.	Institute of Plasma Physics, CAS	lwang@ipp.ac.cn
88	Lyu Bo	Prof.	Institute of Plasma Physics, CAS	blu@ipp.ac.cn
89	Huang Juan	Prof.	Institute of Plasma Physics, CAS	juan.huang@ipp.ac.cn
90	Xiao Bingjia	Prof.	Institute of Plasma Physics, CAS	bjxiao@ipp.ac.cn
91	Liu Haiqing	Assoc. Prof.	Institute of Plasma Physics, CAS	hqliu@ipp.ac.cn
92	Liu Xiaoju	Assoc. Prof.	Institute of Plasma Physics, CAS	julie1982@ipp.ac.cn
93	Gao Wei	Assoc. Prof.	Institute of Plasma Physics, CAS	gw118@ipp.ac.cn
94	Zhang Ling	Assoc. Prof.	Institute of Plasma Physics, CAS	zhangling@ipp.ac.cn
95	Zhang Hongmin	Assis. Prof.	Institute of Plasma Physics, CAS	hmzhang@ipp.ac.cn
96	Chen Yingjie	Dr.	Institute of Plasma Physics, CAS	bestfay@gmail.com
97	Xu Zong	Dr.	Institute of Plasma Physics, CAS	xuzhong@ipp.ac.cn
98	Yang Xiuda	Phd Student	Institute of Plasma Physics, CAS	xdyang@ipp.ac.cn
99	Cheng Yunxin	Master Student	Institute of Plasma Physics, CAS	yunxin.cheng@ipp.ac.cn
100	Li Lei	Master Student	Institute of Plasma Physics, CAS	lei.li2@ipp.ac.cn